UNIVERSIDADE FEDERAL DE SÃO CARLOS

CENTRO DE CIÊNCIAS EXATAS E DE TECNOLOGIA

PROGRAMA DE PÓS-GRADUAÇÃO EM ENGENHARIA QUÍMICA

NUHU AYUBA

Application of CFD to Study the Dynamics of Droplets Expelled During Coughing

Aplicação de CFD no Estudo da Dinâmica de Gotículas Expelidas Durante a Tosse

SÃO CARLOS - SP

AUGUST, 2024

UNIVERSIDADE FEDERAL DE SÃO CARLOS

CENTRO DE CIÊNCIAS EXATAS E DE TECNOLOGIA

PROGRAMA DE PÓS-GRADUAÇÃO EM ENGENHARIA QUÍMICA

NUHU AYUBA

Doctoral Thesis presented to the Postgraduate Program in Chemical Engineering at the Federal University of São Carlos as a requirement to obtain the degree of Doctor in Chemical Engineering.

Supervisor: Gabriela Cantarelli Lopes

Co supervisor: Gabriel Henrique Justi

SÃO CARLOS – SP

AUGUST, 2024

Ayuba, Nuhu

Application of CFD to Study the Dynamics of Droplets Expelled During Coughing / Nuhu Ayuba -- 2024.
120f.

Tese de Doutorado - Universidade Federal de São Carlos, campus São Carlos, São Carlos
Orientador (a): Gabriela Cantarelli Lopes
Banca Examinadora: Profa. Dra. Liliana de Luca Xavier Augusto, Profa. Dra. Marcela Kotsuka da Silva, Prof. Dr. Gabriel Henrique Justi, Profa. Dra. Vádila Giovana Guerra Béttega
Bibliografia

1. Eulerian-Lagrangian Model. 2. Cough Computational Fluid Dynamics. 3. Cough Respiratory Droplets. I. Ayuba, Nuhu. II. Título.

Ficha catalográfica desenvolvida pela Secretaria Geral de Informática (SIn)

DADOS FORNECIDOS PELO AUTOR

Bibliotecário responsável: Arildo Martins - CRB/8 7180

UNIVERSIDADE FEDERAL DE SÃO CARLOS

Centro de Ciências Exatas e de Tecnologia
Programa de Pós-Graduação em Engenharia Química

Folha de Aprovação

Defesa de Tese de Doutorado do candidato Nuhu Ayuba, realizada em 29/08/2024.

Comissão Julgadora:

Profa. Dra. Gabriela Cantarelli Lopes (UFSCar)

Profa. Dra. Liliana de Luca Xavier Augusto (UTFPR)

Profa. Dra. Marcela Kotsuka da Silva Camara Bastos (FURB)

Prof. Dr. Gabriel Henrique Justi (UNIPAMPA)

Profa. Dra. Vádila Giovana Guerra Béttega (UFSCar)

O Relatório de Defesa assinado pelos membros da Comissão Julgadora encontra-se arquivado junto ao Programa de Pós-Graduação em Engenharia Química.

ACKNOWLEDGMENT

First and foremost, I would like to express my deepest gratitude to my supervisor, Dr. Gabriela Cantarelli Lopes, for her invaluable guidance, continuous support, and encouragement throughout the development of this study. Her expertise and mentorship were fundamental to the success of this research.

I also extend my sincere thanks to my co-supervisor, Dr. Gabriel Henrique Justi, for his insightful suggestions and constructive feedback, which significantly enhanced the quality of this work.

I am grateful to the members of the examination committee—Prof. Dr. Liliana de Luca Xavier Augusto, Prof. Dr. Marcela Kotsuka da Silva Câmara Bastos, and Prof. Dr. Vadila Giovana Guerra Bettega—for their valuable time, contributions, and critical evaluation of this dissertation.

My heartfelt appreciation goes to my wife, Jady, and my daughter, Victória, for their unwavering support, patience, and understanding throughout this academic journey. I also extend special thanks to my brothers Minighom, Suleiman, and Seth in Nigeria, whose enduring encouragement and belief in my potential have always motivated me to strive for excellence in my academic pursuits.

A special acknowledgment is due to Dr. Toni Jefferson Lopes for his immeasurable support before, during, and after the completion of this research. I am also particularly thankful to my friend Habila Thomas Yusuf, who played a pivotal role in assisting with my doctoral application to São Carlos. Your support has always gone beyond friendship.

I would also like to thank Dr. Antonio Carlos Daltro de Freitas and Fernando Pedro Dias for their support at the onset of this research.

My sincere thanks to the African community in the cities of São Luís and São Carlos for enriching my social experience during this period—indeed, all work and no play makes Jack a dull boy.

Special thanks to my fellow doctoral colleagues Ricardo Arbach Fernandes de Oliveira, Victor Ferreira, and Karla Raphaela Braga de Melo for their technical assistance and support, especially in handling hardware and computer systems essential to this research.

I am also grateful to my friends Anacleto Domingos, Osmilde Miranda, Joseph Osei, Ojubanire Babatunde, Osires Bideu, Francisco Malungo, Kiabanga Zamba, and Elvis Kasanga, whose kind words and encouragement helped me through difficult times.

I would like to thank the coordination and staff of the Department of Chemical Engineering at UFSCar for providing the necessary infrastructure and a conducive environment for conducting this study.

This study was financed in part by the Coordenação de Aperfeiçoamento de Pessoal de Nível Superior - Brasil (CAPES) - Finance Code 001.

ABSTRACT

This study investigates the behavior of respiratory droplets in indoor environments, applying the Eulerian-Lagrangian method to improve understanding of droplet transmission in the context of Infectious Respiratory Diseases (IRDs). The research is divided into four key sections. The first part evaluates the effects of different turbulence models—SST k-ω, standard k-ε, and Reynolds Stress—on the evaporation of a single droplet, aiming to identify a model that is both precise and computationally efficient. The second part compares the use of graded tetrahedral and hexahedral meshes in simulating droplet behavior, assessing their relative effectiveness and computational cost. In the third part, the influence of phase coupling, droplet size, and relative humidity on the evaporation process is examined, while the fourth part explores the impact of wind boundary conditions on droplet dispersion. To further validate the findings, the models developed were applied under the climatic conditions of São Carlos, São Paulo, Brazil, to observe how the droplets behave in a real-world setting. The results demonstrate that hexahedral meshes provide more accurate droplet behavior representation compared to tetrahedral meshes, which showed discrepancies with previous studies. The effect of phase coupling was found to be minimal, with smaller droplets evaporating rapidly irrespective of ambient humidity, while larger droplets fell to the ground. The study also reveals that higher humidity levels slow down evaporation, with medium-sized droplets (around 50 μm) persisting longer and traveling farther—up to approximately 1.40 meters. This suggests a minimum social distancing distance in indoor, quiescent environments to minimize the transmission of IRDs. Additionally, smaller droplets evaporated quickly, and their dispersion increased at lower wind speeds. The research concludes that the no-slip boundary condition is more cost-effective for indoor simulations. These findings contribute valuable insights into understanding droplet behavior and optimizing models for IRD transmission analysis in indoor spaces.

Keywords: Eulerian-Lagrangian; Respiratory droplets; Tetrahedral and hexahedral mesh; Turbulence model; droplet evaporation; Relative humidity.

RESUMO

Este estudo investiga o comportamento das gotículas respiratórias em ambientes internos, aplicando o método Euleriano-Lagrangeano para melhorar a compreensão da transmissão de gotículas no contexto de Doenças Respiratórias Infecciosas (DRIs). A pesquisa está dividida em quatro seções principais. A primeira parte avalia os efeitos de diferentes modelos de turbulência—SST k-ω, k-ε padrão e Tensões de Reynolds—sobre a evaporação de uma única gotícula, com o objetivo de identificar um modelo que seja preciso e computacionalmente eficiente. A segunda parte compara o uso de malhas tetraédricas e hexaédricas graduadas na simulação do comportamento das gotículas, avaliando sua eficácia relativa e o custo computacional. Na terceira parte, é examinado o efeito do acoplamento de fase, o tamanho das gotículas e a umidade relativa sobre o processo de evaporação, enquanto a quarta parte explora o impacto das condições de contorno do vento na dispersão das gotículas. Para validar ainda mais os resultados, os modelos desenvolvidos foram aplicados nas condições climáticas de São Carlos, São Paulo, Brasil, para observar o comportamento das gotículas em um ambiente real. Os resultados demonstram que as malhas hexaédricas fornecem uma representação mais precisa do comportamento das gotículas em comparação com as malhas tetraédricas, que apresentaram discrepâncias com estudos anteriores. O efeito do acoplamento de fase foi encontrado como mínimo, com as gotículas menores evaporando rapidamente, independentemente da umidade ambiente, enquanto as gotículas maiores caíam ao chão. O estudo também revela que níveis mais altos de umidade desaceleram a evaporação, com gotículas de tamanho médio (cerca de 50 µm) persistindo por mais tempo e viajando mais longe—até aproximadamente 1,40 metros. Isso sugere uma distância mínima de distanciamento social em ambientes internos e tranquilos para minimizar a transmissão de DRIs. Além disso, gotículas menores evaporaram rapidamente e sua dispersão aumentou com velocidades de vento mais baixas. A pesquisa conclui que a condição de contorno de não-deslizamento é mais econômica para simulações em ambientes internos. Esses resultados contribuem com valiosas informações para entender o comportamento das gotículas e otimizar modelos para análise da transmissão de DRIs em espaços fechados.

Palavras-chave: Euleriano-Lagrangiano; Gotículas respiratórias; Malha tetraédrica e hexaédrica; Modelo de turbulência; Evaporação de gotículas; Umidade relativa.

LIST OF FIGURES

LIST OF TABLES

LIST OF ABBREVIATIONS AND ACRONYMS

2D ..... Two dimensional

3D ..... Three dimensional

BC ..... Boundary condition

CFL ..... Courant-Fiedrichs-Lewy

DNAs ..... Deoxyribonucleic acid

DRW ..... Discrete Random Walk model

FSM ..... Fractional Step method

GCI ..... Grid Convergence Index

IRDs ..... Infectious respiratory diseases

KHRT ..... Kelvin-Helmholtz, and Rayleigh-Taylor

LES ..... Large Eddy Simulation

PISO ..... Pressure-Implicit with Splitting of Operators

RANS ..... Reynolds-averaged Navier-Stokes

RNG k-ε ..... Re-Normalisation Group

RSM ..... Reynolds-stress models

SARS ..... Severe acute respiratory syndromes

SIMPLE ..... Semi-Implicit Method for Pressure-Linked Equations

SIMPLEC ..... SIMPLE-Consistent

SST k-ω ..... Shear Stress Transport

TAB ..... Taylor Analogy Breakup

TB ..... Tuberculosis

UDF ..... User Defined Function

LIST OF SYMBOLS

Latin symbols

A_d ..... Surface area of droplet [m^2]

$C_{w,\infty}$ .....Water concentration in the bulk gas [$kmol/m^3$]

$C_{w,d}$ .....Water concentration at the droplet surface [$kmol/m^3$]

$C_{1\varepsilon}$ ..... Production term of the the energy equation

C_2 .....Constant

$C_{2\varepsilon}$.....Dissipation term of the epsilon equation

C_c ..... Cunningham correction factor (dimensionless)

c_d ..... Heat capacity of the droplet [J/kg K]

C_D.....Drag coefficient

C_{ij} ..Convective transport term. Represents the change in Reynolds stress due to the mean flow [$kg/(m \cdot s^3$]

C_ε .....Constant

C_μ .....Turbulent viscosity constant

Dis_k ..... Dissipation of k

$D_{L,ij}$ .....Molecular diffusion term [$kg/m \cdot s^3$]

D_T Turbulent diffusion term [$kg/m \cdot s^3$]

D_v ..... Diffusion coefficient of vapor [m^2/s]

D_ω ..... Cross-diffusion term, Diffusive term of omega

d_p..... Damping coefficient [$N \cdot s/m$]

E_{child} ..... Energy of the child droplets

e_n ..... Coefficient of restitution

E_{Parent}.....Energy equation of parent droplet

$\vec{F}$. ..... Force vector [m/s^2]

F_1 .....Blending function

F_{ij} .....Additional source/sink terms [$kg/m \cdot s^3$]

F_{other} .....Other external forces acting on the mass [$kg/m \cdot s^3$]

f_β .....Function of B

$\widetilde{G}_k$.....Production of turbulent kinetic energy due to mean velocity gradients

G_b.....Generation of turbulence kinetic energy due to buoyancy

G_{ij} ..... Buoyancy production term [kg/m·s³]

G_k ..... generation of turbulence kinetic energy due to the mean velocity gradients

G_ω ..... Production of omega due to velocity gradients

h ..... coefficient of heat transfer [W m^2/ K]

$h_{d,g}$ ..... latent heat of vaporization (kJ/kg)

h_{fg} ..... Latent heat [kJ/kg]

h_g ..... Enthalpy of air [kJ/kg]

k ..... Turbulent kinetic energy, Spring constant [N/m]

K ..... Proportionality constant

k_c ..... Mass transfer coefficient [m/s]

L_3 ..... Cell length at level 3 [m]

L_e ..... Eddy length scale [m]

L_2 ..... Cell length at level 2

m ..... Mass of the particle [kg]

$\dot{m}$ ..... Mass flow [kg/s]

$\dot{m}_{d\rightarrow g}$ ..... Mass transfer rate [kg/s]

m_a ..... Component source term

M_{t0} ..... Initial turbulent Mach number

MW_w ..... Molecular weight of species [kg/ kmol]

n ..... Total number of cells applied

n_d ..... Density number [m^{-3}]

P ..... Pressure [Pa]

P_g ..... Air pressire Pressure [Pa]

P_{ij} ..... Production term [kg/m·s³]

P_{outlet} ..... Outlet pressure [Pa]

P_{sat} ..... Saturated vapor pressure [Pa]

P_{static} ..... Static Pressure [Pa]

P_{total} ..... Total pressure [Pa]

r ..... Mesh growth rate

R ..... Universal gas constant [Pa L/mol K]

R_β ..... Reynolds number for quantity beta

R_{ideal} ..... Ideal radius [m]

R_k ..... Reynolds number for k quantity

R_β ..... Constant

R_ω ..... Reynolds number for ω quantity

Re ..... Relative Reynolds number

S ..... Mean rate-of-strain tensor, Shape factor (dimensionless)

Sc ..... Schmidt number

Sh ..... Sherwood number

t ..... Time [s]

T ..... Integral time scale [s]

T_∞ ..... Temperature of the surrounding air [K]

T_b ..... Boiling temperature [K]

t_{cross} ..... Time needed for a particle to cross an eddy [s]

T_d ..... Respiratory droplet temperature [K]

$t_{interaction}$ ..... Interaction time [s]

T_L ..... fluid Lagrangian integral time [s]

T_v ..... Vapor temperature [K]

v ..... Velocity [m]

v' ..... Fluctuating component of the continuous phase velocity due to turbulence [m/s]

$\bar{v}$ ..... Mean velocity of the continuous phase [m/s]

$\vec{v}_d$ ..... Velocity of respiratory droples [m/s]

$\vec{v}_g$ ..... Velocity of the dispersed phase [m/s]

$v_{1,n}$ ..... of the particle befor collision [m/s]

$v_{2,n}$ ..... Velocity of the particle after collision [m/s]

v_d ..... Respiratory droplets velocity [m/s]

V_i ..... Cell volume [m^3]

V_{ideal} ..... Ideal volume [m^3]

v_{inlet} ..... Inlet velocity [m/s]

V_{real} ..... Real volume

v_{rel} ..... Relative velocity [m/s]

We ..... Weber number

x ..... Displacement of the mass from equilibrium [m]

$Y_{a,vap}$ ..... The respective mass fraction of vapor

Y_k ..... Turbulent dissipation of k

Y_ω ..... Turbulent dissipation of ω

Greek symbols

α_0 .....Constant related to turbulent kinetic energy

α_∞ .....Constant related to the rate of production and dissipation of turbulent kinetic energy

α_∞^* .....Constant related to the rate of production and dissipation of turbulent kinetic energy

β^*.....Turbulence model constant

β_∞^* .....Constant

$\Gamma_{k,\omega}$..... Effective diffusivity of k and ω

ε .....dissipation rate

ε_{ij} ..... Dissipation term [kg/m·s³]

ζ.....Normally distributed random number with zero mean and unit variance

λ .....Cough droplets mean free path [m]

μ_g ..... The molecular viscosity of the fluid [kg m^{-1} s^{-2}]

μ_t..... Turbulent viscosity [kg $m^{-1}.s^{-1}$]

ξ^* .....Constant, Model constant

σ.....Particle surface tension [N/m]

$\rho_{a,vap}$..... Vapor density [kg m^{-3}]

ρ_g ..... Density of the respiratory droplets [kg m^{-3}]

σ_k ..... Turbulente Prandtl for k

σ_ε ..... Turbulent Prandtl for ε

τ ..... Particle relaxation time [s]

$\bar{\bar{\tau}}_g$ ..... Viscous stress

τ_e..... Characteristic lifetime Eddy [s], Time scale [s]

φ_{ij} .....Pressure-strain correlation term [kg/m·s³]

SUMMARY

1. INTRODUCTION

Infectious respiratory diseases (IRDs) such as severe acute respiratory syndromes (SARS), tuberculosis (TB), influenzas (avian and swine) have been interest of study for a long time (Gupta et al., 2009 and Morawska, 2006). The rapid spread of SARS-CoV-2 virus, better known as the new Corona Virus disease (COVID-19) in the early 2020 (Kucharski et al., 2020) has intensified the need to elaborate more studies about IRD.

Currently, IRD studies are not just limited to the medical fields, but have also extended to others. For example, in Engineering, pathogens may not directly be studied. Instead, parameters that influence transportation of contaminated respiratory droplets are studied. Good examples of parameters that influence the spread of IRDs are the particle size and velocity. For instance, large droplets plunge to the ground when they are released, on the contrary, smaller droplets tend to travel larger horizontal distances. Additionally, climatic conditions such as relative humidity, temperature and wind velocity and direction contribute greatly to the spread of IRDs.

In this study, sometimes, simplifying the flow domains and the physical properties of the respiratory droplets are needed to reduce computational cost, yet providing results that are similar to real events. For instance, geometries used to carry out the flow studies are made in such a way to permit the application of coarser meshes. This is done by avoiding the use of curves to build the flow domains. To simplify the respiratory droplets, contents such as mass composition of virus (Branche et al., 2014; Honkinen et al., 2012; Wolfel et al., 2020) proteins, lipids, carbohydrates, DNAs and salts (Redrow et al., 2011) are neglected. Hence, respiratory droplets with the physical properties of pure water are applied.

To execute the CFD studies of droplets emitted during respiratory events, the application of the appropriate numerical models is important. Considerations in the transient formulation of the flow governing equations, turbulent models, multiphase flow formulation which depends on the number of phases applied, droplet evaporation, particle break (where applicable), droplet dispersion due to turbulence, droplet evaporation and boundary conditions should be made. These ample combination makes this study open for new findings.

This analysis is conducted to contribute to the existent results available in the literature. To this end, the CFD of respiratory droplets is studied using the ANSYS Fluent commercial software adopting the Eulerian-Lagrangian model.

It is divided in four parts. In the first part, the objective is to study turbulence effect on the evaporation of a single respiratory droplet. The (SST) k-ω, k-ε and Reynolds Stress (RSM) turbulence models are compared applying a 2D simulation. In the second part of the research, the objective is to build a 3D mesh, comparing two different types: the trihedral and hexahedral. In the third part of the research, the objective is to study the influence of air relative humidity on human cough droplet evaporation with the aim to use a 3D tetrahedral mesh to evaluate the evolution of the droplet at different relative humidity conditions. The last part has the quest to apply the tests carried out in previous parts of the research with the objective to study the behavior of the respiratory droplets under the climatic conditions of São Carlos, São Paulo, Brazil. In addition to, a complimentary study on behavior of the flow at different boundary conditions is carried out in this part of the research.

In summary, this study is expected to contribute to the understanding of the spread of viruses and bacteria carried by droplets, enabling the definition of standards and recommendations to reduce the transmission process of diseases caused by this transmission mechanism. Additionally, this study is also expected to aid in choice and application of the numerical models and meshes that can be applied in the CFD studies of respiratory droplets in closed and open environments.

2. LITERATURE REVIEW

2.1 Airborne transmission

Airborne transmission is a primary route for the spread of IRDs, where pathogens are expelled from an infected person through coughing, sneezing, talking, or breathing. They are expelled with the respiratory droplets. The larger droplets fall to the ground, medium droplets travel larger horizontal distances and small droplets evaporate instantly when they are released. Even though the liquid part of the droplets may evaporate totally, parts remain suspended in the air for extended periods in form of aerosols (Morawska and Cao, 2020) increasing the risk of inhalation by susceptible individuals. The image in Figure 1 shows how the droplets are classified when they are released into the surrounding.

Figure 1- Airborne transmission of IRDs

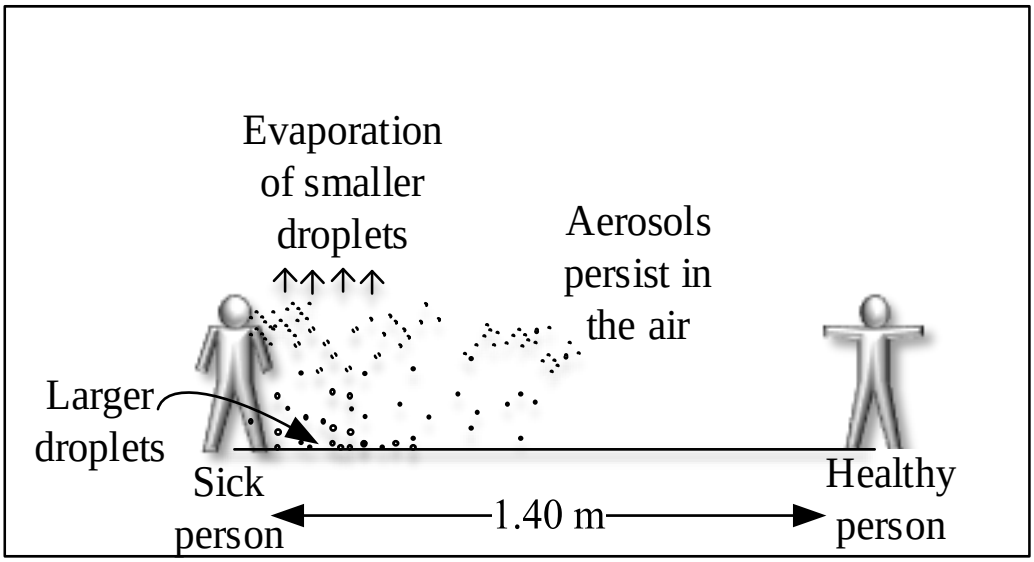

(Self-elaborated diagram with safe distance according to results of this work)

Apart from airborne transmission, contaminations can take place through fomites (Van Doremalen et al., 2020) and high-touch surfaces (Ong et al., 2020) which are surface contaminations. Contaminations can also take place through direct contact (Kwok et al., 2015; COVID, C., 2020).

2.2 CFD studies of respiratory events

CFD has become an important tool for studying the behavior of the droplets (Sedighi et al., 2023). One of the reasons for its regular application by the scientific community is its lower cost when compared to experimental methods (Chen et al., 2022 and Cao et al. 2022). The CFD studies of respiratory events have been carried out in two forms. The first involves the study of the behavior of the respiratory parameters within the human respiratory system. Classical examples are the studies carried out within the lungs and trachea of a human. For instance, authors like Faizal et al. (2020), Augusto et al. (2016), Tsega et al. (2018), Qi et al. (2014), Tsega et al. (2022) and Azarnoosh et al. (2016) have used CFD to carry out investigations that range from particle deposition on the respiratory tract to respiratory flow patterns (studied with specific flow parameters such as velocity, pressure, and shear stress). For external respiratory events, Oh et al. (2022), Chillón et al. (2023), Zee et al. (2021) and Li et al. (2018) have applied CFD to study the particles expelled from events such as coughing, sneezing, breathing, talking, etc.

To carry out these studies with more precision, the availability of experimental data (Zee et al., 2021) even though they are limited (Cao et al. 2022), the choice and application of adequate physical model (Li et al., 2018), solver (Walsh and Boyle, 2020; Li et al., 2021), boundary conditions (Dao et al., 2022 and Aliabadi et al., 2010), and adequate simplification and meshing of the flow domain (D'Alessandro et al., 2021 and Jiang, 2020) is important. Also, an adequate numerical model needs to be applied to calculate the evolution of the respiratory droplets under specific environmental conditions.

Eulerian-Lagrangian model has been applied by many authors like D'Alessandro et al. (2021), Dbouk and Drikakis (2020), Yan et al. (2019), Li et al (2020) and Li et al. (2018). Eulerian model solves the corresponding transport equations related to the continuous phase (Chen et al., 2022, Oh et al., 2022, D'Alessandro et al., 2021) while the Lagrangian model tracks and calculates each particle's position and velocity and updates them as they move through the flow field. (Xiao et al., 2023, Chéron et al., 2023, Zhang and Chen, 2007). In the CFD of respiratory events, the air

and water vapor make up the continuous phase (Eulerian phase) which is solved by the Eulerian model, while the droplets which are largely water form the Lagrangian phase (Chillón et al., 2023).

Regarding the computational tool applied to study the CFD of respiratory droplets, ANSYS Fluent, which is the commercial software is applied in this work, provides pressure and density-based solvers. The respiratory events fit into incompressible flows; therefore, the pressure-based solver can be applied. This solver offers coupled and segregated algorithms (ANSYS, 2013). The coupled algorithm solves the momentum and continuity equations in a coupled form while the segregated algorithm solves the flow equations individually.

The application of the coupled algorithm improves the convergence speed when compared to the segregated counterpart. However, the later algorithm requires lesser computational memory. Therefore, the time-cost factor puts the coupled scheme at an advantage over the segregated one. In the coupled algorithm, the SIMPLE, SIMPLEC, PISO, coupled, and FSM are the pressure-based coupling schemes available in the commercial software adopted in this study. Some of these have been reported in literature; SIMPLE by Cao et al. (2022) and Oh et al. (2022). while D'Alessandro et al used PISO, which is recommended for transient calculations which permits the application of large time-steps, and highly distorted mesh (ANSYS, 2013).

2.3 Boundary characterization

In general studies of CFD of respiratory events, setting up boundary conditions is crucial to obtaining qualitative results (Chen et al.,2022 and Li et al., 2023). The boundary conditions include the characteristics attributed to the velocity inlets, pressure outlets, stationary or moving walls and the flow space. Gupta et al. (2009) have highlighted flow direction, respiratory surface area, temperature, and respiratory droplet size distribution as the specific boundary conditions. The respiratory particles can be emitted in the direction normal to the respiratory surface area, as applied in the works of Redrow et al. (2011) and Bourouiba et al. (2014), or inclined at a specific angle as discussed by Oh et al. (2022) and Gupta et al. (2009). The inclined surface inlets may approximate the reality since exhalation from mouth region is sometimes not normal to the y-axis (Figure 2). However, many researchers use injections normal to the y-axis due to its

economic advantage since they reduce the complexity of the geometry at the inlet, thereby reducing the number of elements applied in the meshing process.

Figure 2- The direction of the injection of the respiratory droplets

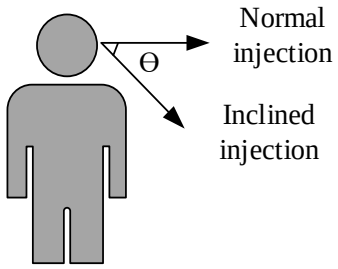

(Self-elaborated)

The temperature of the respiratory droplets injected into the flow domain is analogous to the human body temperature. For instance, Redrow et al. (2011) and Chillón et al. (2023) have applied 310.15K while Oh et al., (2021) have applied 307.15K. The first group of authors have applied the standard body temperature while the second have applied the temperature of the body at rest. As for the ambient temperature and humidity applied in the CFD studies, different values have been applied by researchers; specifically, characterized by where the research was conducted.

2.4 Droplet size and distribution

Even though there are studies on drops size distribution, the inconsistencies in the values presented by authors make it difficult to elaborate concise studies about fluid dynamics of respiratory events. Undoubtedly, the inconsistencies arise from different factors such as physiological state of people, environmental factors and stages of contamination (for instance at advanced stages of IRDs, coughs and sneezes are normally more violent). To explain the physiological factor, Han et al. (2013) presented results showing that heights, weights and gender influenced the forced vital capacities (FVCs measured in ml) of sneezes. That is to say; a respiratory activity may present different particle sizes depending on the aforementioned factors. Additionally, patients at advanced stages of contamination tend to release larger and higher concentrations of

droplets. In terms of particle sizes emitted, no standards have been established (Scharfman et al., 2016). Therefore, Li et al. (2018) have used sizes ranging from 10 to 100 μm for cough droplets. Gralton et al. (2011) and Perella et al. (2020) have studied 1-500 μm. Wei and Li (2015) discussed cough particle sizes that range from 1 to 1000 μm. Weber and Stilianakis (2008) have applied a large range of 1-2000 μm; this range covers most of the rage analyzed by the CFD of IRDs community. Other authors that have contributed contributed significantly include Yang et al. (2007), Zhang et al. (2019) and Lee et al. (2019.

In general, larger respiratory droplets fall to the ground immediately after they have been released (Redrow et al., 2011; LI et al., 2018 and Chillón et al., 2023). On the other hand, smaller droplets persist in the air for a longer period (Bourouiba et al., 2014).

In this study, droplets of 1 μm, 10 μm, 50 μm, 100 μm, 200 μm and 500 μm, which represent a range of particles were used. The range of droplet sizes are distributed so that effect of relative humidity, droplet size and wind velocity and other parameters can be studied within a wide range of particle size distribution.

2.5 Computational domain and meshing

The domain strategic reduction is also a crucial step towards achieving modeling and simulation with lower computational cost. The domain reduction involves the removal of unnecessary sections such as the human parts of the body that have no direct impact on the simulation results. Such a strategy reduces computational cost (Cao et al., 2022 and Duan et al., 2015). In most of the indoor studies of respiratory events, the whole computation domain (which is a representation of closed surroundings like a room) is represented by a rectangular geometry. The inlet of such geometry (which in reality is the human mouth) is represented by simple geometries in the literature. For instance, a rectangular inlet has been applied in the work of Chillón et al., (2023) and D'Alessandro et al. (2021), a circular one has been used in the work of Oh et al. (2022), Li et al. (2018) and Redrow et al. (2011), a squared inlet has been used by Gupta et al. (2009) and Pan et al. (2022), and lastly, ellipse has been applied in the work of Oh et al. (2021). The use of simple geometries makes meshing more convenient at the domain inlet, since relatively

coarser cells can be applied (Cao et al., 2023). In general, it has not been reported that the inlet geometry influences in a large scale, however, it reflects in the computational cost.

After a proper domain reduction, numerical meshing is the next step. It has been observed that in the literature, authors have applied different kinds of meshes to carry out the CFD of respiratory events. These meshes have been built with tetrahedral, hexahedral, and polyhedral elements. At this point it is important to highlight that mesh building is not limited to the application of the aforementioned elements, but can also be carried out with prismatic and pyramidal elements (Baldan et al., 2023). Even though the later elements are not frequently applied, they appear in negligible proportions during meshing. Faleiros et al. (2022), Yan et al. (2019) and Redrow et al. (2011) have used tetrahedrons to discretize their flow domains to study the CFD of respiratory events. On the other hand, Chillón et al. (2023), Cao et al. (2022), D'Alessandro et al. (2021), Dbouk et al. (2020) and Li et al. (2018) have applied hexahedral mesh in their studies. Lastly, Oh et al. (2022), Zee et al. (2021) and Li et al. (2020) have used polyhedral mesh. All the aforementioned researchers have meshed their flow domains with different numbers of elements ranging from hundreds of thousands to units of millions of mesh cells. This means they might be working at different ranges of precision, depending on whatever criteria each researcher must have adopted.

It has been noticed that authors have applied a different element-domain volume relationship. Redrow et al. (2011) have used 500,000 elements to mesh a 17.94 m^3 domain (~ 31,000 elements/m^3); Chillón et al. (2023) have used 877,000 elements to mesh their 50.4 m^3 flow domain (~ 17,000 elements/m^3); D'Alessandro et al. (2021) applied 6 million cells to mesh their 12 m^3 flow domain (~ 500,000 elements/m^3), and Oh et al. (2022) have applied about 500,000 elements to mesh a 14.4 m^3 flow domain (~ 35,000 elements/m^3). The element-domain volume relationships mentioned above reflect the complexity of each scenario. For instance, a domain containing one human is simpler than one with two, and an empty room is less complex than an airplane cabin. The various studies by the mentioned authors were conducted under different conditions. Consequently, it is expected that more complex domains will have higher mesh densities regardless of their dimensions.

In the CFD studies of respiratory activities, the choice of cell geometry to build a mesh is influenced by on the complexity of the flow geometry or the cost, above all, to obtain an accurate result. For instance, it is difficult to apply hexahedrons (which are orthogonal cells) to build mesh on complex geometries (Wang, 2021), even though they have a reduced error approximation to the surface normal gradient, when compared to tetrahedrons and polyhedrons (Baudouin et al., 2014 and Benzle et al., 1995), in other words, the hexahedral meshes yield more accurate solutions than their tetrahedral counterparts for the same number of elements (Biswas, 1998). However, since most of the studies in this field are carried out with simplified geometries that can be meshed up with almost all forms of geometries available, the choice of application is more influenced by computational cost.

In some literature, the inlet region (which represents the human mouth in reality) of the computational domain is meshed with the highest cell density. A gradual increment in average cell size is observed while moving away from that region (Figure 5). Therefore, the coarsest elements are found in the farthest regions away from the inlet.

Figure 3- Graded mesh with quadrilateral elements (2D) or hexahedral elements 3D

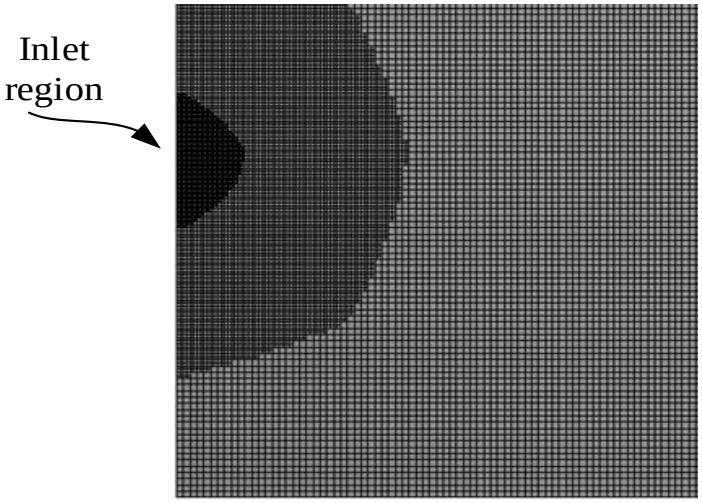

(self-elaborated)

The reason for applying this form of mesh grading is to achieve a more accurate discretization of the droplets and transport equations (D'alessandro et al., 2021). When the Discrete

Particle Model (DPM) is applied to track the motion of each respiratory droplet using a surface injection in commercial software like Fluent, each face cell at the inlet region releases a single particle per DPM flow time (Fluent, 2013).

The measure of quality is eminent in every numerical mesh generated to solve any CFD problem. In the software used to elaborate this work, mesh quality measurement can be carried out through measuring metric factors such as orthogonality, skewness, aspect ratio, warping, element quality among other prominently factors. Table 3 presents different parameters to evaluate the quality of mesh.

Accessing mesh details is important because it is an important criterion of precision (Baudouin et al., 2014) that reflects in the modeling and simulation results. In this research, the skewness has been mostly used to measure the quality of mesh. As a complement to Table 3, this measurement of mesh quality is explained thus.

The measure of the quality of mesh was carried out through the evaluation of the skewness which compares a cell geometry applied in meshing to an ideal cell geometry. For instance, the ideal tetrahedral and hexahedral cells are respectively formed with equilateral triangular and orthogonal quadrilateral faces. Therefore, the skewness for each cell geometry is measured differently.

For a tetrahedral cell, the skewness is calculated from Eq. 2.11 which is the ratio of the real cell volume to the ideal volume.

$$Skewness = 1 - \frac{V_{real}}{V_{ideal}} \qquad 2.11$$

The real cell volume always satisfies the limit $V_{real} \leq V_{ideal}$. The volumes of the ideal and real cells are respectively calculated by the relation $V_{ideal} = 0.5132R_{ideal}^3$, where R_{ideal} is the radius of the external sphere formed around the tetrahedral cell as shown in Figure 3 (a) ii. To calculate the real volume of (i), the same relation is used.

Table 1- Mesh quality measurement

Mesh metric	Description	Accepted range
Orthogonality	Measures the angle between the cell faces and the vector connecting the cell centers. Good orthogonality means that these vectors are perpendicular (or close to it), which helps in minimizing numerical diffusion and ensuring accurate flow calculations.	Values above 0.7 are generally considered good, but the acceptable range may vary depending on the specific application and solver settings
Aspect ratio	Expresses ratio of the longest edge length to the shortest edge length of a cell. High aspect ratio cells can lead to inaccuracies in the solution, especially in regions with high gradients.	Values below 5-10 are generally acceptable, but this can vary depending on the flow conditions and solver.
Cell quality	Often based on the deviation of the cell shape from an ideal shape (e.g., an equilateral tetrahedron for 3D tetrahedral meshes). The quality metric can be calculated using different methods, such as the equiangular skew or the ratio of the cell volume to the volume of an ideal cell with the same circumscribing sphere.	It ranges from 0 (worst) to 1 (best).
Skewness	Measures how much a cell deviates from an ideal shape (e.g., a perfect square in 2D or a cube in 3D). High skewness can lead to numerical errors and convergence issues	Zero (0) is the ideal value. Values below 0.5 are generally considered good; values above 0.9 are often problematic.

(Adapted from ANSYS, 2013).

The skewness of a hexahedral cell measures the deviation of the angles between face pairs from the ideal 90° vertex angles of a perfect hexahedron. The ideal and distorted hexahedral

cell geometries are depicted in Figure Figure 6 (b) i and ii, respectively. For hexahedral cells, the value of skewness is calculated by the relation in Eq. 2.12.

$$skewness = max\left(\frac{\theta_{max} - \theta_e}{180 - \theta_e}, \frac{\theta_e - \theta_{min}}{\theta_e}\right) \quad 2.12$$

where θ_{max} and θ_{min} are the maximum and minimum angles formed by the distorted cells, which are non-orthogonal in this case. θ_{min} is the angle for an equiangular cell (60 for a triangle, 90 for a square) (ANSYS, 2012).

Figure 4- Diagrams of skewed and ideal (a) tetrahedral and (b) hexahedral elements that are used to form numerical meshes

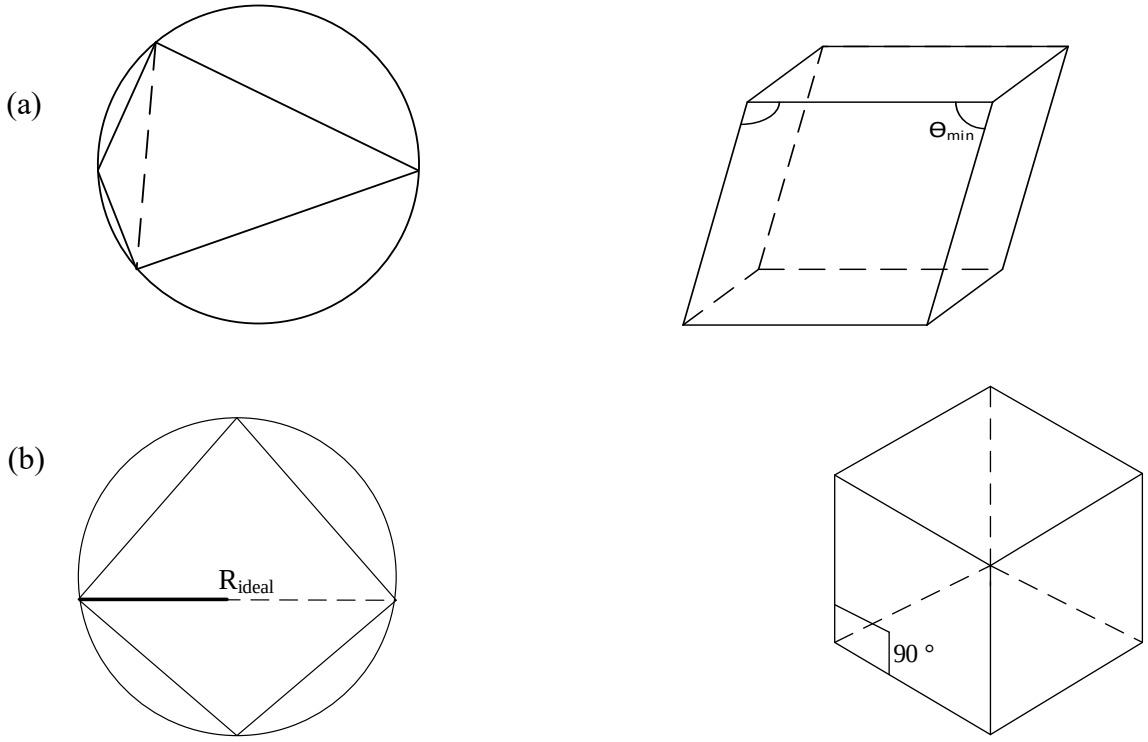

(Adapted from ANSYS, 2012)

For both tetrahedral and hexahedral meshes, the skewness value ranges from 0 to 1. Generally, a mesh is considered to be of higher quality when its skewness values are closer to 0. It

is typically recommended that simulations are performed using meshes with an average skewness value below 0.5 (ANSYS, 2012).

2.6 Discrete Particle Model (DPM)

Discrete Particle Model in Computational Fluid Dynamics is a numerical method used to track individual particles in a fluid flow. It is used to simulate the behavior of particles, such as their motion, interaction with each other, and interaction with the surrounding fluid (Li et al., 2020).

In DPM surface injection, each mesh-cell at the surface of the inlet represents a particle. Therefore, each mesh-cell injects one particle per unit time into the flow domain.

When a large number of particles is injected into the respiratory domain, the computational cost increases, because an explicit numerical scheme may require a lower time step to keep the Courant-Fiedrichs-Lewy (CFL) number low enough to avoid numerical inaccuracy. This particular dimensionless number is related to the velocity u, timestep (t) and the element size (x) (Eq. 2.13).

$$CFL = \frac{vDt}{Dx} \tag{2.13}$$

CFL sets restrictions on fluid particles so that they move within one grid length (Ferziger et al., 2019) to avoid inaccurate solutions in explicit integral schemes. However, the implicit scheme permits the application of higher CLF numbers (Blazek, 2015, and Miettinen and Siikonen, 2015). For instance, CLF value of 25 has been applied by Faleiros et al. (2022). However, the application of CFL below the unit value is recommended. In the work of Dbouk and Drikakis (2020), it was observed that $CLF_{max} > 0.2$ produced slight discrepancies in particle cloud properties trajectory despite applying an implicit formulation.

2.7 Turbulence model

Among other important considerations to make in the CFD studies of respiratory droplets emitted during respiratory droplets, selecting a suitable turbulence model is also important

(Liu et al., 2013 and Cao et al., 2022). The Large Eddy Simulation (LES) and Reynolds-averaged Navier-Stokes (RANS) are prominently applied in this type of study. In the work of Cao et al. (2022), the two methods have been studied and the authors concluded that even though the LES model gives a more accurate result, it has a higher computational cost when compared to the RANS models. It is known that the computational cost is an important factor when carrying out CFD studies of respiratory events. However, such consideration becomes secondary when it risks the precision of the results.

The commercial software applied in this study offers several RANS turbulence models, that extend from the one-equation Spalart Allmaras model to the most elaborate second-order closure model; the Reynolds Stress Model (RSM). Nevertheless, the k-ε and k-ω have been frequently applied. The authors in Table 4 have used different kinds of RANS turbulence model to carry out their research.

Table 2- Some turbulence models applied in the CFD studies of respiratory droplets

	Turbulence models			
	(SST) k-ω	RNG k-ε	Realizable k-ε	Standard k-ε
Authors	-Cao et al. (2022) -Faleiros et al. (2022) -Dbouk and Drikakis (2020)	-Cao et al. (2022) -Li et al. (2018) and Redrow et al. (2011) -Yan et al. (2019)	-Cao et al. (2022) -Oh et al. (2022) -Zee et al. (2021)	-Cao et al. (2022)

(self-elaborated)

Even though all the models present satisfactory results, the (SST-k-ω) has been recommended by Faleiros et al. (2022). The reason behind the recommendation is the fact that it ensures proper zone selection and modeling without any user interference. In such a model, the turbulence is solved using k-ε in the near-wall regions, while k-ω is activated in regions far from

the wall (Menter, 2003). Such a model could increase the precision at the inlet (mouth) region since it has a high cell density.

3. STUDY OBJECTIVE

The main objective of this research is to apply the Eulerian-Lagrangian to carry out the CFD studies of droplets emitted during respiratory events using the commercial software FLUENT 14.5.

Specifically, the objective of the research is divided into four parts:

First Part (Section 6):

I. Objective: Study the effect of turbulence on the evaporation of a single respiratory droplet.

II. Details: Compare the SST k-ω, k-ε, and Reynolds Stress (RSM) turbulence models using a 2D simulation.

Second Part (Section 7):

III. Objective: Conduct a 3D mesh analysis.

IV. Details: Compare two prominent meshes (tetrahedral and hexahedral) applied in CFD studies of droplets emitted during human respiratory events.

Third Part (Section 8):

V. Objective: Investigate the influence of phase coupling, droplet diameter and relative humidity on human cough droplet evaporation.

VI. Details: Use a 3D tetrahedral mesh to calculate the evolution of droplets at different relative humidity conditions.

Fourth Part (Section 9):

VII. Objective: Apply the tests results from previous research (Firs Part, Second Part and Third part).

VIII. Details: Study the behavior of respiratory droplets under the climatic conditions of São Carlos city, São Paulo State, Brazil, and conduct a complementary study on flow behavior at different boundary conditions.

4. MATHEMATICAL MODEL

4.1 Eulerian model

In this research, a multiphase-phase flow is conducted, therefore the mathematical model is built to calculate the conservation of mass, momentum and energy for each component of the flow. The air and water vapor make up the continuous phase in this research. Therefore, a single conservation of mass is given by Eq. 4.1.

$$\frac{\partial(\rho_g)}{\partial t} + \nabla \cdot \left(\rho_g v_g\right) = \dot{m}_{d\to g} \tag{4.1}$$

where ρ_g denotes the density (kg m^{-3}) of the continuous phase, t represents the time (s) and v_g represents the mass-averaged velocity (m s^{-1}). The term $\dot{m}_{d\to g}$ stands for the mass transfer rate through evaporation from the discrete phase (which is composed of the respiratory droplets) to the continuous phase which is as a result of coupling between the continuous and discrete phases (kg m^{-3} s^{-1}).

As the continuous phase is a multicomponent mixture of air and water vapor, the density, ρ_g, varies according to the mixture rule defined in Eq. 4.2.

$$\rho_g = \sum Y_i \rho_i \tag{4.2}$$

where Y_i and ρ_i are the mass fraction and the density of specie *i* in the mixture, respectively.

The momentum conservation of the Eulerian phase can be represented by Eq. 4.3.

$$\frac{\partial\left(\rho_g v_g\right)}{\partial t} + \nabla \cdot \left(\rho_g v_g v_g\right) = -\nabla P_g + \nabla \cdot \bar{\bar{\tau}}_g + F_g + S_g \tag{4.3}$$

The terms $P_g, \bar{\bar{\tau}}_g$ and F_g respectively represent pressure (Pa), viscous stress, volumetric force, source term for momentum exchange between the continuous and discrete phase. Given that the respiratory case study in this work is turbulent, the phase stress tensor ($\bar{\bar{\tau}}_g$) is defined by Eq. 4.4.

$$\bar{\bar{\tau}}_g = \mu_g \left[\left(\nabla v_g + \nabla v_g^T \right) - \frac{2}{3} \nabla \cdot v_g \bar{\bar{I}} \right] \tag{4.4}$$

where $\left(\nabla v_g + \nabla v_g^T \right)$ term represents the rate of strain tensor, which is symmetric and accounts for the deformation (both shear and elongation) of the fluid. $\bar{\bar{I}}$ is the identity tensor, a unit matrix that preserves the dimensional integrity of the terms in the equation. The second term on the right-hand side represents the effect of volume dilation.

The energy conservation of the continuous phase is given by Eq. 4.5, accounting for the internal energy change due to pressure, viscous effects, and heat flux.

$$\frac{\partial \left(\rho_g h_g \right)}{\partial t} + \nabla \cdot \left(\rho_g v_g h_g \right) = \nabla \cdot \left(\bar{\bar{\tau}}_g \cdot v_g \right) - \nabla \cdot q_g - \dot{m}_{d \to g} h_{d,g} \tag{4.5}$$

where the first and the second terms of Equation 15 represent the local time rate of change of the enthalpy per unit volume and the convective transport of enthalpy, respectively. The first and the second terms on the right-hand side of the equation represent the rate of work done by viscous stresses and the divergence of the heat flux, which can include conductive and possibly viscous dissipation components. $\dot{m}_{d \to g}$ and $h_{d,g}$ are the mass transfer rate from the droplet to vapor and the latent heat of vaporization. This is also the source term which results from the exchange of energy between the discrete phase and the continuous phase.

Finally, the Eulerian phase component mass balance is given by Eq. 4.6.

$$\frac{\partial (Y_i \rho_g)}{\partial t} + \nabla \cdot \left(\rho_g v_g Y_i \right) = - \nabla \cdot J_i + S_i \tag{4.6}$$

where Y_i is the mass fraction of the specie *i*, S_i is the component source term, and J_i is the diffusion flux of specie *i*, which arises due to gradient of concentration. This is given by Eq. 4.7.

$$J_i = -\left(\frac{\mu_g}{Sc_g} + \frac{\mu_{g,t}}{Sc_{g,t}}\right)\nabla \cdot Y_i \qquad 4.7$$

where μ_g and $\mu_{g,t}$ are respectively air viscosity and its turbulent contribution. Sc_g and $Sc_{g,t}$ are the respective molecular Schmidt number and its turbulent contribution.

While there are several methods to conduct turbulent CFD simulations, each has its application advantages and limitations. These approaches are Reynolds-Averaged Navier-Stokes (RANS), Large Eddy Simulation (LES), and Direct Numerical Simulation (DNS).

RANS is the simplest and the most popular method to solve turbulence in fluid flows. The idea about this method is that; since turbulent flows are unpredictable and occur over large-scale range of length and time, it becomes necessary to work with time-average of the equations governing the flow. For real fluids, the instabilities observed in the flows can be measured through interaction of non-linear inertial terms and viscous term contained in the flow equations. Through averaging, the aforementioned complexities add-up to RANS transport equations to form unknown variables or second moments. Therefore, higher-order correlations are needed to solve the unknown flow variables. However, the variables need to be supplemented before any solution can be obtained. Hence, algebraic or differential relations (also known as turbulent closures) are needed through defining a number of auxiliary equations.

RANS closure usually focuses on modeling Reynolds stress tensor (Perot and Wang, 1999). The method offers the most economic means of solving complex turbulent industrial flow problems. In this approach, turbulence modeling is achieved through Reynolds' decomposition of flow variables into average and fluctuating parts, respectively. Further substitution of the Reynolds-decomposed variables in the Navier-Stokes equation and taking an average result to an unknown Reynold stress tensor. This unknown force is modelled in order to obtain a solution (Afonsi, 2009).

Typical examples of closure models that can be applied to solve RANS equations include Spalart-Allmaras One-Equation, k-ε, k-ω, Reynolds Stress Model (RSM), Laminar-Turbulent Transition Models, among others. Although all of them can be applied specifically to

solve turbulent flow equations, the approach of algebraic closure adopted in each method to solve Reynolds's tensor vary.

4.1.1 *Standard $k-\varepsilon$ turbulence model*

The $k-\varepsilon$ is semi-empirical, therefore, its derivation depends on phenomenological or empirical considerations. It is modeled based on transport equations for turbulent kinetic energy (k) and its dissipation rate (ε). Its robustness, considerable accuracy and economy in solving a wide range of engineering flows and heat transfer are some of the reasons why it is applied frequently in simulations.

In the derivation of standard $k-\varepsilon$, it is assumed that the flow is fully turbulent, and the effects of molecular viscosity are negligible. This method is only valid for fully turbulent flows. Thus, the turbulent kinetic energy (k) and dissipation rate (ε) are obtained from Eqs. 4.8 and 4.9.

$$\frac{\partial}{\partial t}(\rho k) + \nabla.(\rho k v) = \nabla.\left[\left(\mu + \frac{\mu_t}{\sigma_k}\right)\nabla k\right] + G_k + G_b - \rho\varepsilon + S_k \tag{4.8}$$

$$\frac{\partial}{\partial t}(\rho \varepsilon) + \nabla.(\rho \varepsilon v) = \nabla.\left[\left(\mu + \frac{\mu_t}{\sigma_\varepsilon}\right)\nabla \varepsilon\right] + C_{1\varepsilon}\frac{\varepsilon}{k}(G_k + C_{3\varepsilon}G_b) - C_{2\varepsilon}\rho\frac{\varepsilon^2}{k} + S_\varepsilon \tag{4.9}$$

At high Reynolds number, the viscosity term is solved by combining k and ε as presented in Eq. 4.10.

$$\mu_t = \rho C_\mu \frac{k^2}{\varepsilon} \tag{4.10}$$

where G_k and G_b represent the generation of turbulence kinetic energy due to the mean velocity gradients and generation of turbulence kinetic energy due to buoyancy, calculated as described in Modeling Turbulent Production in the k- ε Models of Fluent (2013). σ_k and σ_ε are the turbulent Prandtl numbers for k and ε, respectively. S_k and S_ε are user-defined source terms. The

constants $C_\mu = 0.09,\ C_{1\varepsilon} = 1.44,\ C_{2\varepsilon} = 1.92,\ C_\mu = 0.08,\ \sigma_k = 1.0$ and $\sigma_\varepsilon = 1.3$ have been determined from experiments for fundamental turbulent flows, and are widely accepted and used as default values for viscous models.

4.1.2 *Shear stress transport (SST) k-ω*

The (SST) k-ω was developed by Menter et al. (2003) in order to eliminate the boundary condition dependency, which the model has with respect to free fluid flow. It is similar to the standard k-ε model. The only peculiarity lies in some adjustments the model incorporates. In (SST) k-ω, standard k-ε and k-ω are multiplied by a unit blending function which is designed to activate either of the models depending on the region where the turbulence would be solved near the walls or away from it (Menter et al., 2003).

Transport equations for SST k-ω model are represented by Eqs. 4.11 and 4.12.

$$\frac{\partial}{\partial t}(\rho k) + \nabla.(\rho k v) = \nabla.(\Gamma_k \nabla k) + \tilde{G}_k + Y_k \tag{4.11}$$

$$\frac{\partial}{\partial t}(\rho \omega) + \nabla.(\rho \omega v) = \nabla.(\Gamma_\omega \nabla \omega) + G_\omega + Y_\omega \tag{4.12}$$

where v, Γ_k and Γ_ω are the velocity and effective diffusivity of k and ω. $\tilde{G}_k$, and G_ω generation of turbulence due to mean velocity gradients in k and ω. Y_k and Y_ω represent turbulent dissipation of k and ω. The term D_ω represents a cross-diffusion term. The effective diffusivity of k and ω as are given by Eqs. 4.13 and 4.14.

$$\Gamma_k = \mu_g + \frac{\mu_{g,t}}{\sigma_k} \tag{4.13}$$

$$\Gamma_\omega = \mu_g + \frac{\mu_{g,t}}{\sigma_\omega} \tag{4.14}$$

The σ_k and σ_ω are the turbulent Prandtl numbers for k and ω. The term $\mu_{g,t}$ stands for the turbulent viscosity and is computed by Eq. 4.15.

$$\mu_t = \alpha_\infty^* \left(\left. 0.024 + \frac{\rho k}{6\mu\omega} \right/ 1 + \frac{\rho k}{6\mu\omega} \right) \tag{4.15}$$

For turbulent flows, $\alpha_\infty^* = 1$ (Eqs. 4.16 to 4.22 are all functions of μ_t).

$$\sigma_k = \frac{1}{\frac{F_1}{\sigma_{k,1}} + \frac{1 - F_1}{\sigma_{k,2}}} \tag{4.16}$$

$$\sigma_\omega = \frac{1}{\frac{F_1}{\sigma_{\omega,1}} + \frac{1 - F_1}{\sigma_{\omega,2}}} \tag{4.17}$$

$$F_1 = tanh\left\{ min\left[max\left(\frac{\sqrt{k}}{0.09\omega y}, \frac{500\mu}{\rho y^2 \omega} \right), \frac{4\rho k}{\sigma_{\omega,2} D_\omega^+ y^2} \right] \right\} \tag{4.18}$$

$$D_\omega^+ = max\left(2\rho \frac{1}{\sigma_{\omega,2}} \frac{1}{\omega} \frac{\partial k}{\partial x_j} \frac{\partial \omega}{\partial x_j}, 10^{-10} \right) \tag{4.18}$$

$$\tilde{G}_k = \min\left(G_k, 10\rho\beta^* k\omega \right) \tag{4.19}$$

In a manner of Boussinesq hypothesis,

$$G_k = \mu_t S^2 \tag{4.20}$$

Where *S* is mean rate-of-strain tensor. And

$$G_\omega = \tilde{G}_k \frac{\alpha}{v_t} \tag{4.21}$$

For SST $k-\omega$,

$$\alpha_\infty = F_1\left(\frac{\beta_{i,1}}{{\beta_\infty}^*} - \frac{k^2}{\sigma_{w,1}\sqrt{\beta_\infty^*}}\right) + (1-F_1)\left(\frac{\beta_{i,2}}{{\beta_\infty}^*} - \frac{k^2}{\sigma_{w,2}\sqrt{\beta_\infty^*}}\right) \quad 4.22$$

Equations 4.24 to 4.27 are functions of k dissipation (Dis_k).

$$Dis_k = \rho\beta^* f_\beta k\omega \quad 4.23$$

$$f_\beta = \begin{cases} 1 & x_k \le 0 \\ \frac{1+680x_k^2}{1+400x_k^2} & x_k \ge 0 \end{cases} \quad 4.24$$

$$x_k = \frac{1}{3}\frac{\partial k}{\partial x}\frac{\partial w}{\partial x} \quad 4.25$$

$$\beta^* = \beta_i^*[1+\xi^* F(M_t)] \quad 4.26$$

$$\beta_i^* = \left[\frac{0.27\left(Re_t/Re_\beta\right)^4}{1+(\frac{Re_t}{Re_\beta})^4}\right] \quad 4.27$$

where $R_\beta = 8, \beta_\infty^* = 0.09$ and $\xi^* = 1.5$

Equations 4.29 to 4.34 are functions of dissipation of ω (Dis_ω).

$$Dis_\omega = \rho\omega^2\beta f_\beta \quad 4.28$$

$$\beta = \beta_i\left[1-\frac{\beta_i^*}{\beta_i}\xi F(M_t)\right] \quad 4.29$$

$$F(M_t) = \begin{cases} 0 & M_t \le M_{t0} \\ M_t^2 - M_{t0}^2 & M_t > M_{t0} \end{cases} \quad 4.30$$

$$f_\beta = \frac{1 + 70x_\omega}{1 + 80x_\omega} \quad 4.31$$

$$x_\omega = \left| \frac{Q_{ij}\Omega_{jk}S_{ki}}{(\beta_\infty^* \omega)^3} \right| \quad 4.32$$

$$M_t^2 = \frac{2k}{\gamma RT} \quad 4.33$$

$$Q_{ij} = \frac{1}{2}\left(\frac{\partial u_i}{\partial x_j} - \frac{\partial u_j}{\partial x_i} \right) \quad 4.34$$

where at high Reynolds numbers, $\beta_i^* = \beta_\infty^* = 0.09, M_{t0} = 0.25, \alpha_\infty^* = 1, \alpha_\infty = 0.52, \alpha_0 = \frac{1}{9}, \beta_i = 0.072, R_{\beta,}\ R_k = 6, R_\omega = 2.95, \xi^* = 1.5, \sigma_k = 2.0, \sigma_\omega = 2021.$

Since SST k-ω is based on both standard k-ω and $k - \varepsilon$, in order to blend the two models together, $k - \varepsilon$ has been transformed into k and -ω equations which resulted in the inclusion of diffusive term D_ω as represented by Eq. 4.35.

$$D_\omega = \frac{2\rho(1 - F)}{\omega \sigma_{\omega,2}} \frac{\partial k}{\partial x_j} \frac{\partial \omega}{\partial x_j} \quad 4.35$$

4.1.3 *Reynolds stress model (RSM)*

These models do not use Eddy Viscosity hypothesis. However, they model transport equations for all components of the Reynolds stress tensor and dissipation rate in the fluid. They are suitable for complex flows since it includes effects of streamline curvature, sudden changes in

the strain rate, buoyancy flows compared to (SST) k-ω and Realizable $k-\varepsilon$. Specifically, they model solves 5 viscous Equations. Nevertheless, researches have shown that Reynolds Stress model is not superior to two-equation models, especially in anisotropic flow.

The momentum equation is given by Eq. 4.36.

$$\frac{\partial \rho\left(\overline{v_i{}' v_j{}'}\right)}{t} + C_{ij} = -D_{T,ij} + D_{L,ij} + \varphi_{ij} - \varepsilon_{ij} \qquad 4.36$$

where $\partial \rho v_i{}' v_j{}' / \partial t$ is a local derivative, C_{ij} is the convective term, $-D_{T,ij}$ is the turbulent diffusion, $D_{L,ij}$ is the molecular diffusion, , φ_{ij} is the pressure strain, $-\varepsilon_{ij}$ is dissipation. In the model, the terms C_{ij}, $D_{L,ij}$, $-P_{ij}$ and $-F_{ij}$ are calculated. On the other hand, $-D_{T,ij}$, $-G_{ij}$, φ_{ij} and $-\varepsilon_{ij}$ are modeled. Details of the closure equations are available in ANSYS (2013).

4.2 Lagrangian formulation

The organization of this stage is carried out in the following steps; General Equations, droplet dispersion, droplet evaporation, droplet break, and coupling.

4.2.1 *Force balance equation*

In this formulation, the particle movement is calculated applying force balance using the Newton's second law of motion. Therefore, the trajectory of any discrete particle is predicted by integrating the force balance on the Lagrangian reference frame (Zahari et al., 2018). The force balance is equated to the particle inertial as written in Eq. 4.37.

$$\frac{dv_d}{dt} = F_D\left(u_g - v_d\right) + g\frac{\left(\rho_d - \rho_g\right)}{\rho_d} \qquad 4.37$$

where ρ_d represents the density of the droplet (kg m^{-3}) and F_D stands for the fluid drag force per unit mass given by Eqs. 4.38.

$$F_D = 0.75 \frac{\mu C_D Re}{\rho_d d_d^3} \quad 4.38$$

where C_D is the drag coefficient explained in Liu et al. (1993), and d_d is the particle diameter (m). The Re in Eq. 37 is the relative Reynolds number, which is given by Eq. 4.39.

$$Re = \frac{\rho d_d \left| \vec{v}_d - \vec{v}_g \right|}{\mu_g} \quad 4.39$$

4.2.2 *Droplet dispersion*

The dispersion of droplets caused by turbulence can be calculated using a stochastic model. Specifically, the Discrete Random Walk (DRW) model was employed in this study. This stochastic model is used to compute particle dispersion within a turbulent flow field (Gosman and Loannides, 1983). The droplet velocity is, then, recalculated as a sum of its mean velocity ($\bar{v}$) and a fluctuating contribution (v'), as presented in Eq. 4.40.

$$v_g = \bar{v} + v' \quad 4.40$$

The fluctuating (v') is treated as a random variable and simulated using Gaussian random value with zero mean and a unit variance. Each of the particle eddy is described by a Gaussian distributed random velocity fluctuation v', as shown in Eq. 4.41.

$$v' = \sqrt{2k/3}\ \zeta \quad 4.41$$

Where k and ζ are the turbulent kinetic energy ($m^2\ s^{-2}$) and the normally distributed random number with zero mean and unit variance. The fluctuating component can be computed based on local turbulence characteristics, typically derived from the turbulence kinetic energy and the turbulence dissipation rate.

The dispersion of the respiratory droplets is calculated based on the concept of integral time scale (T), as shown in Eq. 4.42. For smaller tracer particles that dislocate with zero drift velocity with reference of the transporting fluid, the integral time is given as Eq. 4.43, which is the fluid Lagrangian integral time (T_L).

$$T = \int_0^\infty \frac{v'_d(t)v'_d(t-\tau)}{\overline{v'^2}}\, d\tau \tag{4.42}$$

$$T_L = C_L \frac{k}{\varepsilon} \tag{4.43}$$

where τ represents particle relaxation time (s), which is proportional to the dispersion rate, and means; the larger integral time, the larger the turbulence in the flow. The C_L is an empirical constant that ranges from 0.1 to 0.3 depending on the turbulent model, for example 0.15 for the k-ε turbulent models, 0.30 for the RSM. For the k-ω models, $\omega = \varepsilon/k$ in Eq. 4.43.

In DRW model, the interaction of a droplet with discrete stylized fluid phase turbulent eddies given by a Gaussian distribution of random velocity fluctuation (Eq. 4.44) and the characteristics lifetime Eddy (τ_e) (Eq. 4.45) are simulated.

$$\tau_e = 2T_L \tag{4.44}$$

It is considered that the particle interacts with the fluid phase over a minimum Eddy lifetime (4.45)

$$t_{interaction} = f\ (\tau, t_{cross}) \tag{4.45}$$

where $\mathrm{t_{cross}}$ is the time needed for a particle to cross an eddy, and it is expressed by Eq. 4.46.

$$t_{cross} = -\,\tau\, ln\left[1 - \left(\frac{L_e}{\tau|v_g - v_d|}\right)\right] \tag{4.46}$$

where L_e and $|v_g - v_d|$ are the eddy length scale, and the magnitude of the relative velocity, respectively. The time scale of the particle τ_d and the eddy length scale L_e are given by Eqs. 4.47 and 4.48.

$$\tau_d = \frac{1}{18} \frac{\rho_d S d_d^2 C_c}{\mu_d} \tag{4.47}$$

$$L_e = \tau_d \sqrt{\frac{2k}{3}} \tag{4.48}$$

where S and C_c are shape factor and Cunningham slip correction factor (given by Eq. 4.49).

$$C_c = 1 + \frac{2\lambda}{d_d}\left(0.4e^{-\left(\frac{1.1 d_d}{2\lambda}\right)} + 1.257\right) \tag{4.49}$$

where λ is the cough droplets mean free path. When the interaction time (Eq. 4.45) is reached, a new value of instantaneous velocity is calculated by using a new value of ζ in Eq. 4.44.

4.2.3 *Droplet evaporation*

The evaporation of cough droplets is governed by the diffusive flux of droplet vapor in air (Li et al., 2020). In the simulations presented in this study, it was considered that the evaporation initiates when the droplet temperature, T_d, reaches the vaporization temperature, T_v. The evaporation continues until the droplet completely disappears or when it reaches the boiling temperature, T_b, as represented by Eq. 4.50.

$$T_v \leq T_d < T_b \tag{4.50}$$

When the evaporation rate is slow, it can be assumed to be primarily governed by gradient diffusion. In this case, the vapor transitioning from the droplet into the gas phase is

assumed to be driven by the difference in vapor concentration between the droplet surface and the bulk gas. The droplet mass variation is, then, given by Eq. 4.51).

$$\frac{Dm_d}{Dt} = -k_c(C_{v,d} - C_{d,\infty})\, A_d MW_w \tag{4.51}$$

where k_c, $C_{w,d}$ and $C_{w,\infty}$ are, respectively, the mass transfer constant (m s^{-1}), the water concentration at the droplet surface (kmol m^{-3}) and the water concentration in the bulk gas (kmol m^{-3}), respectively. MW_w and A_d are the molecular weight of water (kg $kmol^{-1}$), and surface area of droplet (m^2), respectively. The mass transfer coefficient k_c is calculated from Froessling Equation (Eq. 4.52) through correlating Sherwood (Sh) and Schmidt (Sc).

$$Sh = \frac{k_c d_d}{D_v} = 2 + \frac{3Re_d^{1/2} Sc^{1/3}}{5} \tag{4.52}$$

where D_v and d_p are, respectively, the diffusion coefficient of water vapor in air (m^2 s^{-1}), and the Schmidt number. Eq. 4.52 correlates the data for Reynolds numbers ranging from 2 to 800 and Schmidt numbers from 0.6 to 2.7. The data from Evnochides and Thodos correlate for Reynolds numbers between 1,500 and 12,000 and Schmidt numbers between 0.6 and 1.85. This work was conducted within this range.

At the droplet surface, where the temperature is T_d, the vapor concentration is calculated by assuming that the partial pressure of vapor at the surface is equivalent to the saturated vapor pressure (P_{sat}).

$$C_{v,d} = \frac{P_{sat}}{RT_d} \tag{4.54}$$

where R is the universal gas constant (atm L mol^{-1} K^{-1}).

Additionally, the concentration of the vapor present in the bulk gas is calculated from Eq. 4.55.

$$C_{v,\infty} = \frac{p}{RT_\infty} Y_v \quad 4.55$$

where p (Pa) is the absolute pressure onto the domain, T_∞ (K) is the temperature of the surrounding air and Y_v is the local bulk mole fraction of the water vapor.

For high evaporation rates, the effect of convection during droplet evaporation is relevant, thus modeled based on that principle. Li et al. (2018) and Lu et al. (2020) presented the evaporation rate from the droplet surface into the bulk gas phase (Eq. 4.56).

$$\frac{dm_d}{dt} = k_c A_p \rho_\infty \ln\left(1 + \frac{Y_{v,d} - Y_{v,\infty}}{1 - Y_{v,d}}\right) \quad 4.56$$

where ρ_∞ is the density of bulk gas (air, in this case). $Y_{v,d}$ and $Y_{v,\infty}$ are the respective vapor mass fraction at the droplet surface and vapor mass fraction in the bulk gas (air).

During the process of evaporation, the temperature of the droplet is updated according to the heat balance equation between the droplet and the surrounding (continuous phase) (Eq. 4.57).

$$m_d c_d \frac{dT_d}{dt} + \frac{dm_d}{dt} h_{fg} = hA_d(T_\infty - T_d) \quad 4.57$$

where c_d is the heat capacity of the droplet (J kg^{-1} K^{-1}), h_{fg} is the latent heat (J kg^{-1}), h is the coefficient of heat transfer (W m^2 K^{-1}).

4.2.4 *Droplet Break- Taylor Analogy Breakup (TAB)*

Collisions and breakup of particles occur rampantly in nature. For example, they are seen during the formation of raindrops, activities of nuclear reactors, spray combustion, firefighting, and material spraying processes (Pan et al., 2009). Specifically in this work, when the respiratory particles expelled travel through the air, it is believed that they are subjected to forces that may lead to their breakup. Therefore, to conduct such analysis, the choice for the model will

depend on the flow characteristics, most especially indicated by the Weber number (We). The Weber number is dimensionless number compares the relevance of inertial forces when compared to surface tension as given by (Eq. 4.58) (Campbell, 2015).

$$We = \frac{Drag\ Force}{Cohesion\ Force} = \frac{\rho_d r_d v_d^2}{\sigma} \tag{4.58}$$

where σ is the particle surface tension (N m^{-1}).

When $We = 1$, there are virtually no unbalanced forces acting on the particles (Campbell, 2015). Therefore, it may be assumed that flows are free from surface turbulence. However, We >100 is a value that is considered high (Pan et al., 2009). At such Weber magnitude, the surface turbulence becomes visible and particles can be seen splashing (Campbell, 2015). Among the particle breakup models, the TAB is recommended for low Weber numbers ($We \leq 100$). At the transitional stage ($We \geq 100$), KHRT is recommended, while Wave and SSD are recommended for high Weber. In this work, the TAB model was applied since Weber ranged between minimum and maximum values of 0.378 and 78.39, which is within the recommended range.

The TAB relates the oscillating and distortion of a droplet to the spring-mass system. For instance, it relates the restoring force of a spring to fluid surface tension force, external force to droplet drag force, and damping force to droplet viscosity force. It is assumed that the oscillations attain a critical value which leads to the breakup of parent droplets into several child droplets.

According to O'Rourke and Amsden (1987), the damped forced droplet oscillation is governed by Eq. 4.59.

$$\frac{F_{other}}{m} - \frac{kx}{m} - \frac{d_p}{m}\frac{dx}{dt} = \frac{d^2x}{dt^2} \tag{4.59}$$

where

F_{other}: Other external forces acting on the mass (N).

m: Mass of the particle (kg).

k: Spring constant (N/m).

x: Displacement of the mass from equilibrium (m).

d_p: Damping coefficient (N·s/m).

$\frac{dx}{dt}$: Velocity of the mass (m/s).

$\frac{d^2x}{dt^2}$: Acceleration of the mass (m/s²).

From Taylor's analogy, the coefficients of Eq. 4.59 are given by Eqs. 4.60, 4.61, and 4.62.

$$\frac{F_{other}}{m} = C_F \frac{\rho_g v^2{}_d}{\rho_d r} \tag{4.60}$$

$$\frac{k}{m} = C_k \frac{\sigma}{\rho_d r^3} \tag{4.61}$$

$$\frac{d_p}{m} = C_d \frac{\mu_d}{\rho_d r^2} \tag{4.62}$$

In nondimensional form, $y = x/C_b r$ is substituted in Eq. 4.59 to form Eq. 4.63.

$$\frac{C_F \rho_g v^2{}_{rel}}{C_b \rho_d r} - \frac{C_k \sigma}{\rho_d r^3} y - \frac{C_d \mu_d}{\rho_d r^2} \frac{dy}{dt} = \frac{d^2 y}{dt^2} \tag{4.63}$$

where r_d is the droplet radius. The dimensionless constants C_b, C_F, C_k and C_d are given by 0.5, 0.33, 8 and 5, respectively. Droplet breakup occurs when $y > 1$,

To determine the child droplet size, the energy equations of the parent and child are respectively equated. The energy equation (E_{Parent}) of the parent droplet is given by Eq. 4.64.

$$E_{Parent} = 4\pi r^2 \sigma + k \frac{\pi}{5} \rho_d r^5 \left[\left(\frac{dy}{dt} \right)^2 + \frac{8\sigma}{\rho_d r^3} y^2 \right] \tag{4.64}$$

where $\frac{\pi}{5}$ is geometric factor, $\left(\frac{dy}{dt}\right)^2$ is the square of the rate of change of y with respect to time, representing kinetic energy, $\frac{8\sigma}{\rho_d r^3} y^2$ is the potential energy term related to the surface tension and deformation y, k is the ratio of the total energy in distortion and oscillation to energy in its original form of the order (10/3). And, the energy of the child droplets (E_{child}) is given by Eq. 4.65.

$$E_{child} = 4\pi r^2 \sigma \frac{r}{r_1} + \frac{\pi}{6} \rho_d r^5 \left(\frac{dy}{dt}\right)^2 \quad 4.65$$

Where r/r_1 is Ratio of the radius of the child droplet (r) to the radius of the parent droplet (r_r).

From equating the energy equations (Eqs. 4.64 and 4.65) and considering $y = 1$, the child droplet size can be determined, thus given in Eq. 4.66.

$$r_1 = \frac{r}{\left(1 + \frac{8Ky^2}{20} + \frac{\rho_d r^3 \left(\frac{dy}{dx}\right)^2}{\sigma} \left(\frac{6K-5}{120}\right)\right)} \quad 4.66$$

where $\frac{8Ky^2}{20}$ is related to deformation energy and K is a proportionality constant. The Sauter mean radius r_1 is then applied in the mass conservation equation, and the number of child droplets is calculated.

4.3 Coupling

The interaction between the discrete and the continuous phase is coupling. Normally, it keeps track of mass, momentum and heat lost or gained by particle stream interaction with the continuous phase. This interaction can be modeled using one-way or two-way coupling, each having distinct theoretical underpinnings and computational implementations. Figure 7 shows a droplet moving in a fluid where there is interaction between the phases.

Figure 5- Coupling between the continuous phase and discrete particle

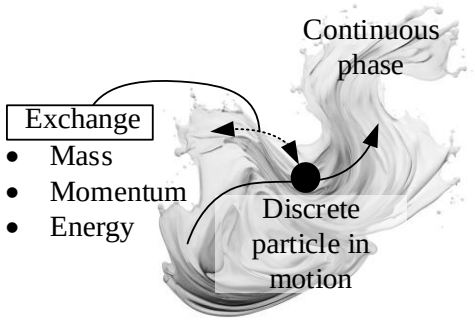

(Self-elaborated)

4.3.1 *One-Way Coupling*

In one-way coupling, the fluid phase affects the dispersed phase (particles or droplets), but there is no feedback from the dispersed phase to the fluid phase. This approach is typically used when the volume fraction or mass loading of the dispersed phase is low enough that its influence on the fluid flow can be neglected.

4.3.2 *Two-way coupling*

In two-way coupling, there is a mutual interaction between the fluid phase and the dispersed phase. This means that the fluid affects the particles, and the particles, in turn, exert forces on the fluid, altering its flow field.

5. SIMULATION

5.1 Work organization

In this thesis, all simulations were carried out using the commercial software ANSYS FLUENT 14.5. The simulations are organized into four (4) distinct parts. The first part involved the application of different turbulence models — namely the Standard k-ε**,** SST k-ω, and Reynolds **Stress** models — to study the evaporation of cough droplets in a closed and quiescent environment, aiming to identify the differences in results provided by each model. The second part assessed the influence of relative humidity on droplets emitted during coughing, also in an indoor and stationary environment. The third part focused on evaluating the feasibility of using graded tetrahedral and hexahedral meshes**,** comparing their performance. Lastly, the fourth part aimed to analyze the behavior of respiratory droplets under the environmental conditions of São Carlos**.** Additionally, three boundary conditions were analyzed: no-slip wall**,** zero-shear stress wall, and pressure outlet**.**

5.2 Processing capacity

The simulations were carried out using a cluster computer of the Chemical Engineering Department of the Federal University of São Carlos (UFSCar). A computing node denoted n002 with 64 core and 576 GB RAM was used. The cluster operates on SUSE Linux with AMD Operon processor 6234 which has a frequency of 2.261 MHz.

5.3 Common to all parts of the studies

To avoid repeating some information in the development of this work, this section was created to register some parameters, boundary conditions and simulation configurations that were common in the whole research. Thus, this part of the research is segmented where the parameters and boundary conditions are firs discussed, next the simulation configuration is set up, and lastly, the run interruption is discussed.

5.3.1 *Parameters and boundary conditions*

The parameters are fluid velocity, temperature and relative humidity. The velocity boundary condition was applied on the inlet to inject the transporting fluid, for all cases**.** The velocity of the transporting fluid which is air blown out during cough (specifically) was established using the UDF (Appendix I), which is a polynomial function. The function $v = f(t)$ was developed in this work to mimic the velocity of a single human cough, and it is presented in Figure 8. The velocity starts at $v = 0\ m/s$ and $t = 0\ s$, marking the beginning of the cough. It then rapidly increases, reaching close to $10\ m/s$ within $0.1\ s$, which is the maximum velocity that the respiratory fluid could attain in this research. Thereafter, the velocity plunges to zero at a total time $t = 0.52\ s$.

Figure 6- Cough velocity profile

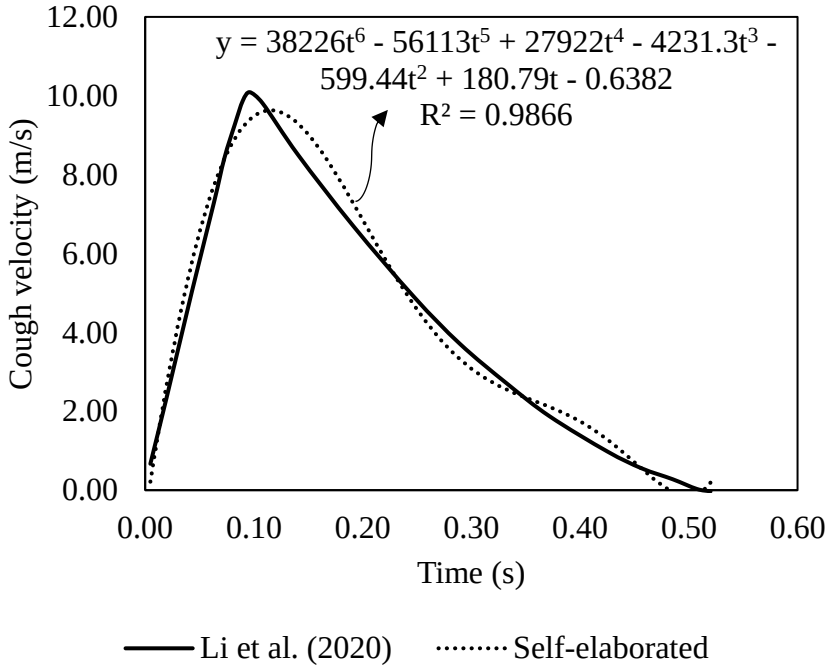

Another parameter common to all the calculations in this research is the human body temperature, which is 310.15 K, provided by the work of Worth and Xi (2008). The respiratory

droplets and the transporting fluid (which is the air released together with the respiratory droplets) were emitted at this temperature.

Lastly, the transporting fluid was released at saturated vapor pressure (100 % relative humidity of air). This condition is similar to the that used by Li et al. (2020) and Redrow et al. (2011).

In the commercial software used in this work, the mass fraction of water vapor was required to set the relative humidity at the inlet region and within the computational domain to carry out the simulations.

Figure 9 shows the relation between the relative humidity and the water mass fraction that was established. Through the patch relative to the cell zone, the value of the mass fraction of water is entered to establish the desired relative humidity.

Figure 7- Relationship between vapor mass fraction of pure water and relative humidity at 293.15 K and 1 atm.

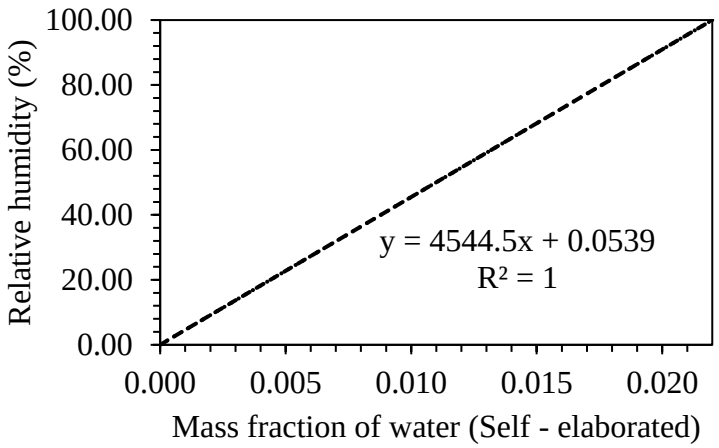

5.3.2 *Simulation configuration*

Here, the pressure-based solver was applied. Transient simulation was carried out (using Second Order Implicit Formulation) - the same time function was successfully applied in Li

et al. (2020) and Li et al. (2018). In the Discrete Particle Model, unsteady particle treatment with fluid flow time-step tracking was applied. In order to track each cough particle, Discrete Random Walk Model with Time Scale Constant of 0.15 was used.

The Semi Implicit Linked Equations (SIMPLE) was applied in pressure-velocity coupling. For Spatial Discretization of the flow gradient, Least Squares Cell Based method was used. Second Order Upwind was used to discretize momentum, Turbulent kinetic energy, Specific dissipation Rate, Discrete Particle Species (water and air) and energy.

5.3.3 *Run interruption*

The numerical tests were performed in two steps. In the first one, simulation was run for $0.52\ s$, which represents the lapse for a single human cough. Thereafter, it was interrupted, and the inlet velocity was set at 0 m/s to carry out the rest of the simulation. This process was done for all studies.

6. PART 1 – TURBULENCE MODEL STUDIES

6.1 Computational domain

Since this specific part of the study was carried out at the inception of this research, there was need to simplify the geometry, and to select numerical parameters with the objective to reduce computational cost. For these reasons, a 2D squared respiratory chamber since according to Steadmam (2006), most buildings are quadrilateral applied to mimic a closed and quiescent space where infectious respiratory diseases could be transmitted. The inlet of the respiratory domain (which represents the mouth of a human in reality in this work) was also a quadrilateral. The geometry of a human mouth is more complex in reality, even though, the choice to apply a quadrilateral was a computational cost reduction strategy. To generate a 2D computational domain presented in Figure 10 was used.

Figure 8- Computational respiratory chamber

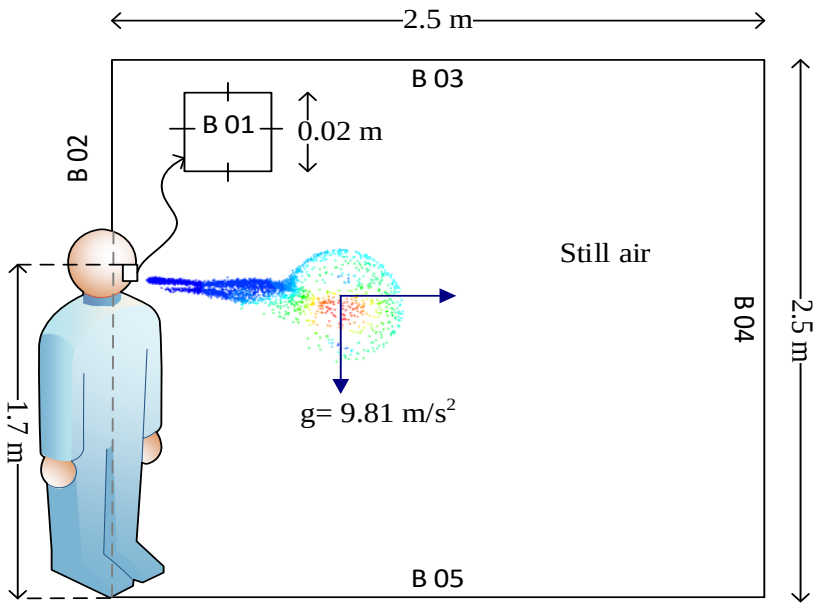

(Self-elaborated)

The height of the cougher (1.7 m) was inspired from the work of Li et al. (2020). The B 01 is the boundary that represents the mouth with an area of $4x10^{-4}$ m^2. The B 02, B 03 and B 05 are walls. Lastly, the B 04 is the domain outlet.

6.2 Numerical mesh

The literature reveals that authors employ diverse mesh types for CFD studies of respiratory events in both indoor and outdoor environments, including tetrahedral, hexahedral, and polyhedral elements. Notably, a wide range of element-to-domain volume ratios has been observed. For example, Redrow et al. (2011) used 500,000 elements to mesh a 17.94 m³ domain (~31,000 elements/m³), while Chillón et al. (2023) utilized 877,000 elements for their 50.4 m³ flow domain (~17,000 elements/m³). D'Alessandro et al. (2021) applied 6 million cells to a 12 m³ flow domain (~500,000 elements/m³), and Oh et al. (2022) used approximately 500,000 elements for a 14.4 m³ flow domain (~35,000 elements/m³). These variations in element-to-domain volume ratios reflect the complexity of each study. For instance, a domain containing a single human is simpler than one with two, and an empty room is less complex than an airplane cabin. Given that these studies were conducted under varying conditions, it is expected that complex domains would necessitate higher mesh densities, regardless of their overall dimensions.

In this study, 3D graded tetrahedral and hexahedral meshes were employed. These meshes were generated using Ansys Meshing 14.5, with a maximum of six levels of refinement. The rate at which cell size increases from one refinement level to the next, such as from level 2 to level 3 (as illustrated in Figure 2).

Figure 9- Mesh with different levels of refinement

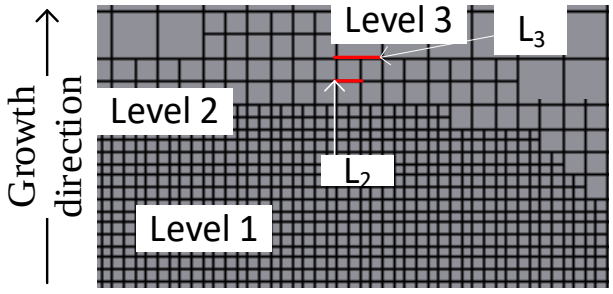

(Self-elaborated)

It is defined by the growth rate (r). For the hexahedral mesh, this relationship is determined by Equation 1. Specifically, a growth rate of 1.5 indicates that the length of a cell at level 3 (L_3) is 1.5 times the length of the corresponding cell at level 2 (L_2).

$$r = 1 + \frac{L_2}{L_3} \tag{6.1}$$

Similarly, the growth rate for the tetrahedral mesh is also calculated using Equation 1. However, the initial cell lengths are determined using Eq. 6.2.

$$L_{level} = \sqrt[3]{\frac{1}{n}\sum_{i=1}^{n}(\Delta V_i)} \tag{6.2}$$

where n is the total number of cells applied in the discretization of the domain, and ΔV_i is the volume of the ith cell (Celik et al., 2008).

The computational domain was discretized using 2D quadrilateral shapes, where about 15600 elements were used (Figure 11).

Figure 10- Structured 2D quadrilateral grid with a single element at the inlet

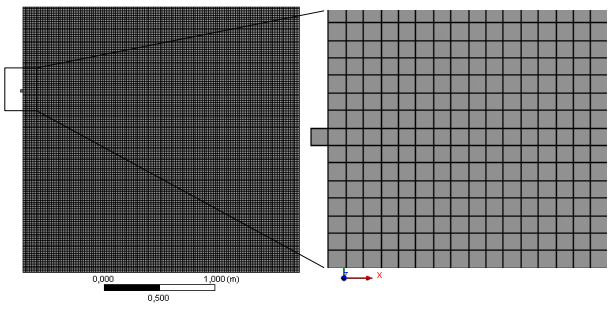

(Self-elaborated)

Specifically, 15625 elements were used to mesh the respiratory chamber, while a single element was used at the inlet region (B 01 Figure 10). The single element was created to inject a single discrete particle per time-step into the respiratory chamber through the cell surface. Details of the mesh generated to carry out the simulation is presented in Table 5.

Table 3- Mesh information

References	Details
Minimum length	0.02 m
Growth rate	1.20
Nodes	15878
Elements	15626
Element quality	0.997

(Self-elaborated)

The minimum cell length established was 0.02 m which was equivalent to the size of the inlet surface. It means that the inlet has a single cell, and in such case a single droplet will be injected at a unit time-step, if simulation is conducted. The growth rate establishes the grading on the cells. The minimum size was established using the inlet size (B 01 Figure 10). On the other hand, the maximum number was attributed through error trial. In the mesh generated, it had no great influence because the CFL number was less than a unit, which means in the mesh generated, Minimum size ≅ Maximum size.

6.3 Initial and boundary conditions (BC)

The attribution of a correct boundary condition is eminent towards qualitative numerical research. This involves considerations related to cost and accuracy. To establish boundary condition to carry out any numerical process, the phases involved determine how to establish such. In a two-phase multiphase flow of droplets and air, BC can be established for each phase.

- *Eulerian phase BC*

In the Commercial software used in this work, the boundary conditions for the Eulerian phase which is a combination of air and vapor are given in Table 4. The table gives the region, type, description and the equations applied in the boundary conditions.

Table 4- Eulerian boundary conditions

Region	Type	Description	Equations
Inlet	Velocity	Specifies the velocity of the fluid entering the domain. The velocity components are defined along with the turbulence parameters.	$v_g = v_{inlet}$ 6.3
	Mass flow	Specifies the mass flow rate of the fluid entering the domain. This is useful when the exact velocity is unknown.	$\dot{m} = \rho v \cdot A$ 6.4
Outlet	Pressure	Specifies the static pressure at the outlet boundary. Fluent adjusts the velocity to satisfy mass conservation.	$P = P_{outlet}$ 6.5
	Outflow	Assumes that the flow exits the domain with a zero-gradient condition for all variables, implying that the quantities are convected out of the domain without any backflow.	$\frac{D\varphi}{Dn} = 0$ 6.6
Wall	No-Slip Wall	Assumes that the fluid velocity relative to the wall is zero.	$v_g = 0$ 6.7
	Slip wall	Allows the fluid to slip along the wall, specifying a tangential velocity.	$v.n = 0$ 6.8
Symmetry Boundary Conditions	-	Used when the domain has symmetry, allowing for reduced computational effort. No flux across the symmetry plane is enforced.	$\frac{D\varphi}{Dn} = 0, v.n = 0$ 6.9

(Adapted from ANSYS, 2013)

Table 5- Lagrangian boundary conditions

General characteristic	Type	Description
Injection	Single	Particles are introduced at a specific location with defined initial velocity, size, temperature, and mass flow rate.
	Surface	Particles are injected from a surface.
Periodic and Symmetry	Periodic	Similar to the Eulerian phase, particles exiting one boundary enter the corresponding opposite boundary.
	Symmetry	Particles are mirrored across the symmetry plane, maintaining their trajectory and properties.
Outflow	Escape	Particles are allowed to leave the computational domain through the outlet boundary.
	Reflect	Particles are reflected back into the domain if they hit the outlet boundary.
	Trap	The particles are trapped when they reach the any boundary that has been characterized thus.

(Adapted from ANSYS, 2013)

- *Lagrangian BC*

The Lagrangian phase typically represents the discrete (particles, droplets, or bubbles) in which the trajectory of each particle is obtained by solving Newton's second law of motion. Here are the common boundary conditions used for the Lagrangian phase (Table 4).

The last BC of the Lagrangian boundary condition is the particle-wall interaction. The types of boundary conditions here characterize what happens to a particle when it touches the boundary. Figure 3 presents the particle-wall boundary conditions.

In the “reflect” boundary condition, the respiratory droplets bounce back to the domain when they hit the boundary. This condition is also applied when one desires to retain the droplets after they touch the boundary. For this kind of boundary, the momentum change is defined by the coefficient of restitution $e_n$which relates the velocities ($v_{1,n}$and $v_{2,n}$) of the particle before and after collision. In the case of “escape” boundary condition, the particles evacuate when they touch the boundary. Lastly, the “trap” boundary condition makes volatile particles to evaporate or terminate when they touch the boundary.

Figure 11- Disperse phase boundary conditions

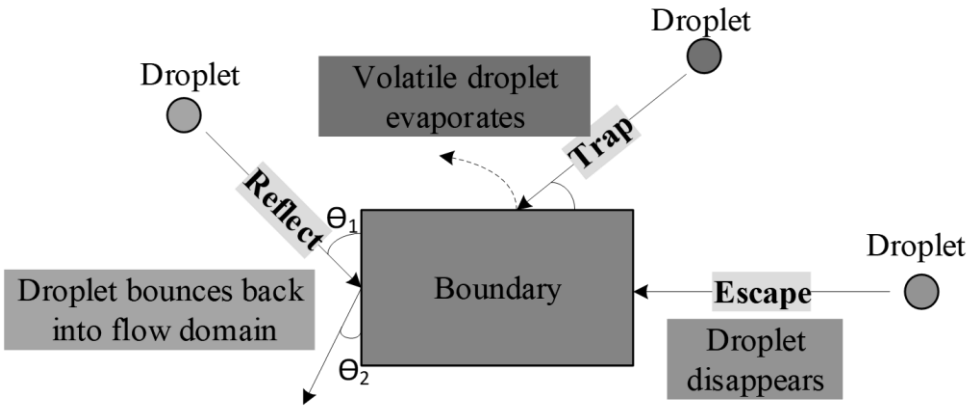

(self-elaborated)

The Eulerian-Lagrangian boundary condition can be specified based on the composition of the flow; continuous phase and discrete phase as presented in Table 6.

Table 6- Boundary condition of the Euler-Lagrangian model

	Eulerian Phase	**Lagrangian Phase**	**Chamber boundary Region**
Inlet	Velocity inlet	Surface velocity injection	B 01
Outlet	Pressure outlet	Escape	B 04
Wall	No-slip	Reflect	B 02 and B 03
		Trap	B 05

Self-elaborated

The initial value of the velocity applied to inject the transporting fluid is given by the velocity function given in Fig 8 of Section 5.4.

6.4 Other important properties

The respiratory droplets used at this stage of the research are 1 μm, 10 μm, 50 μm and 100 μm. The choice was motivated by the work of Li et al. (2020), where the authors analyzed extreme (In each case of the simulation, a single droplet was released into the respiratory chamber in a single time step. Other complementary conditions can be found in Section 5.3.

6.5 Simulation configuration

The configurations in 5.3.2 were applied. In addition, since particles that are relatively small evaporate faster, there was smaller time-steps were applied to capture their evolution. Therefore, specifically in this initial stage, 10^{-5} s was used to simulate the evaporation of particles ≤ 10 μm, while 10^{-3} s time-step was used for 10 μm <particles≤ 100μm particles. This strategy was adopted to reduce computational cost.

6.6 Part 1 Results

The simulations carried out in this study lasted 10 to 15 days on an average depending on the complexity of the model. Standard k-ε was the cheapest in terms of computational cost followed by the SST k-ω, while RSM was the most expensive.

6.6.1 Mesh independence test

To conduct the turbulence model test in this work, firstly, a mesh independence test was carried out. Three sizes (S1, S2 and S3) were selected representing fine, medium and coarser meshes, respectively. Details of the selected meshes are presented in Table 7.

Droplet evaporation was the parameter applied in the mesh independence test. The diameter variation of a single droplet caused by evaporation was calculated. Here, a 1 μm droplet was released into the computational domain and its evaporation was observed over time, under 80% humidity (Figure 12). Once the single droplet is released, its size reduces due to evaporation until it disappears, marking the end of the droplet tracing within the computational domain. It can be observed that the change of the droplet diameter calculated by S1, S2 and S3 were similar. The results indicate that the solution has converged, hence the mesh is independent.

Table 7- Mesh applied in this study with different level of refinement

Name	Element size (m)	Nodes	Elements	Quality	Standard deviation of quality
S1	0.005	251021	250016	0.999	±3.022E-06
S2	0.010	63007	62504	0.999	±1.656E-06
S3	0.020	15878	15626	0.999	±3.074E-07

(self-elaborated)

Figure 12- Mesh independence test using 3 levels of mesh refinement

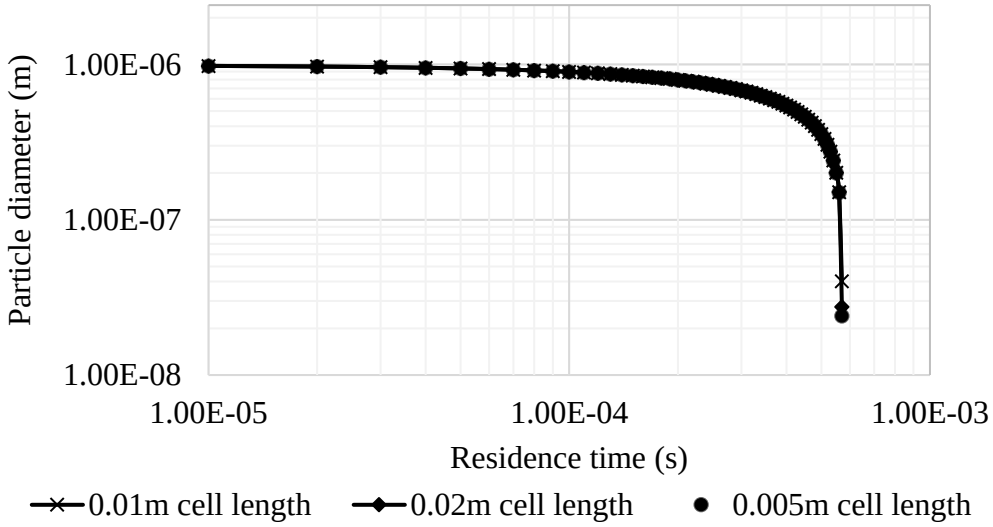

(Self-elaborated)

Similar grid test results were also observed in Sen (2021). However, the authors used unstructured tetrahedral cells to form the computational grid. Similarly, D'Alessandro et al. (2021)

carried out a mesh test measuring the streamwise velocity of cough cloud for continuous phase, using fully structured mesh (with 2.856 x10^6, 5.830 x10^6 and 9.854x10^6 elements, respectively). The authors also presented results similar to those in Figure 12. Therefore, the intermediary mesh (0.02 m cell length) was selected to carry out the rest of the simulation. This choice was motivated by the computational capacity available and the simplicity of the case-study model.

6.6.2 Droplet independence test

Normal human cough is turbulent and transient, and the particles are released into the surroundings randomly. For these reasons, consecutive multiple coughs from a single person can present different particle behaviors. To ascertain how the evaporation rate varies during each cough, a droplet evaporation independence test was carried out. A 1 μm particle was released five times (in different simulations) into the computational domain and its evaporation was observed. The result is presented in Figure 13.

Figure 13- Droplet evaporation convergence test

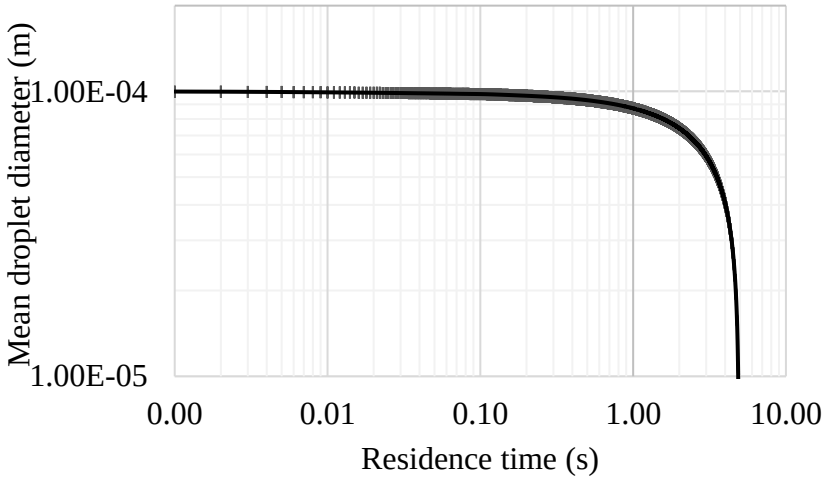

(Self-elaborated)

Since the particle tracking was conducted with DRW which is a probabilistic model, the droplet evaporation was expected to vary for the five trials. However, it can be observed that the

evaporation rate was similar in all cases; the standard deviation was relatively low. That is to say, simulating with a single particle will not just lessen the computational cost, but will also produce satisfactory results.

6.6.3 Validation

To validate the simulation, a few tests were carried out to compare the droplet evaporation presented by Li et al. (2020) under the conditions presented in Table 8. The table comprises details of the computational domain, droplet particle, and other conditions applied in this part of the research.

Table 8- Simulation conditions used by Li et al. (2020)

Nomenclature	Magnitude/characteristics
domain dimension	10.1 m length, 7.12 m width and 5.4 m height
Number of cough droplet particles	4897
Cloud mass	9.37×10^{-6} kg
Flow rate	1.80×10^{-5} kg/s
Species	Air (oxygen, nitrogen, and water vapor)
Mouth areas of cougher	4 cm^2
Cough temperature	310.15 K
Room Temperature	293.15 K
Cougher's height	1.70 m
Grid	Unstructured polyhedral
Density	998.2 kg/m^3
Specific heat	4182 J/kg.K
Latent heat	2263073 J/kg
Vaporization temperature	284 K
Volatile component fraction	100%

(Adapted from Li et al., 2020)

6.6.4 Droplet evaporation

Figure 14 shows the comparison of the droplet evaporation calculated in this work with the work of Li et al. (2020). It was conducted under 0% and 80% relative humidity conditions using different droplet diameters.

In Fig 14, the droplet evaporation in this work was generally faster than the evaporation rate calculated by Li et al. (2020). A large difference in evaporation time was observed in 1 µm and 100 µm. For instance, a time difference of 0.02 s was registered. Additionally, at the release of 100 µm droplet into the computational domain under 80 % humidity, Li et al. (2020) presented a total evaporation time of about 0.06 s faster. These estimations were made when the particles approached total evaporation. Nevertheless, the results were similar. Smaller droplets evaporated faster than the larger ones at the same relative humidity conditions.

Figure 14- Respiratory droplet evaporation of different particle sizes under 80% relative humidity

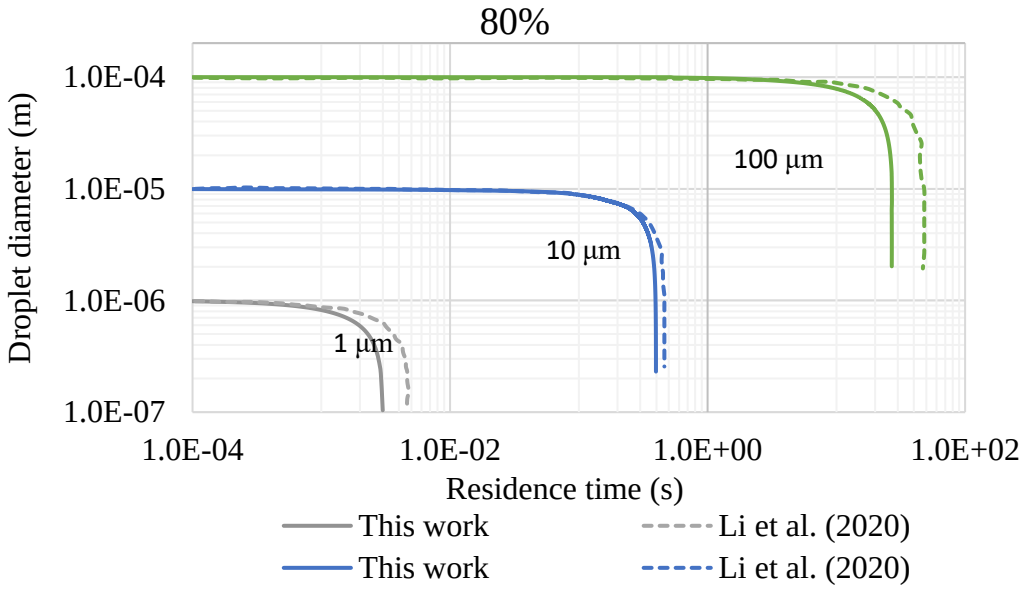

(Self-elaborated)

The slight difference noticed in the results might have arisen from the numerical models or mesh differences.

6.6.5 Turbulence model comparison

➢ *Diameter variation*

The first comparison of the turbulent models was based on droplet diameter variation. The evaporation of 1 µm and 100 µm at a humidity of 0%. The results are presented in Fig 15. In (a) and (b), the turbulence models calculated similar results. The curve of the droplet diameter calculated by the turbulent models forms an overlay that is difficult to distinguish.

It can be noticed that the $(SST)k-\omega$, Standard $k-\varepsilon$ and Reynolds Stress) applied to calculate the evolution of a single droplet presented similar results.

Figure 15- Evaporation of cough droplet particle using cough velocity of 10 m/s (SST) k-ω, k-ε and Reynolds Stress (RSM) turbulence models (a) 1 µm and (b) 100 µm

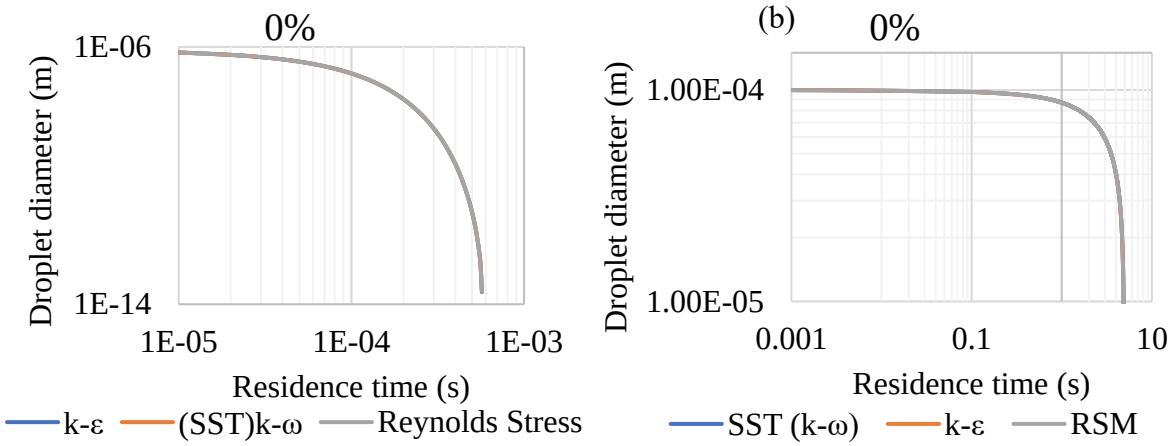

(Self-elaborated)

The similarities in the results observed in Figure 15 might have resulted from the simplicity of the case study. The flow was simple and had no separation, adverse pressure gradient, and anisotropy, therefore, it is possible that all the turbulent models calculate similar droplet behavior in an indoor and still environment.

➢ *Velocity variation*

At this stage, three constant cough velocities (10 m/s, 14 m/s, and 20 m/s) were respectively used to inject a 100 μm particle into the flow domain (Fig 8). The values were inspired by Han et al. (2013), where values from 10 m/s to 20 m/s were applied. All the simulations were carried out at 0% humidity, and part of the results are presented in Table 9.

Table 9- Time taken by 100 μm droplet to evaporate at different injection velocities and 0% humidity

Velocity (m/s)	Evaporation time (s)		
	k-ε	(SST) k-ω	RSM
10	4.949	5.371	4.914
14	4.904	4.919	5.087
20	4.906	4.918	4.918

(Self-elaborated)

In general, an increase in cough velocity seldom affected the droplet evaporation time as the results in Table 9 present. However, (SST) k-ω droplet evaporation was affected by increase in velocity. However, it was expected that increase in velocity of cough may increase evaporation due to increased contact of the droplets with the surrounding air.

Even though the results did not represent a significant difference, the (SST) k-ω is recommended because it offers a good balance between accuracy and computational cost, particularly effective near walls and in boundary layers, making it suitable for scenarios involving surface interactions.

➢ *Application*

In this section, the turbulence model (SST) k-ε was selected and applied. Here, the evaporation of three droplet sizes (1 μm, 10 μm and 100 μm) were observed under two humidity conditions (0% and 80%), as presented in Figure 16.

Figure 16- Single drop evaporation under various humidity and droplet sizes

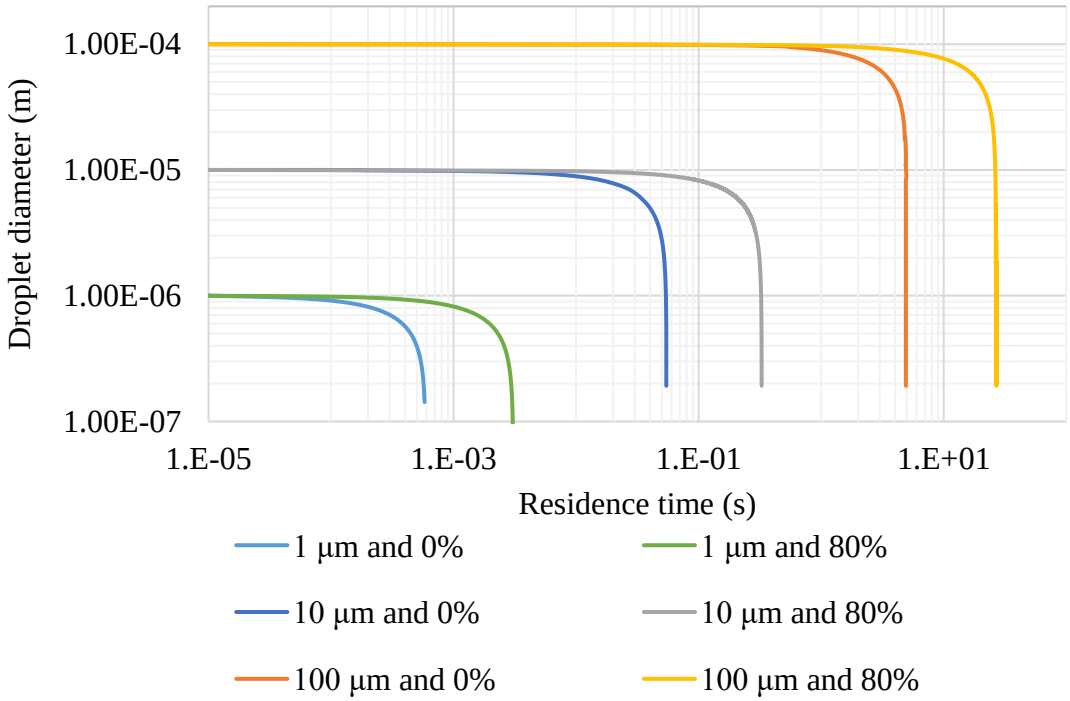

(Self-elaborated)

The relative humidity of the air significantly influences the evaporation of respiratory droplets. For example, at 4.9 seconds into the flow, the size of droplets initially released at 100 µm shows a percentage difference of over 100% when comparing 0% and 80% relative humidity conditions.

Similar to other studies like Morawska (2006), Redrow (2011), Dbouk and Drikakis (2020), Li et al (2020), Li et al (2018) and Liu et al (2019), droplet evaporation was faster for smaller droplets because of increased surface area per unit volume, which favors contact with dry air.

7. PART 2 – MESH STUDIES

This section aims to compare the graded hexahedral and tetrahedral meshes. Thus, the droplet diameter reduction caused by the evaporation of respiratory droplets, the position of the droplet cloud calculated by the meshes at different relative humidity conditions, and the droplet evaporation time were compared. In addition, a Grid Convergence Index (GCI) test is carried out to assess the viability of the mesh density used in the study. Through the GCI study, a mesh was strategically selected for further computations.

7.1 Computational domain

A domain of 2.5 m by 1 m by 2.5 m was built to carry out the study (Figure 17).

Figure 17- Geometry of the respiratory chamber with dimensions and indications of boundaries used to establish boundary conditions

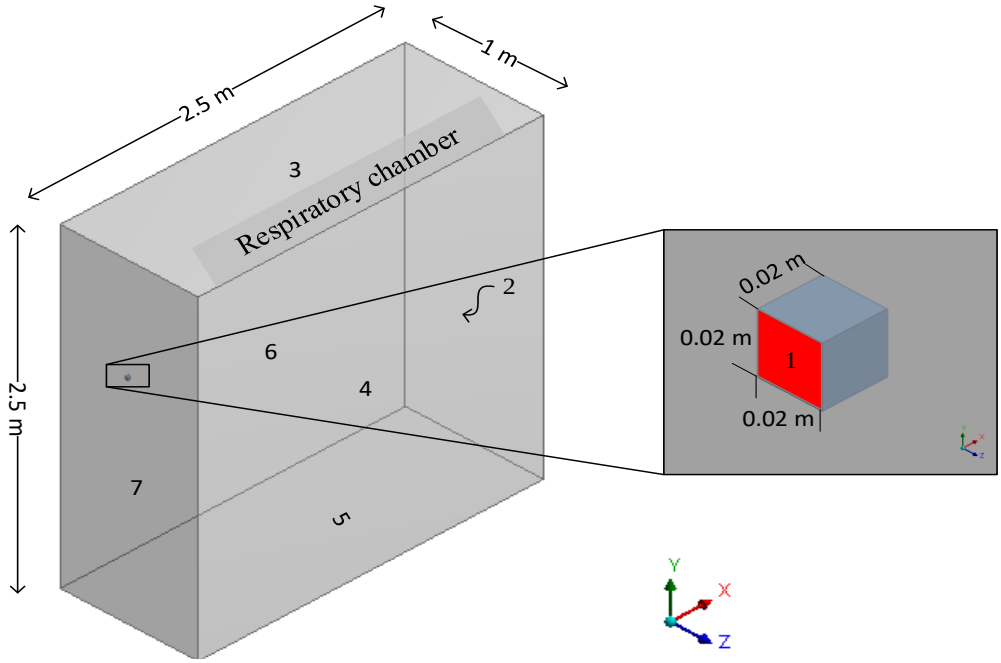

(Self-elaborated)

The velocity inlet (1), which represents the mouth of a human, protruded to a length of 0.02 m from wall 7, and with an area of 4.0 x 10^{-4} m^2.

7.2 Numerical mesh

Two meshes built with tetrahedral and hexahedral elements were studied in this part of the research. The inlets (1 of Figure 17) of both meshes were discretized with 400 cells. That means, 400 particles were expected to be released at every time step. The number of particles used in this part of the studies is different from previous studies because it was conducted in 3D, and multiple particles were expected to represent a cough situation better than a single particle. The distribution of the mesh cells was controlled by growth rates ranging between 1.04 and 1.30. Additionally, the minimum and maximum cell lengths that were applied ranged between 2.0 x10^{-3} m and 0.128 m.

To carry out the mesh studies, four levels of mesh refinements were applied: g_1, g_2, g_3, and g_4. The respective meshes are presented in ascending order of cell density. More details of the respective meshes are presented in Table 10.

Table 10- Details of tetrahedral and hexahedral meshes with respective number of elements growth rate and quality

Grid	g_1	g_2	g_3	g_4
Tetrahedral mesh				
Number of elements	40,000	150,000	600,000	2,400,000
Growth rate	1.300	1.128	1.071	1.041
Average Skewness	0.208	0.215	0.213	0.212
Standard deviation	0.152	0.128	0.118	0.114
Hexahedral mesh				
Number of elements	40,000	150,000	600,000	2,400,000
Growth rate	1.150	1.068	1.035	1.019
Average Skewness	0.013	0.005	0.002	0.001
Standard deviation	0.066	0.044	0.026	0.015

Figure 18- Projections of the isomeric, side, and cutout views of a tetrahedral mesh with (a) g1- 40 thousand elements (b) g2- 150 thousand elements (c) g3- 600 thousand elements, and (d) g4- 2.4 million elements

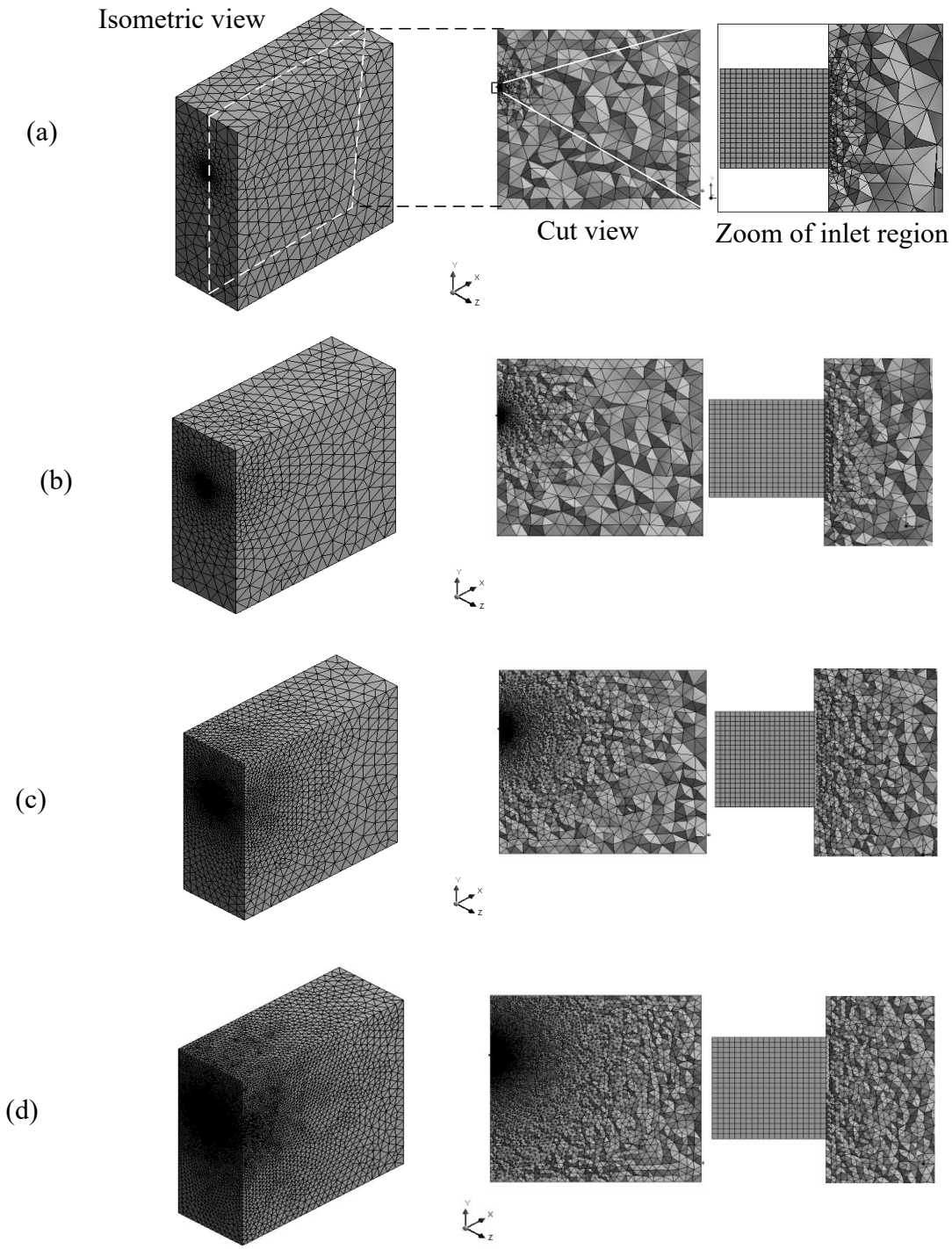

(Self-elaborated)

Figure 19- Projections of the isometric, side, and cutout views of a hexahedral mesh with (a) g1- 40 thousand elements (b) g2- 150 thousand elements (c) g3- 600 thousand elements, and (d) g4- 2.4 million elements

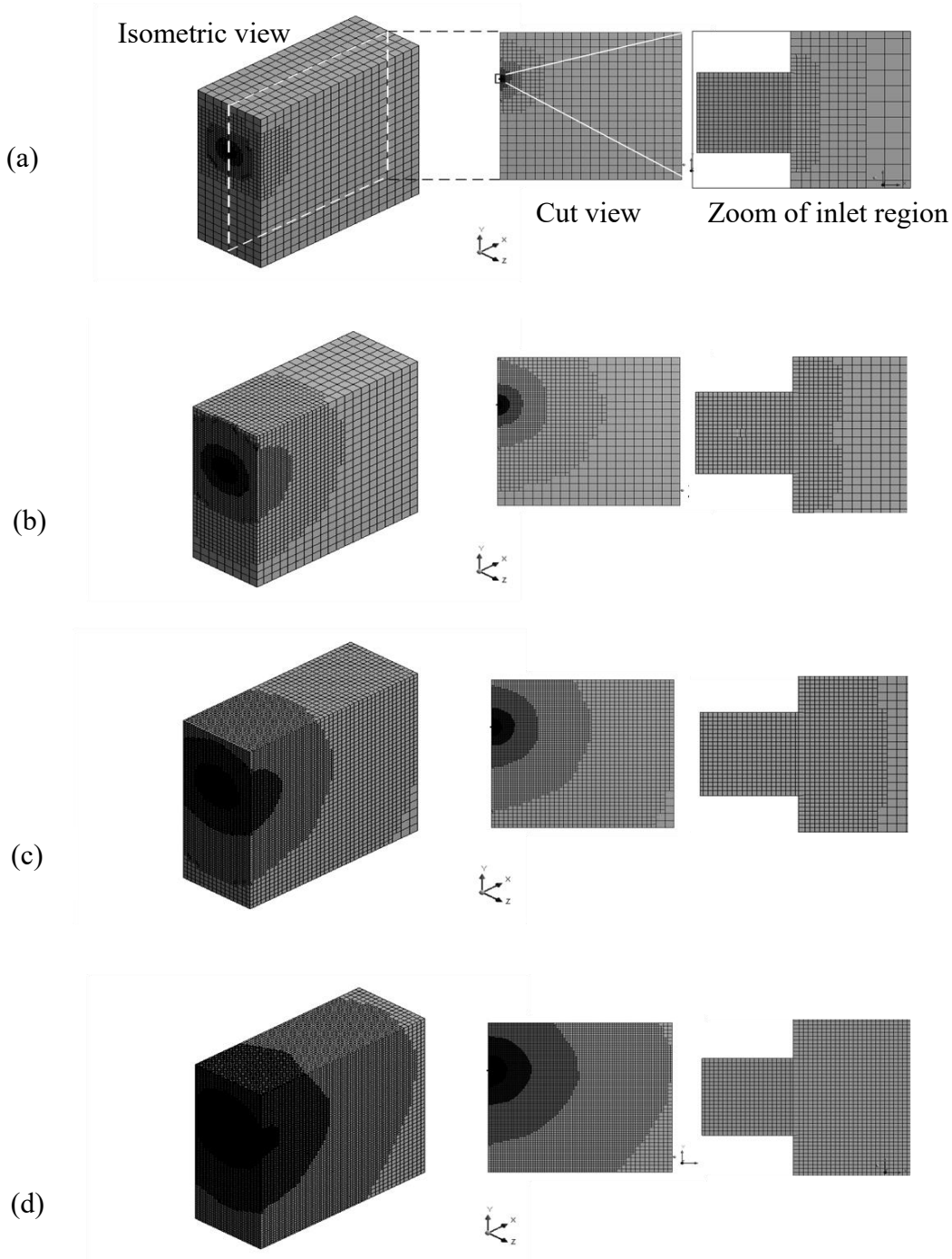

(Self-elaborated)

The meshes g_2, g_3 and g_4 were generated with a relation where the grid spacing in each direction increased by 2 between two successive meshes. For instance, a mesh generated with 387 cells in each direction has 149769 elements, the next mesh will have 774 cells in each direction with a total number of 599076 elements. As for the g_1 mesh, half of the number of elements was used. The mesh distribution applied in g_2, g_3 and g_4 was prior to the Grid Convergence Index that is applied in Section 7.4.

To ensure an equal number of elements in the computational domain for both graded tetrahedral and hexahedral meshes, the growth rate of the hexahedral elements was set to approximately twice that of the tetrahedral elements. Figures 18 and 19 represent all mesh projections. The growth rate was varied to establish the exact number of elements the respects the grid spacing established for these studies.

The g1 mesh has about three zones with different element size. However, g4 has about six zones due to mesh grading using configurations that generate a high-density mesh.

7.3 Initial and boundary conditions (BC)

The Eulerian and Lagrangian boundary conditions used in this part of the research is presented in Table 11.

Table 11- Boundary condition for mesh independence test and result calculations

	Eulerian Phase	**Lagrangian Phase**	**Chamber boundary Region**
Inlet	Velocity inlet	Surface velocity injection	1
Outlet	Pressure outlet	Escape	2
Wall	No-slip	Reflect	5
		Trap	2, 3, 4, 6 and 7

(Self-elaborated)

The “reflect” was attributed to the floor of the domain to retain droplets whenever hit the floor, that way, a concise visual representation can be made. Two sets of simulations were conducted in this part of the study. The first set involved the Grid Convergence Index (GCI) test developed by Roache (1994), while the second set was performed to compare the results with Li et al. (2020) and Redrow et al. (2011).

Therefore, the GCI was conducted with ambient temperature kept at 294.15 K; which is the average annual temperature of the city of São Carlos, in São Paulo State of Brazil (Climate-Data, 2023) was applied. Additionally, relative humidity and droplet diameter of 50% and 50 μm which were adopted specifically for this test, but do not represent any condition of the city. As for the transporting fluid (which represents a human cough in reality), it was released at a velocity guided by the User Defined Function (UDF in Appendix I).

As for the rest of the simulation, the ambient temperature of 293.15 was applied (from Li et al. 2020). Two relative humidity conditions were used; 0% and 80%. The velocity of the transporting fluid was guided by the UDF in Appendix I. In the discrete phase, three droplet sizes; 1 μm, 10 μm and 100 μm were applied.

In both GCI test and the rest of the case study, 400 particles of 50 μm, and humid air (with a relative humidity of 100%) were released into the respiratory chamber in a single time step. The respiratory droplets were released at a constant velocity of 10 m/s using face normal direction. The droplets were at a temperature of 310.15 K.

7.4 Mesh independence test

In this section, the Grid Convergence Index is studied. It is a method used to estimate the numerical uncertainty in computational fluid dynamics (CFD) and other computational simulations. The Grid Convergence Index (GCI) was developed by Patrick J. Roache in the early 1990s where formal and standardized method for quantifying the numerical uncertainty associated with grid convergence in computational fluid dynamics (CFD) and other computational simulations can be analyzed. It quantifies how the results of a simulation converge as the computational grid is

refined (i.e., as the grid becomes finer with more cells or elements). In this study, the GCI is calculated by the following steps; establishing the parameter of evaluation, the respective mesh types and refinements, calculating the Richardson Extrapolation and lastly, calculating the GCI.

Table 12 presents the values for the droplet diameter (d1, d2, d3, and d4, corresponding to meshes g1, g2, g3, and g4, respectively), which are the solution variables used in the mesh independent test, as well as the corresponding times at which each value was obtained for the different meshes. In the GCI evaluation, g1 was excluded because a three-level mesh convergence order was applied. Therefore, g2, g3, and g4, representing the coarse, medium, and fine meshes, were further analyzed.

Table 12- Respiratory particle diameter at a specific time for different mesh structures and refinement levels

Diameter (m)			**d_1**	**d_2**	**d_3**	**d_4**
Nomenclature			g_1	g_2	g_3	g_4
	Grid index	**time (s)**	40,000	150,000	600,000	2.4 million
Tetrahedral mesh	1	0.05	$4.84x10^{-5}$	$4.84x10^{-5}$	$4.84x10^{-5}$	$4.84x10^{-5}$
	2	0.10	$4.72x10^{-5}$	$4.72x10^{-5}$	$4.72x10^{-5}$	$4.71x10^{-5}$
	3	0.50	$3.73x10^{-5}$	$3.69x10^{-5}$	$3.69x10^{-5}$	$3.69x10^{-5}$
	4	1.00	$1.89x10^{-5}$	$1.78x10^{-5}$	$1.79x10^{-5}$	$1.78x10^{-5}$
Hexahedral mesh	1	0.10	$4.72x10^{-5}$	$4.91x10^{-5}$	$4.91\ x10^{-5}$	$4.90\ x10^{-5}$
	2	2.00	-	$3.77x10^{-5}$	$3.77\ x10^{-5}$	$3.78\ x10^{-5}$
	3	3.00	-	$3.04x10^{-5}$	$3.04\ x10^{-5}$	$3.04\ x10^{-5}$
	4	4.00	-	$2.07x10^{-5}$	$2.07\ x10^{-5}$	$2.07\ x10^{-5}$

(Self-elaborated)

The behavior of the solution error, termed The Order of Convergence, is determined by the difference between the discrete solution and the exact solution, and it is calculated using Eq. 7.1 (Roache, 1998).

$$p = \ln\left(\frac{d_3 - d_2}{d_2 - d_1}\right) / \ln(p_t) \qquad 7.1$$

where p_t is the theoretical order of convergence, which was set to 2. The values of p for the specified time intervals are presented in Tables 13 and 14 for tetrahedral and hexahedral meshes, respectively.

Table 13- Order of convergence for tetrahedral mesh at four different time intervals

Time (s)	p
0.05	0.6512
0.10	5.1132
0.50	0.2174
1.00	0.5170

(Self-elaborated)

Table 14- Order of convergence for hexahedral mesh at four different time intervals

Time (s)	p
0.10	0.4661
2.00	3.1726
3.00	2.5768
4.00	2.4469

(Self-elaborated)

As can be seen, the order of convergence calculated from the particle evolution using a tetrahedral mesh differs from the theoretical order of convergence $p_t = 2$. Conversely, most of the values calculated for the hexahedral meshes are closer to p_t. The discrepancies observed in the evolution of respiratory droplets calculated on the tetrahedral mesh could have resulted from the mesh itself or the numerical models used to discretize the flow equations. Additionally, a portion of the deviation could have come from the mean droplet particle size measured over time, since the diameter value used for the evaluation represents an average distribution of 400 respiratory droplets. The theoretical order of convergence can be applied to obtain the true droplet size through Richardson extrapolation. This is calculated using the two finest grids at zero grid spacing, as given in Equation 34 Eq. 7.2.

$$\mathrm{f_{h=0}} = \mathrm{d_2} + \frac{\mathrm{d_2} - \mathrm{d_3}}{\mathrm{r^p} - 1} \tag{7.2}$$

where r is the grid refinement ratio ($r = 2$) which corresponds to the order of the discretization model applied in this study. The extrapolations for tetrahedral and hexahedral meshes using d_2 and d_3 are plotted in Figure 20, where the respective values are the droplet diameters at the respective flow times.

Figure 20- Richardson Extrapolation for (a) Tetrahedral mesh (b) Hexahedral mesh (c) Tetrahedral and Hexahedral mesh at 0.1 s

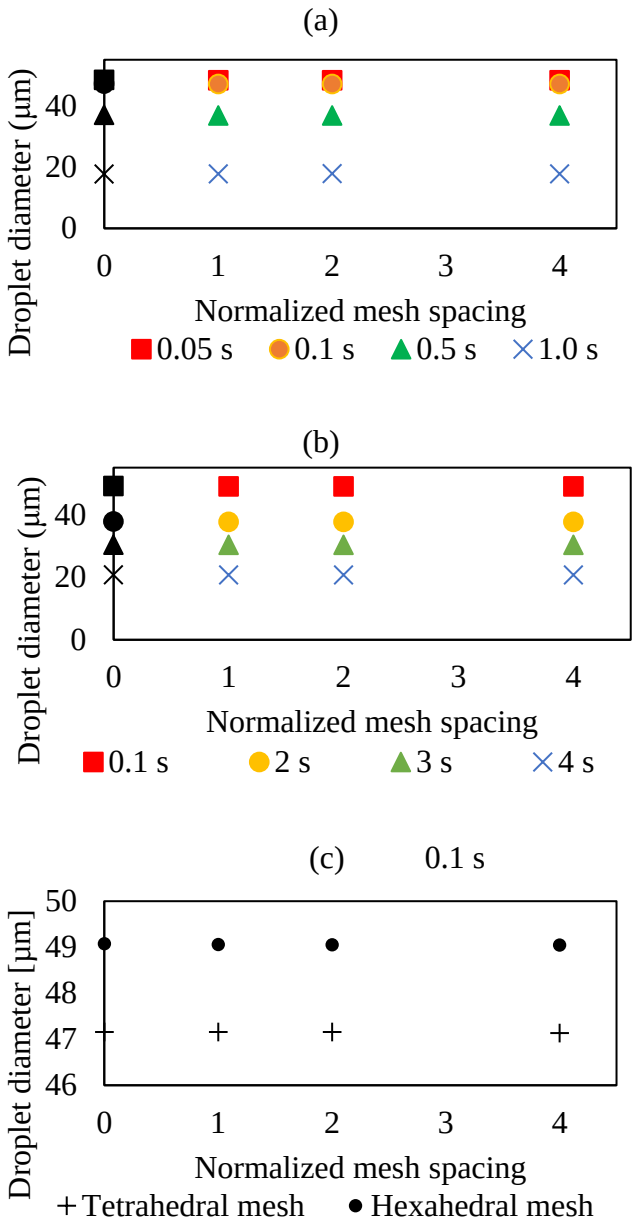

(Self-elaborated)

Despite the observed discrepancies in the order of convergence, particularly with the tetrahedral mesh, the extrapolated values in Figures 20(a) and 20(b) are similar to the respiratory

droplet diameters calculated by both meshes. Figure 20(c) shows a relatively small discrepancy of 3.9% between the diameters calculated by the tetrahedral and hexahedral meshes at 0.1 s.

With all the subsequent information, the GCI can be computed using a safety factor of $F_s = 1.25$, which is a standard value used when three grids are used. Thus, the GCI for the medium and fine refinements levels can be calculated using Eq. 7.3 and the results for this specific case are presented in Table 15.

$$GCI = \frac{F_s|\varepsilon|}{r^p - 1} \tag{7.3}$$

Table 15- GCI for tetrahedral mesh at using different time intervals

Time (s)	$GCI_{g2 \text{ and } g3}$ (%)	$GCI_{g3 \text{ and } g4}$ (%)
Tetrahedral mesh		
0.05	0.0046	0.0072
0.10	0.0001	0.0020
0.50	0.5546	0.4767
1.00	-	-
Hexahedral mesh		
0.1s	0.0397	0.0548
2.0s	0.0004	0.0040
3.0s	0.0017	0.0100
4.0s	0.0047	0.0256

(Self-elaborated)

where ε is the relative error, which could be defined depending on the mesh level. For instance, for the first and second levels, the relation is given by Eq. 7.4.

$$\varepsilon = \frac{d_2 - d_1}{d_1} \tag{7.4}$$

At this stage, it is possible to check if the solutions are in the asymptotic range of convergence through the mesh range ratio given by Eq. 7.5. The values of the ratio are presented in Table 16.

A ratio of close to 1 indicates that the solution is within asymptotic range. Therefore, it can be concluded that the results obtained for the behavior of the respiratory droplet in the

respiratory chamber under the specified conditions are within the convergence range. Consequently, all meshes (g2, g3, and g4) can be used in CFD studies of coughs in closed spaces. Since all the meshes applied in the GCI are apt for application to carry out this study, mesh g_2 was selected based on computational cost.

$$\text{Ratio} = \frac{\text{GCI}_{d_3,d_4}}{r^p \text{GCI}_{d_2,d_3}} \quad 7.5$$

Table 16- Asymptotic range of convergence check

Tetrahedral mesh		Hexahedral mesh	
Time (s)	Ratio	Time (s)	Ratio
0.05	1.00002	0.10	1.00012
0.10	1.00002	2.00	0.99997
0.50	0.99938	3.00	0.99993
1.00	-	4.00	0.99983

(Self-elaborated)

During the generation of the tetrahedral element mesh, a small percentage of hexahedral and pyramidal elements were observed. Similarly, in the hexahedral element mesh, traces of tetrahedral and pyramidal elements were found. However, in both cases, they were present in insignificant quantities. It is important to note that the presence of other cell geometries within a mesh in negligible quantities is normal. For the selected mesh, the quality was within the recommended range (skewness < 0.95).

7.5 Comparison with literature results

Due to the scarcity of detailed experimental data on cough droplet evaporation in the literature, consolidated results from the discrete phase model equation are commonly used as benchmarks (Sedighi et al., 2023). Studies by Redrow et al. (2011), Wei and Li (2015), Li et al. (2018), and Li et al. (2020) are frequently referenced in the literature for CFD simulation validation. In the present work, simulated results are compared with data from Redrow et al. (2011) and Li et al. (2020). The details of the conditions applied by these authors and in this study are presented in Table 8. Comparisons between the literature results and the graded tetrahedral and hexahedral mesh

results are presented in Figures 21 and 22. To reduce computational cost, this study employed a smaller number of particles, while still achieving results consistent with the literature. Moreover, preliminary tests with a larger number of particles yielded similar findings. Furthermore, the use of a one-way coupling approach, which neglects particle-particle and particle-fluid interactions, explains this consistency.

Table 17. Parameters and conditions applied by the authors used to compare the results of this work

Parameter	Redrow et al. (2011)	Li et al. (2020)	This work
Droplet diameter	1— 10 and 100 (µm)	1, 10 and 100 (µm)	1, 10 and 100 (µm)
Breath temperature	310.15 K	310.15 K	310.15 K
Room temperature	294.15 K	293.15 K	294.15 K
Relative humidity	0%	0%	0%
Number of particles	50,000	4,897	400
Number of cells	554,028	3,900,000	150,000
Cell geometry	Tetrahedral	Polyhedral	Tetrahedral/Hexahedral

Figure 21- Evolution of droplet diameter with time, under 0% relative humidity, in a quiescent space: comparison with the data from Redrow et al. (2011)

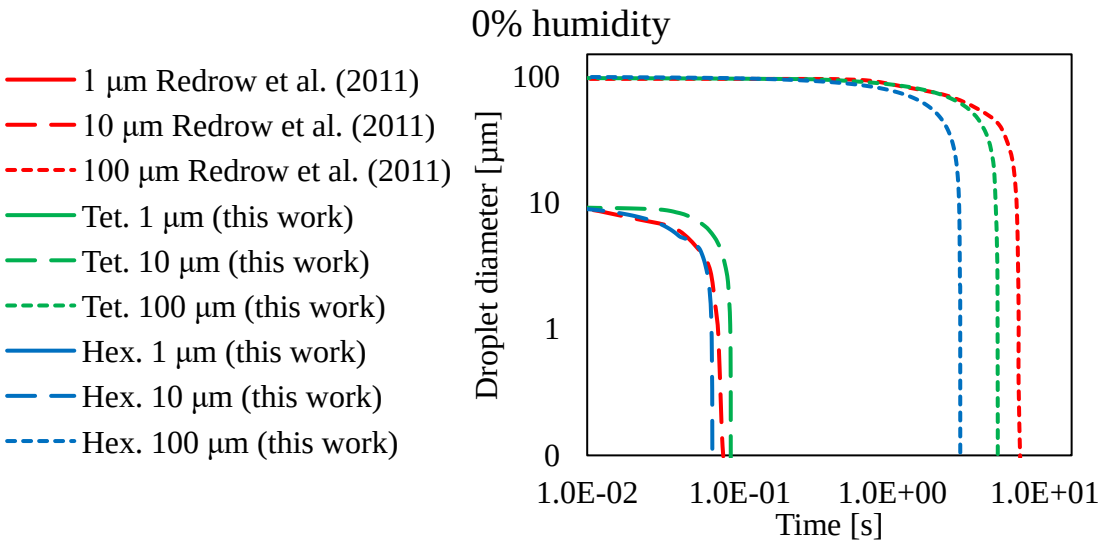

(Self-elaborated)

Figure 22- Evolution of droplet diameter with time, under 0% relative humidity, in a quiescent space: comparison with the data from Li et al. (2020)

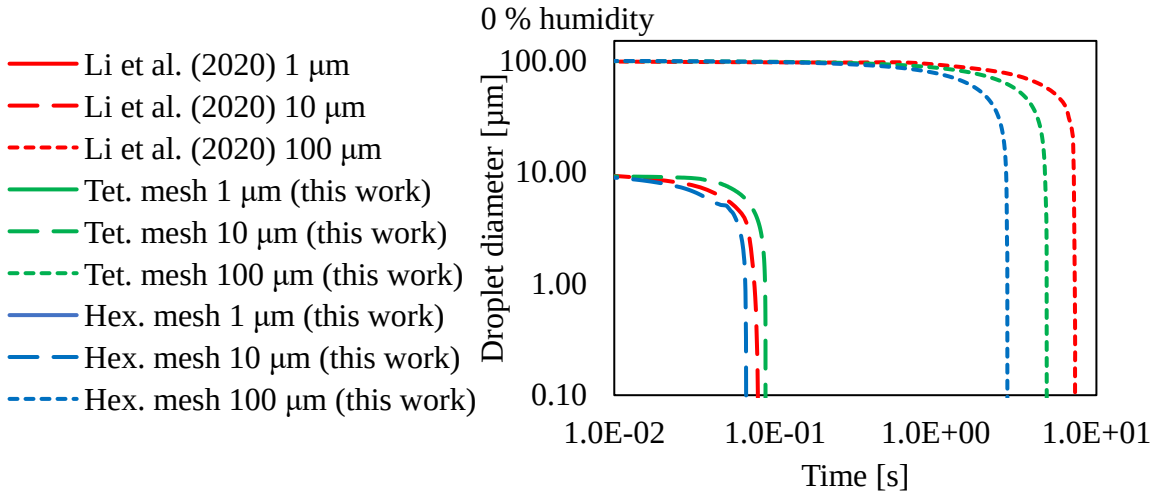

(Self-elaborated)

When comparing the two graded meshes, the tetrahedral mesh calculated a higher evaporation rate than the hexahedral mesh under the same numerical conditions. It was also noted that the simulation of larger droplets resulted in higher differences between the evaporation time calculated by the graded tetrahedral and hexahedral meshes. This difference is practically negligible for 1 and 10 µm droplets. Although, in all cases, both mesh structures yielded similar evaporation times when compared to the data from the literature, the tetrahedral mesh appears to better represent the vaporization process, as its results were closer to the literature data for all droplet diameters.

7.6 Comparison between tetrahedral and hexahedral meshes

7.7.1 Particle cloud

The behavior of the respiratory droplets along the domain was studied for 10 µm, 50 µm, and 100 µm droplets at low and high relative humidity conditions. The visual representation of the 1 µm droplet clouds was excluded because their evaporation occurred almost instantly after

release. As shown in Figures 23 and 24, for the 10 µm and 50 µm respiratory particles, respectively, the particle cloud evolution within the computational domain was similar for the respective meshes at different time intervals, until they evaporated.

Figure 23- Visual representation of respiratory particles 10 µm using tetrahedral and hexahedral meshes at the specified interval of time under relative humidity conditions of (a) at 0% and (b) at 80%

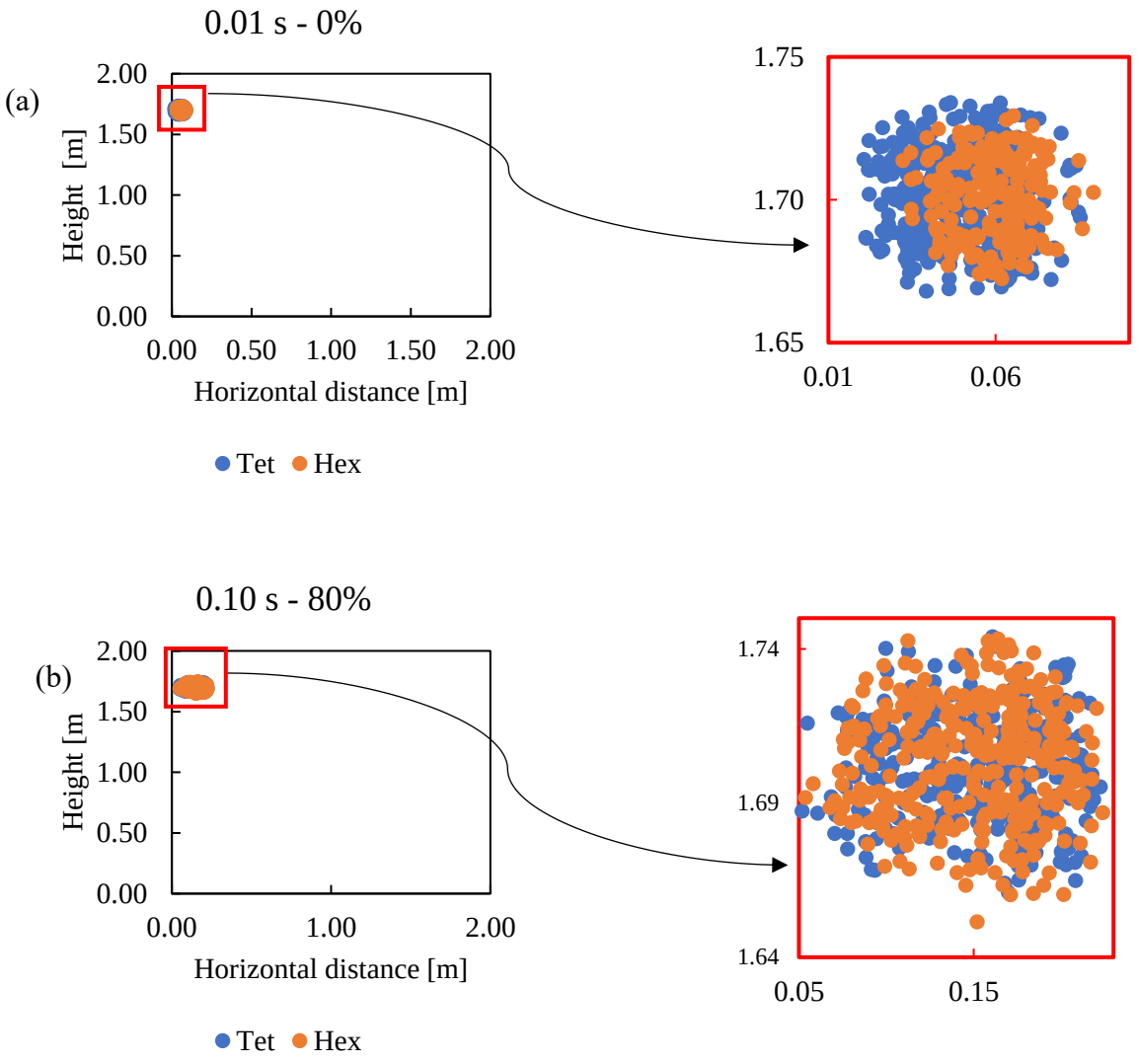

(Self-elaborated)

Figure 24- Visual representation of respiratory particles 50 µm using tetrahedral and hexahedral meshes at the specified interval of time under relative humidity conditions of (a) at 0% and (b) at 80%

(a)

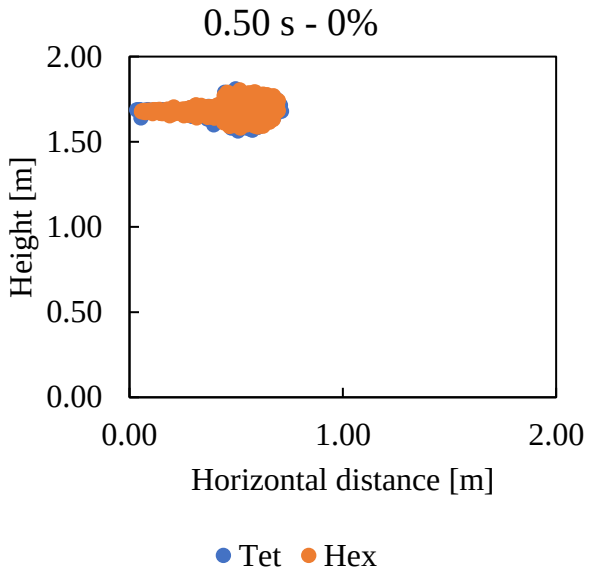

(b)

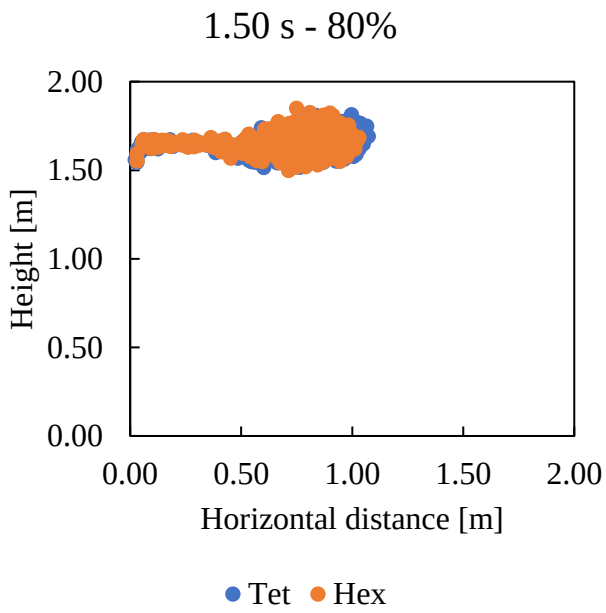

(Self-elaborated)

Figure 25- Visual representation of respiratory particles of 100 µm in diameter using tetrahedral and hexahedral meshes at the specified interval of time under a relative humidity condition of 0%

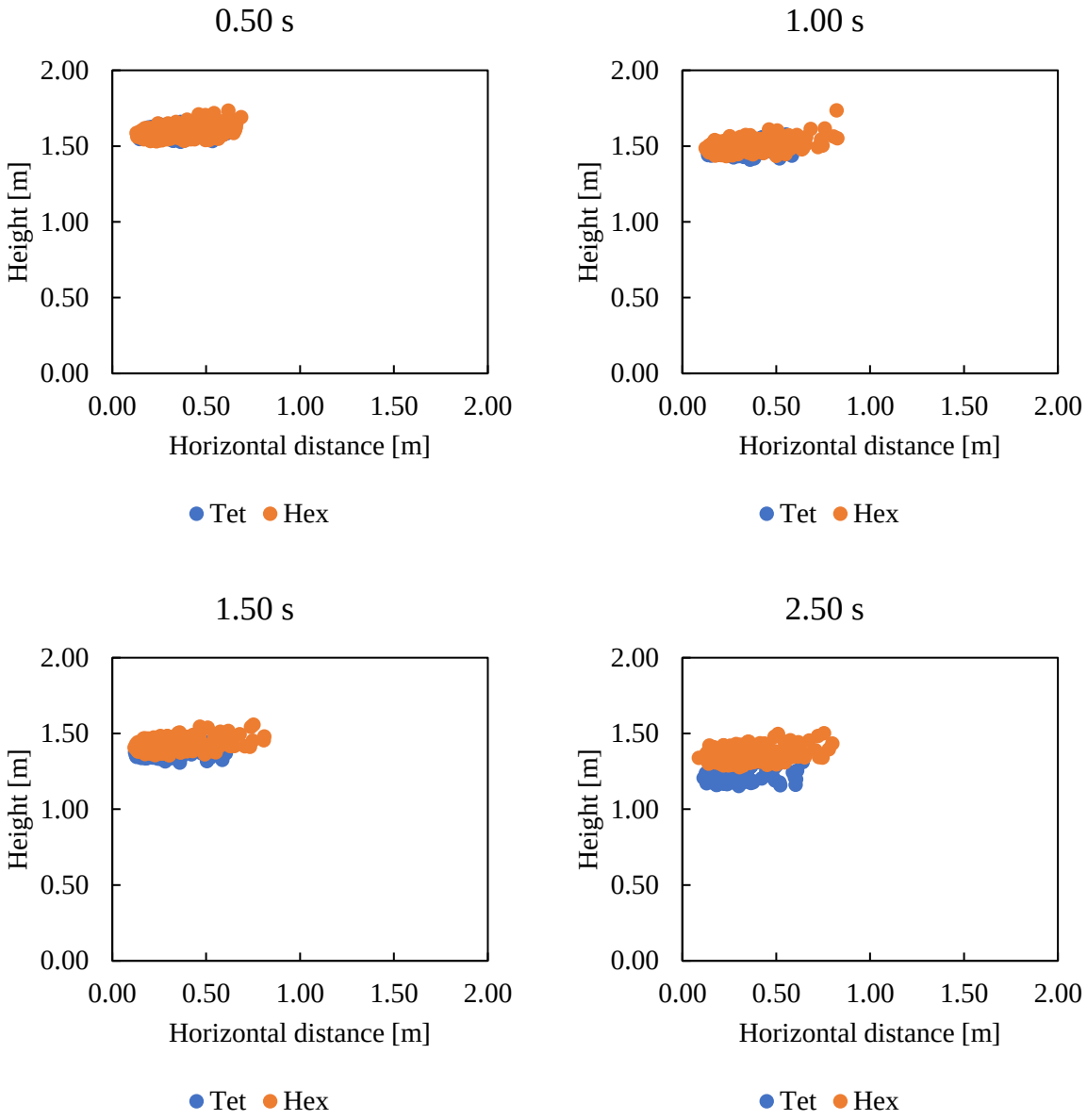

(Self-elaborated)

As shown in Figure 25, where results for 0% relative humidity are presented, different results were obtained using the graded tetrahedral and hexahedral meshes when larger respiratory droplets were simulated.

Figure 26- Visual representation of respiratory particles of 100 µm in diameter using tetrahedral and hexahedral meshes at the specified interval of time under a relative humidity condition of 80%

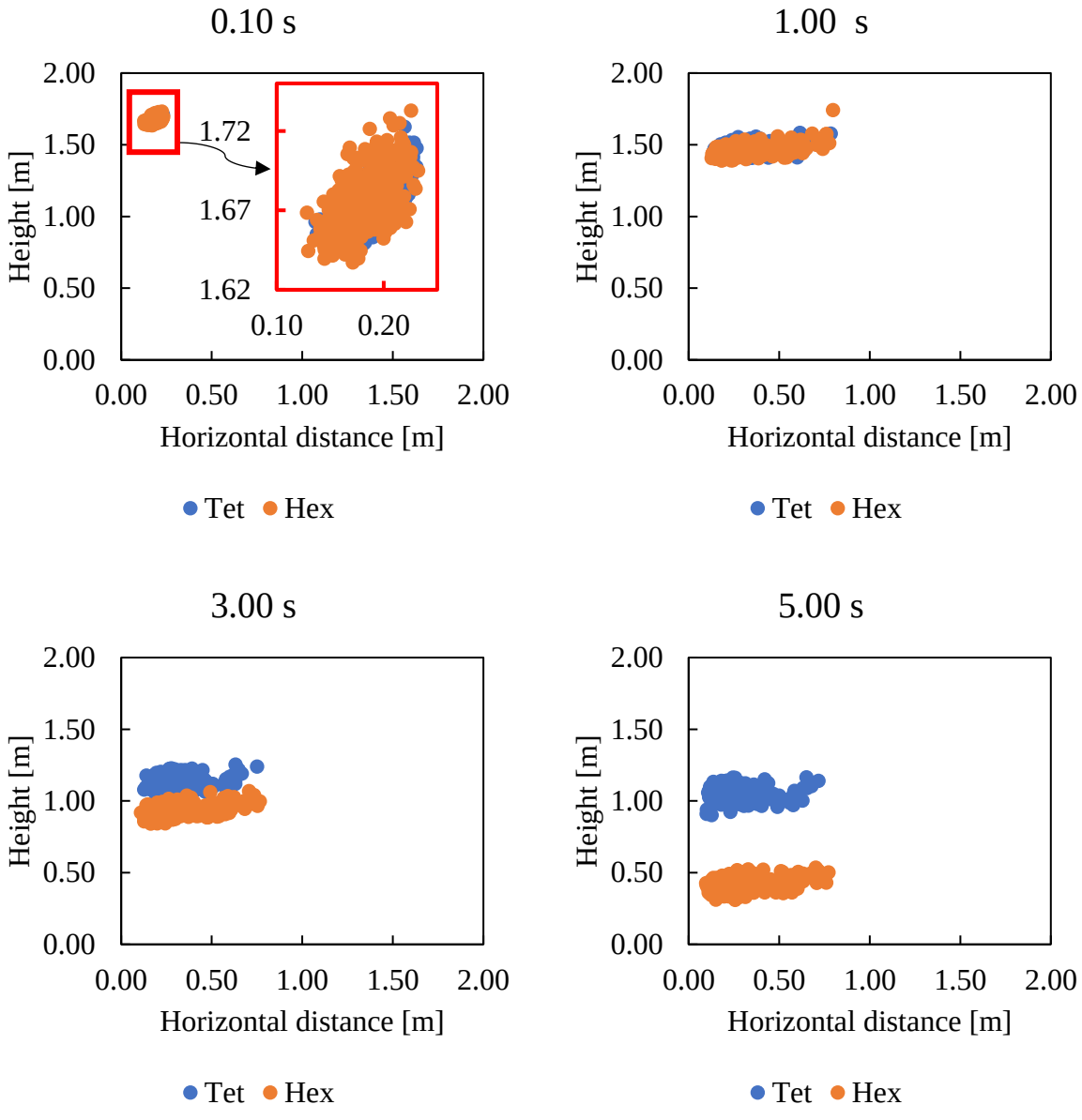

(Self-elaborated)

This category represents the largest droplet diameter (100 µm) used in this study. For t = 0.5 s and t = 1 s, the particle clouds remain very similar. However, as the simulation advances in time, these clouds begin to diverge. These differences are even higher when the relative humidity of air increases to 80%, as can be seen in Figure 26, indicating that the mesh is influencing the results.

To evaluate how the mesh structure influences particle dispersion, it is useful to analyze the mesh regions, as identified in Figure 27, which shows a cross-section of the tetrahedral and hexahedral meshes at the center of the domain along the particle path. In this figure, the different refinement levels are identified as L1 to L6, with L1 representing the smallest cells and L6 representing the largest cells.

Figure 27- (a) Tetrahedral mesh and (b) hexahedral with the grading regions

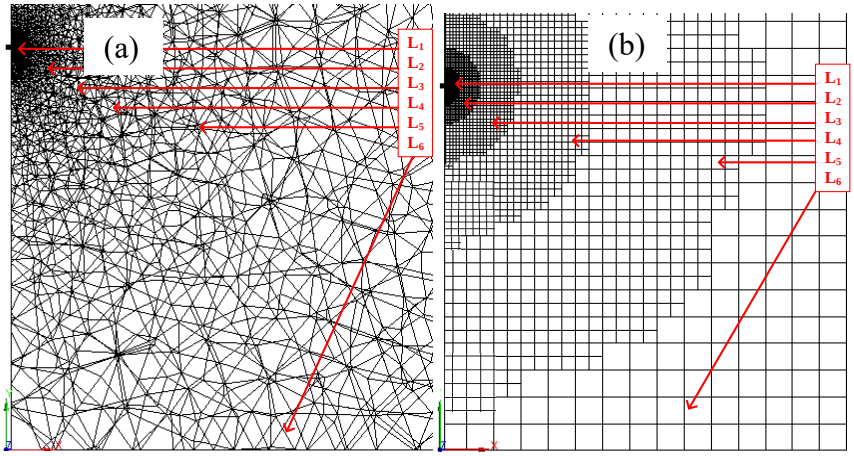

(Self-elaborated)

When comparing Figures 23 and 24 to Figure 27, it can be seen that the smaller droplets (10 µm and 50 µm) evaporate before reaching the regions where the mesh is coarser. Most of them evolved and evaporated within the L_1, L_2, L_3, and L_4 regions.

The larger droplets (100 µm), however, reach a region farther from the mouth, where the meshes are coarser, before evaporating. These differences were even greater under 80% relative humidity. In these cases, the use of a hexahedral mesh resulted in droplets that completed the flow trajectory, falling onto the domain floor without evaporating and, consequently, advancing to the

L_6 region. However, when the same calculation was carried out using a tetrahedral mesh, total evaporation of the respiratory droplets was observed within the L_5 region.

7.7.2 Particle evaporation/trapping time

In addition to comparing the particle clouds computed using the graded tetrahedral and hexahedral meshes, the evaporation/trapping time of the respiratory particles was also calculated. The evaporation start time was defined as the time when the first respiratory droplet evaporated from the flow domain, and the evaporation/trapping end time was the moment when the last droplet either evaporated or fell to the ground. These times are presented in Table 17 for different size droplets, air humidity and mesh structures. The mesh regions where the particle cloud is present before complete evaporation or trapping are also shown in this table.

Table 18- Droplet evaporation time calculated by the tetrahedral and hexahedral meshes respectively at different droplet sizes and air humidity

Size/Humidity	Mesh	Evaporation start time (s)	Evaporation/trapping end time (s)	Mesh Region
10 µm/ 0%	Tet	0.063	0.128	L1/L2
	Hex	0.037	0.083	L1/L2
10 µm/ 80%	Tet	0.078	0.164	L1/L2
	Hex	0.084	0.159	L1/L2
50 µm/ 0%	Tet	0.767	0.921	L1 to L4
	Hex	0.700	0.913	L1 to L4
50 µm/ 80%	Tet	1.597	3.083	L1 to L5
	Hex	1.597	2.310	L1 to L5
100 µm/ 0%	Tet	4.725	4.811	L1-L5
	Hex	2.783	2.895	L1-L5
100 µm/ 80%	Tet	5.818	6.255	L1-L5
	Hex	No evaporation	8.5 s trapping time	L1-L6

(Self-elaborated)

As expected, 10 µm droplets evaporate rapidly (within 0.2 seconds), so the observed differences in evaporation start and end times between the mesh structures are not significant for this study. For 50 µm droplets at 0% air humidity, both the evaporation start and end times are nearly identical for both meshes. In these simulations, the droplet clouds remain within the finer mesh cell regions (L_1 to L_4). However, for 50 µm particles at 80% air humidity, while the evaporation initiates at the same time for both meshes, the evaporation end time shows a difference of approximately 0.8 seconds. These differences are even higher for 100 µm droplets, where the particles do not evaporate at all with the hexahedral mesh, as depicted in Figure 28. This figure shows the particle cloud spread on the floor 8.5 seconds after release. Furthermore, a difference of almost 2 seconds was observed in the evaporation end time between the mesh structures.

Figure 28- Respiratory droplets with a diameter of 100 µm laying on the bottom of the domain floor of a closed space with a relative humidity of 80% calculated by a hexahedral mesh

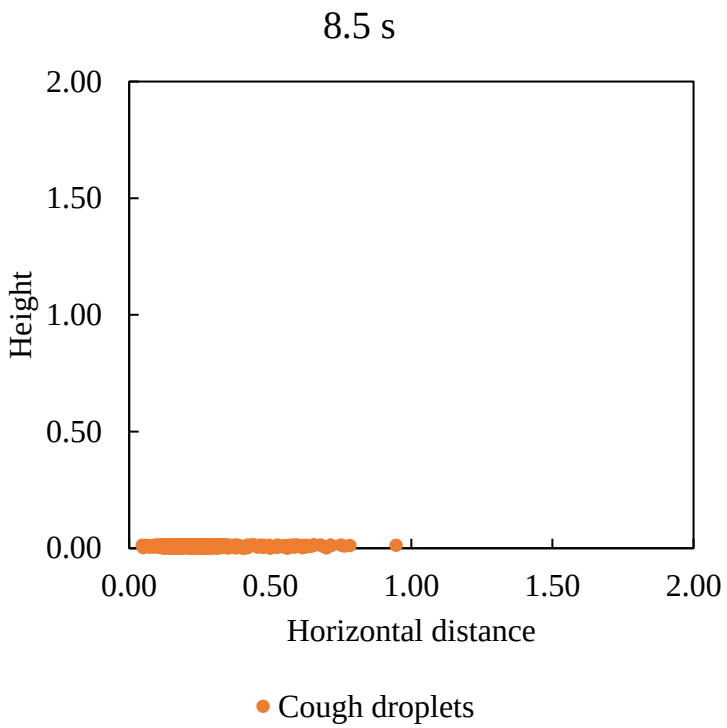

(Self-elaborated)

While the results obtained using the tetrahedral mesh were closer to the data from Redrow et al. (2011) and Li et al. (2020) for 100 μm droplets, as shown in Figures 21 and 22, a comparison with the study by Oh et al. (2024) suggests the hexahedral mesh may be more accurate. Oh et al. (2024) used 80 μm droplets (which is closer to the diameter used in this study) in their research and observed droplet deposition on the floor. Additionally, other studies indicate that within this particle size range, evaporation of respiratory droplets is unlikely, particularly at medium or higher relative humidity, as reported by Yan et al. (2019) and Li et al. (2018). These observations align with the results calculated by the hexahedral mesh.

7.7.3 Total CPU time

To evaluate CPU time differences across simulations, 0.52 s of flow was run for all cases, consistent with the duration of a single human cough as reported by Li et al. (2020). However, since respiratory droplets smaller than 50 μm evaporated rapidly within this timeframe, regardless of relative humidity, CPU time was evaluated only for droplets with initial sizes of 50 μm and 100 μm, at 0% and 80% air humidity, as detailed in Table 18.

Table 19- Total CPU time measured at t = 0.52 s for the simulation

		Tet mesh		Hex mesh	
Humidity		50 μm	100 μm	50 μm	100 μm
0 %	Total CPU Time (h)	197.25	192.97	223.02	224.75
80 %		196.21	198.23	220.84	220.18

(Self-elaborated)

As observed, there are slight differences in the CPU time required to simulate the respiratory droplet particles on both tetrahedral and hexahedral meshes. On average, the simulations using the hexahedral mesh required 13% more time than those using the tetrahedral mesh.

8. PART 3 - INFLUENCE PHASE COUPLING, DROPLET DIAMETER AND RELATIVE HUMIDITY ON HUMAN COUGH DROPLET EVAPORATION

In this part of the studies, the effect of coupling, droplet diameter and relative humidity, which are important factors that influence the behavior of the droplets released during respiratory events is studied. The studies at this stage were carried out using a 3-D model. There were no significant differences observed in the application of standard k-ε, (SST) k-ω and RSM turbulence models, therefore, the (SST) k-ω was applied in this part of the study. The choice for this turbulence model was motivated by its capacity to calculate the flows involving adverse pressure gradient with stability even though it is computationally more expensive when compared to k-ε. It has advantages over the other two-equation models, due to its improved transport feature. Additionally, (SST) k-ω predicts results similar to RSM, which is a more sophisticated turbulence model. Even though in previous studies, hexahedral mesh was recommended, tetrahedral mesh will be applied, however with a different configuration which makes it applicable.

8.1 Computational domain & mesh

To mimic and simulate human cough, a computational domain of 2.5 m x 1 m x 2.5 m was considered (Figure 29). The cough inlet region (mouth region) was created at 1.70 m above ground level. In terms of modeling and simulation, the mouth of a human presents a complex geometry that can reflect in the computational cost, therefore a simple quadrilateral geometry with an area of 4 cm^2 was applied in this work; a type of inlet also used by Li et al. (2020), D'Alessandro et al. (2021) and Ge at al. (2022). The inlet surface starts at x = -0.02 m and meets the cough chamber at x = 0.00 m. Therefore, in the presentation of results with reference to the x-axis, the horizontal distance-time curves of the particles start at the negative x-axis. That means, the particles travel 0.02 m before they start registering positive distances. This is seen in the results presented in droplets with 1 μm.

Figure 29- Cough chamber built with ANSYS design modeler 14.5

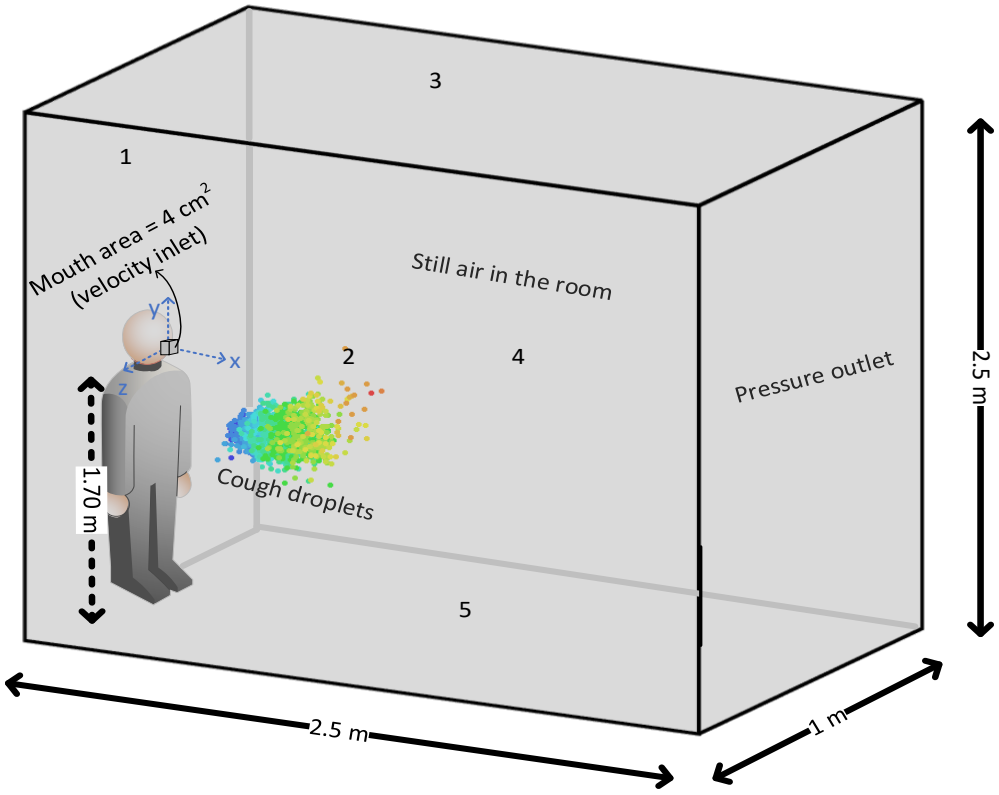

(Self-elaborated)

Next step was the creation of the numerical mesh. In this part of the study, the unstructured tetrahedral mesh was used. To apply this mesh, the numbers of elements used in the previous study (Section 7) was increased to increase its precision. This was done strategically to avoid errors that were observed in the results calculated in comparison with the hexahedral mesh. The mesh was built in the same way where higher cell density was attributed at the inlet region as presented in Figure 30. The letters A, B, and C are used to represent the inlet, walls, and outlet, respectively as presented in Figure 30.

The mesh configurations, specifically the minimum element growth rate used in this part of the study is similar to that applied on the tetrahedral mesh studied in Section 7.

Figure 30- Mesh with its boundaries built using Ansys Meshing 14.5

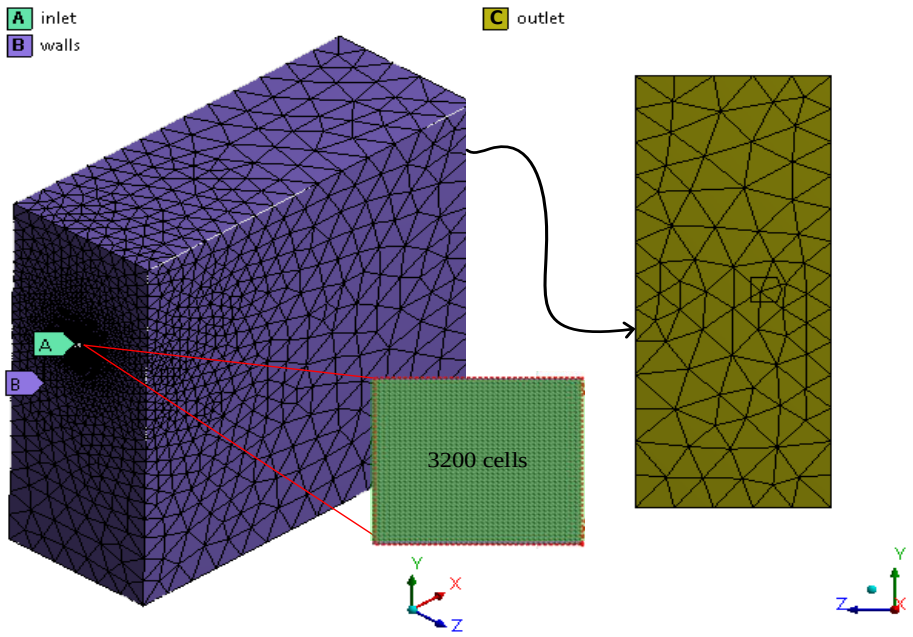

(Source: self-elaborated)

The number of respiratory particles injected in this stage of the research was adjusted. For instance, 3200 cells were used, in this work, 400 cells were used at the inlet region of the domain.

8.2 Numerical process

The conditions used at this stage are similar to those applied in Section 7.

8.2.1 Simulated cases

At this stage, three different computational models M1 and M2 were tested through the variation of cough droplet diameter and relative humidity, which are parameters that can influence the spread of contaminated droplets emitted during intense respiratory events. The respective models and their physical configurations are presented in Table 19.

Table 20- Models 1 and 2 and their respective physical configurations

	Model	
Physics	M1	M2
Turbulence model ($\mathbf{k-\omega}$) SST	✓	✓
Energy Equation	✓	✓
Two-way coupling (phase)	×	✓
Unsteady particle tracking	✓	✓
Temperature-dependent latent heat	✓	✓
Specie transport	✓	✓
Breakup (Taylor Analogy Breakup)	✓	✓
Stochastic Tracking	✓	✓

(Self-elaborated)

In M1, there is a one-way phase coupling between the respiratory droplets and air. In M2, the coupling is two-way.

Apart from the models presented in Table 19, the relative humidity of the room (computational domain) and droplet diameter were also varied in the simulations and their influence on the droplets' movement and evaporation were evaluated (Table 20).

Table 21- Simulation cases and their respective characteristics

Relative humidity (%)	**Droplet diameter (µm)**			
-	1	10	50	100
0	Case 1	Case 3	Case 5	Case 7
80	Case 2	Case 4	Case 6	Case 8

(Self-elaborated)

Additionally, parameters such as flow rate, inlet area, temperature, domain temperature, cougher's height, and the range of cough droplet diameter were obtained from Li et al. (2018), and Li et al. (2020), thus presented in Table 21.

Table 22- Simulation conditions

Nomenclature	Magnitude/characteristics
Species	Air and water
Cougher's mouth areas	4 cm^2
Cough temperature	310.15 K
Room Temperature	293.15 K
Cougher's height	1.70 m
Droplet diameter	1 µm, 10 µm, 50 µm and 100 µm

(Self-elaborated)

8.2.2 *M*esh independence test

Since tetrahedral mesh can present inaccuracy in the calculation of respiratory droplets emitted, the mesh was projected to have elements above the number (150, 000 elements) applied in Section 7 for the tetrahedral mesh.

Therefore, the mesh independency test was carried out with three different sizes ($G1 < G2 < G3$) with details presented in Table 22. All of them were built with growth rates of 1.10 and minimum element lengths of 5.0×10^{-5} m. The maximum element size in each case was established according to the geometric progression presented in Equation 8.1.

$$a_n = a_1 r^{n-1} + a_1 \quad 8.1$$

where a_1 corresponds to the maximum element size of G1, n is the n-th term grid, r is the common ratio (for instance $r = l_{G2}/l_{G1}$, where l_{G2} and l_{G1} are the respective element sizes of meshes G2 and G1). It is important to note that by decreasing the maximum element length, finer meshes are obtained with higher element density at the inlet region. The choice for this mesh size distribution parameter makes it possible to have a large range of maximum element lengths.

Table 23- Mesh parameters.

Mesh parameters	G1	G2	G3
Min. cell volume $x10^{-12}$ (m^3)	5.18	5.08	3.62
Max. cell volume (m^3)	$5.31x10^{-2}$	$1.96x10^{-3}$	$1.32x10^{-4}$
No. of nodes	41349	42145	56162
No. of elements	229253	233327	309908
Av. skewness	0.23	0.23	0.23

(Self-elaborated)

8.2.3 Droplet evaporation

A mesh independence test was conducted using the droplet size parameter. Specifically, the reduction of droplet diameter caused by evaporation was applied. The diameter was monitored at specific time intervals. It is important to state that this test did not witness total evaporation.

Figure 31 shows the mean droplet evaporation of 3200 cough droplets released after 5 s (under Table 20 conditions).

Figure 31- Mean droplet diameter as a function of time for different meshes

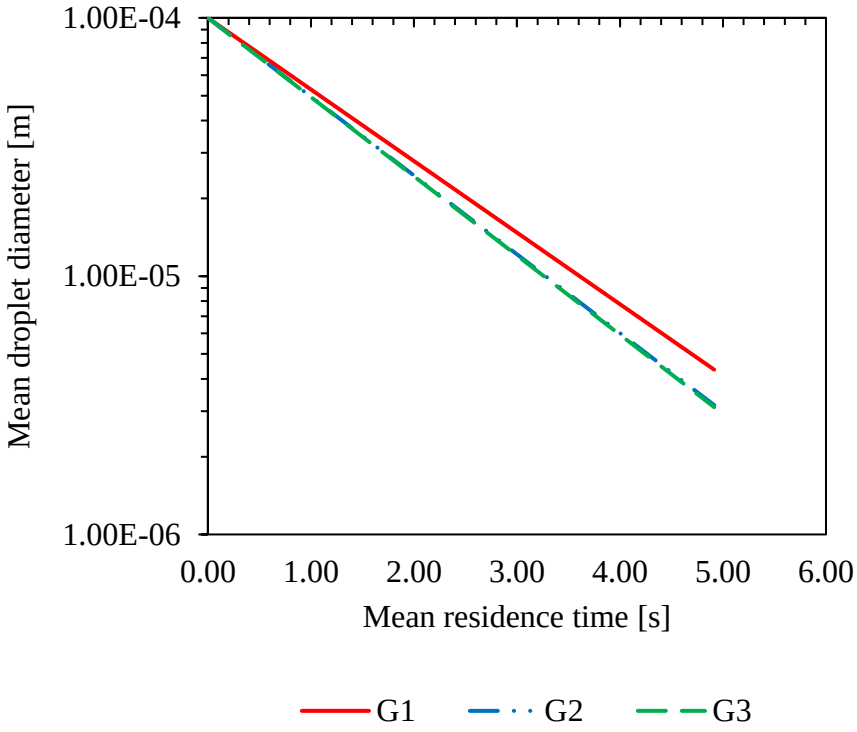

(Self-elaborated)

After 5 s of droplet release, it could be observed that G2 and G3 presented similar mean droplet diameters (3.16 x10^{-6} m and 3.24 x10^{-6} m, respectively), while G1 which is the coarsest mesh presented the largest mean droplet size (4.35x10^{-6} m). Further refinement did not produce significantly different results, hence mesh independency (similarly applied in Bahramian et al., 2023) was established.

8.2.4 Mesh choice

In studying mesh independency through droplet evaporation, G2 was chosen for its balance of computational cost and accuracy, as identified by Bahramian et al. (2023). G2 produced results comparable to G3 but used elements twice the size of those in Section 7. Specifically, G2 was approximately 58% more cost-effective than G3 in terms of total CPU time for the simulation. A visual representation of G2 mesh composition and its skewness is presented in Figure 32.

Figure 32- G2 aspect ratio distribution of mesh built using non-uniform tetrahedral elements

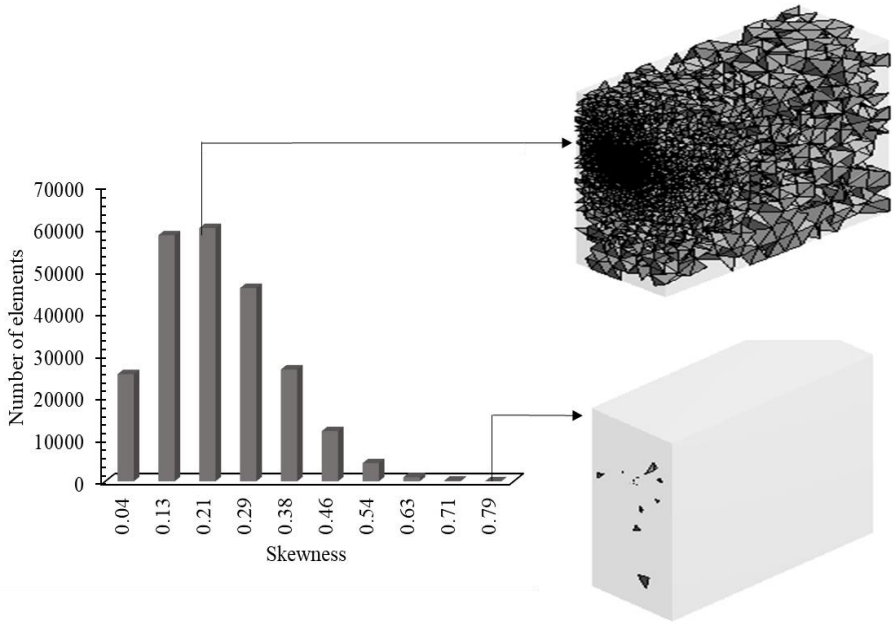

(Self-elaborated)

It can be noted from Figure 32 that the majority of the elements have low skewness, hence denoting an increased quality which is reflected in the results obtained in this work. To be specific, G2 had a minimum, maximum, and average skewness of 1.28×10^{-3}, 0.83, and 0.23, respectively, which is within the suggested range by Santana et al. (2019).

8.2.5 Validation of the results

The mesh selected in Section 6 (Part 1) was used to reproduce the single droplet evaporation presented by Li et al. (2020) at conditions presented in Table 8. The authors used three droplet diameters (1 μm, 10 μm, and 100 μm) at different relative humidity conditions in a quiescent room. The mimicking was carried out using the same diameters but with only 0% relative humidity (which is one of the conditions used by the authors). The results are presented in Figure 33.

Figure 33- Droplet evaporation of cough droplets in a quiescent room at 0% relative humidity

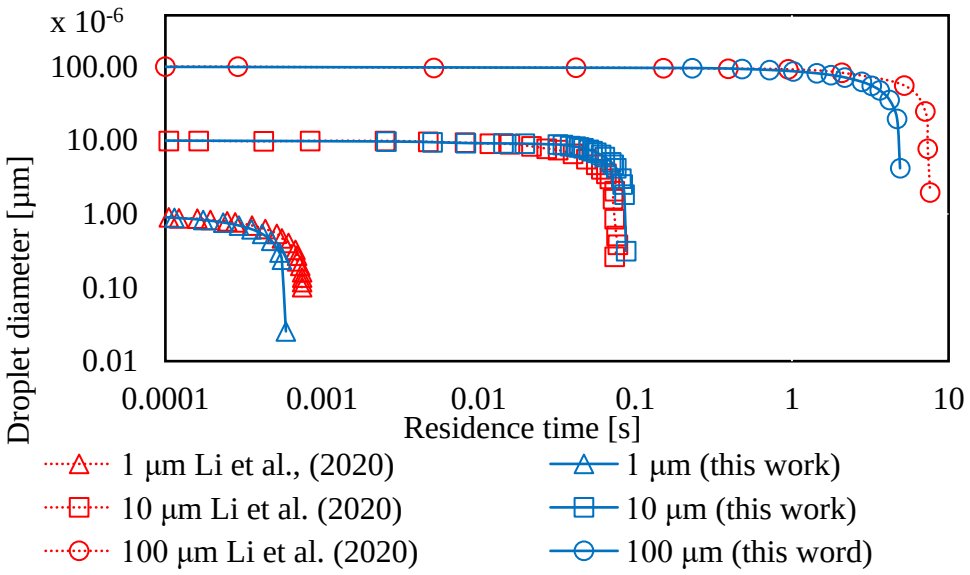

(Self-elaborated)

It can be seen that similar to droplet evaporation was presented by Li et al. (2020). Even though 3200 particles were used in this work against a single droplet used by the authors, the results were similar. This number increases the computational cost, however offers a result suitable to represent cough droplets.

8.2.6 Model, humidity, and diameter influence

The cases are presented and discussed in pairs. The three coupling models applied in this study are permuted between the two relative humidity (0% and 80%) conditions and the droplet sizes (1 µm, 10 µm, 50 µm, and 100 µm), and the results are discussed. Since 3200 uniform droplets were released in a single time-step, presenting all the particles will be bulky, therefore mean droplet diameter was used. All the plots presented in this section are with reference to the mean droplet diameter of 3200 droplets released at the same time, therefore, when a curve terminates, it means the particle has completely evaporated, otherwise, it continues until the particle touches the ground.

➢ *Cases 1 and 2*

Here the particles have 1 μm in diameter, however, Cases 1 and 2 are respectively simulated at 0% and 80% relative humidity conditions. The results are presented in terms of horizontal distances attained by the respiratory droplets as presented in Table 23.

The cough droplets traveled relatively short distances before they evaporated. In a realistic description, the particles evaporated instantly after release. In Case 1, the horizontal distances covered slightly different distances for M1 and M2. In Case 2, even though the particles also covered very short horizontal distances, the differences were larger

Table 24- Horizontal distance traveled by cough droplets using different coupling models and atmospheric conditions

	Case1		Case2	
Model	Horizontal distance	Standard deviation	Horizontal distance	Standard deviation
M1	$3.47x10^{-5}$ m	$4.66x10^{-6}$	$3.65x10^{-5}$ m	$2.03x10^{-6}$
M2	$3.46x10^{-5}$ m	$3.56x10^{-6}$	$6.75x10^{-5}$ m	$7.88x10^{-5}$

(Self-elaborated)

Specifically, M1 calculated the least. The low standard deviations in all cases show that the data points obtained were clustered around the mean horizontal distance, that is to say, the particles were relatively close before evaporation. From the horizontal distances presented in Table 23, it could be seen that the effect of the coupling models was that among the numerical models, coupling was insignificant, however, evaporation was affected by relative humidity, as expected.

➢ *Cases 3 and 4*

They were simulated at 0% and 80% of relative humidity, respectively, using a 10 μm particle diameter. The results which are in the form of the vertical, horizontal, and particle distances plotted against time, and the particle cloud are presented in Figure 34.

Figure 34- Models 1 and 2 using Cases 3 and 4 (a) horizontal direction (b) vertical direction (c) M2 Case 4; dispersed particle cloud formed at t = 0.10 s with the color grades indicating its advancement in the computational domain

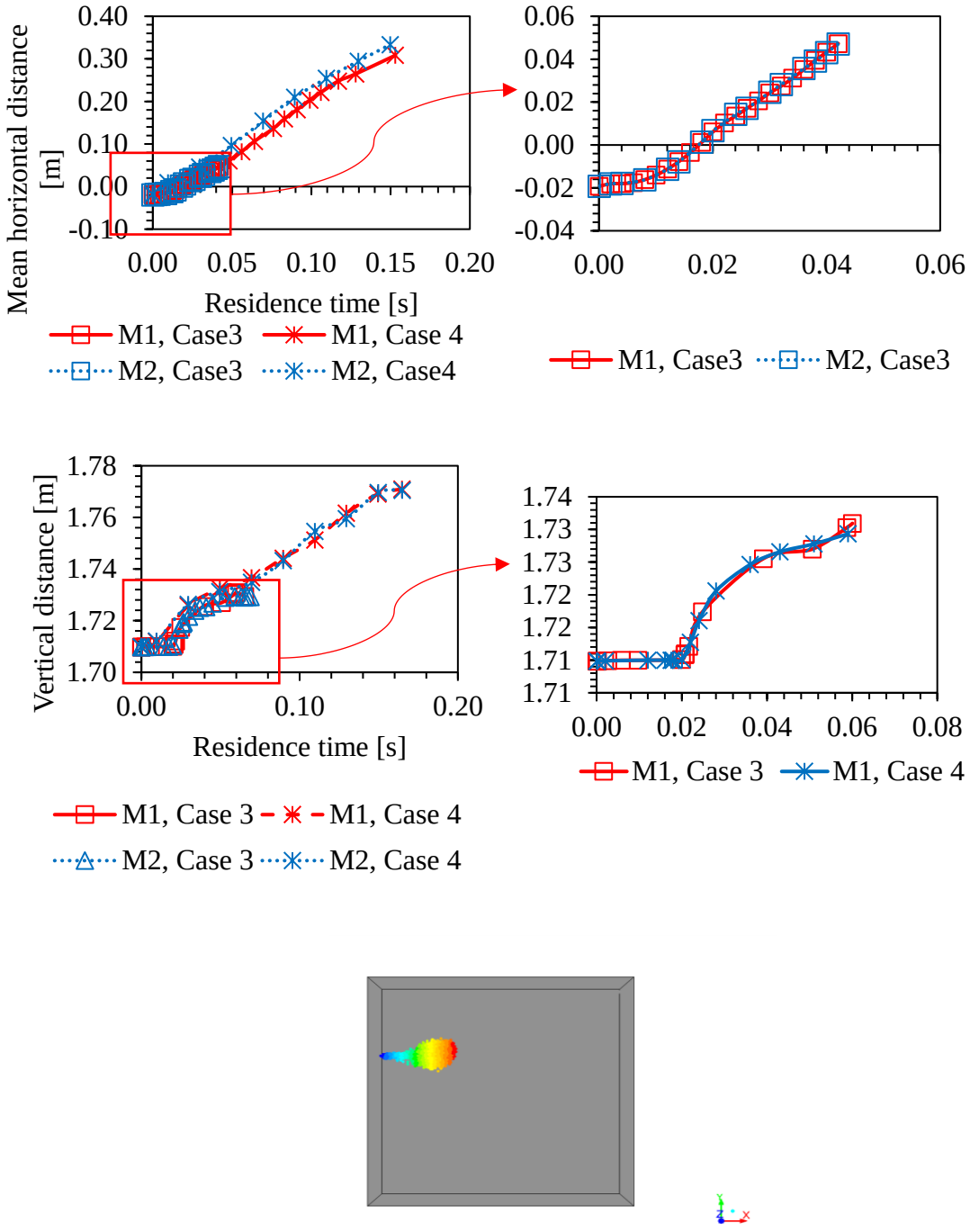

(Self-elaborated)

The particles are traced from the moment of their release. They travel through the calculated distances until they disappear as a result of evaporation. The end of the curve marks total evaporation of the droplets.

The horizontal (a) and vertical (b) distances traveled by the droplet particles in Case 3 were similar for all models to indicate the insignificance of the effect of the discrete phase on the continuous phase. In Case 4, M1 was slightly different from M2 in terms of the horizontal distance covered by the particles. For instance, at 0.15 s M1 calculated a horizontal distance of 0.31 m while M2 calculated 0.33 m. In a more detailed analysis, it is observed that the particle cloud released suddenly expands with an even distribution in the x, y, and z directions (Figure 34 c) the blue, green, and red zones refer to short, intermediate, and advanced distances covered by the particles. In Case 3, the particles began to evaporation at 0.042 for both M1 and M2, and the maximum horizontal distance covered by the droplets was 0.047 m (Figure 34a). It can be noted that models M1 and M2 registered the same initial evaporation time and horizontal distance. In the vertical direction in Case 3, M1 and M2 registered 0.030 m droplet dispersion above the cough level before evaporating. However, using the operational conditions in Case 4, the particle cloud traveled farther due to higher relative humidity conditions. In the vertical direction, the particle cloud attained a maximum vertical distance of 0.07 m by applying Case 4 on M1 and M2, which represents an increase of 80% when compared to Case 3.

- *Cases 5 and 6*

These cases were simulated at 0% and 80% of relative humidity, respectively, using a 50 µm particle diameter. The results are presented in Figure 35.

For Case 5, M1 and M2 presented slightly different horizontal distances covered by the respiratory droplets. While M2 found a horizontal distance x = 0.72 m, M1 presented x = 0.81 m at 1.19 s. As for Case 6, M1 gave x = 1.24 m while M2 registered x = 1.34 m at 7.00 s. In a more detailed analysis, even though the particles in these cases are larger when compared with Cases 3 and 4, the particle cloud formed (Figure 35 c) was similar for M1 and M2. In Case 5, evaporation was initiated at 1.19 s and 1.21 s for M1 and M2.

Figure 35- Models 1 and 2 using Cases 5 and 6 (a) horizontal direction (b) vertical direction (c) M2 Case 6; dispersed particle cloud formed at t= 0.10 s with the color grades indicating its advancement in the computational domain

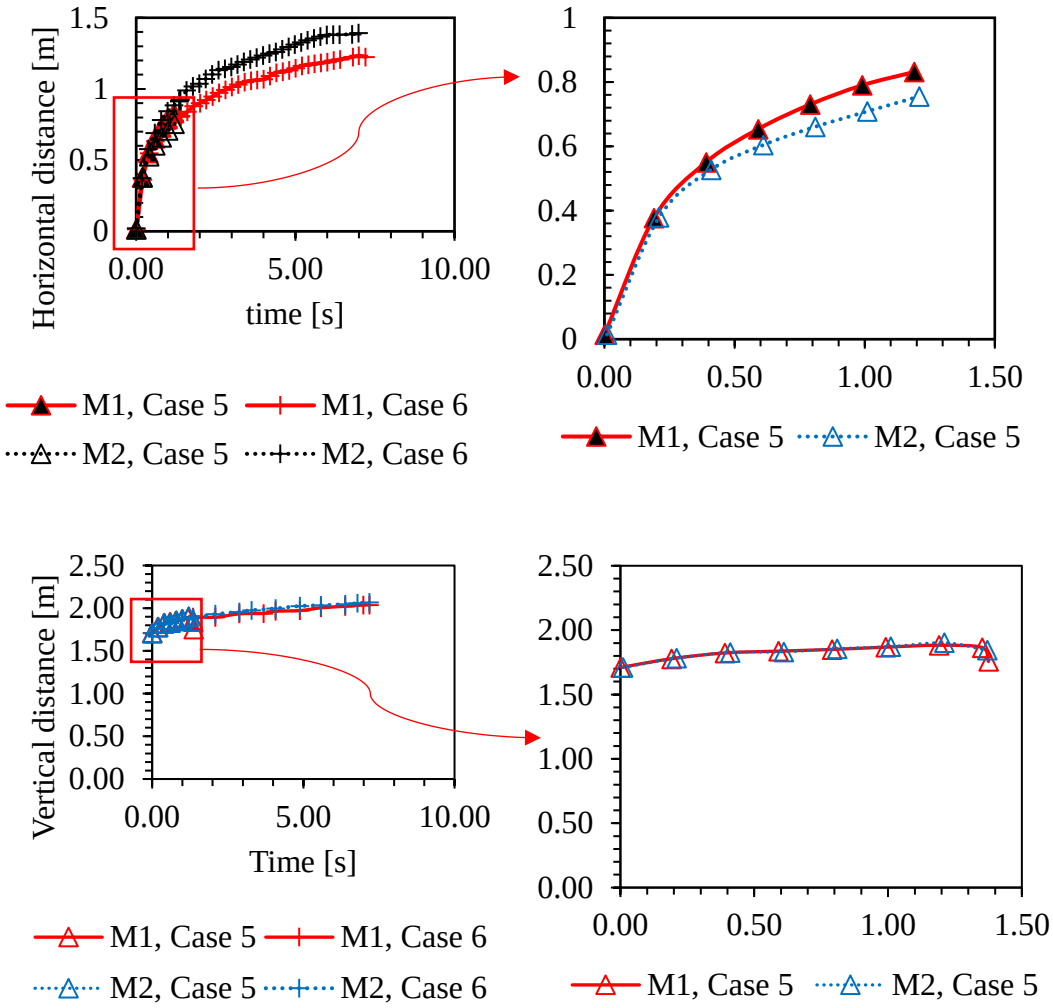

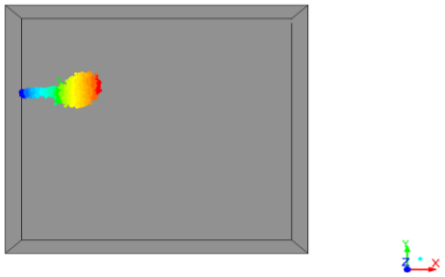

(Self-elaborated)

At those respective times, horizontal and vertical distances were 0.83 m and 0.76 m, and 0.18 m and 0.14 m, respectively. As for Case 6, the cough particles lasted longer before they evaporated due to higher relative humidity. For instance, when compared to Case 5, the evaporation initial times increased by about 142% while the maximum horizontal distances increased by over 30%. It is important to note that when 50 µm particles (Cases 5 and 6) were released, they fell until one-fourth of the cougher's height (1.70 m) before totally evaporating.

Even though the 50 µm droplets were pulled by gravity, they persisted longer and travelled a farther distance than 10 µm droplet, in the still air both at 0% and 80%. As droplets fall, they reduce in size due to evaporation, and that affects their residence time in air. Normally, smaller droplets are impacted more by drag forces, thereby decreasing their terminal velocities (Bagheri and Bonadonna, 2016). Since smaller cough droplets have little inertia, they can easily be deflected leading to a prolonged persistence in air with the aid of a high relative humidity condition. Therefore, medium particles close to 50 µm, and under a high relative humidity condition can travel

- *Cases 7 and 8*

Lastly, the analyses were simulated at 0% and 80% of relative humidity, respectively, using 100 µm particle diameter. The results are presented as horizontal and vertical distances against time The graphical results are presented in Figure 36.

In Case 7, M1 and M2 calculated similar horizontal distances between $t = 0$ s and $t = 0.99$ s (a region where inertial force predominates and acts in the horizontal direction). At $t = 2.00$ s, the particle cloud had lost its inertial forces, therefore the gravitational force predominated thereby making the particles fall vertically until they evaporated (Case 7) or settle at the bottom of the computational domain (Case 8). In summary, the horizontal and vertical distances calculated by M1 and M2 (Figure 36 a) were slightly different. For instance, M1 and M2, the particles attained maximum horizontal distances of 0.92 m and 0.81 m, at 4.88 s, respectively. And the maximum vertical heights attained by the cough droplets were 1.77 m and 1.73 m.

Figure 36- Models 1 and 2 using Cases 7 and 8 (a) horizontal direction (b) vertical direction (c) M2 Case 8; compacted particle cloud formed at; Left t= 0.10 s and Right 10.00 s with the color grades indicating its advancement in the computational domain

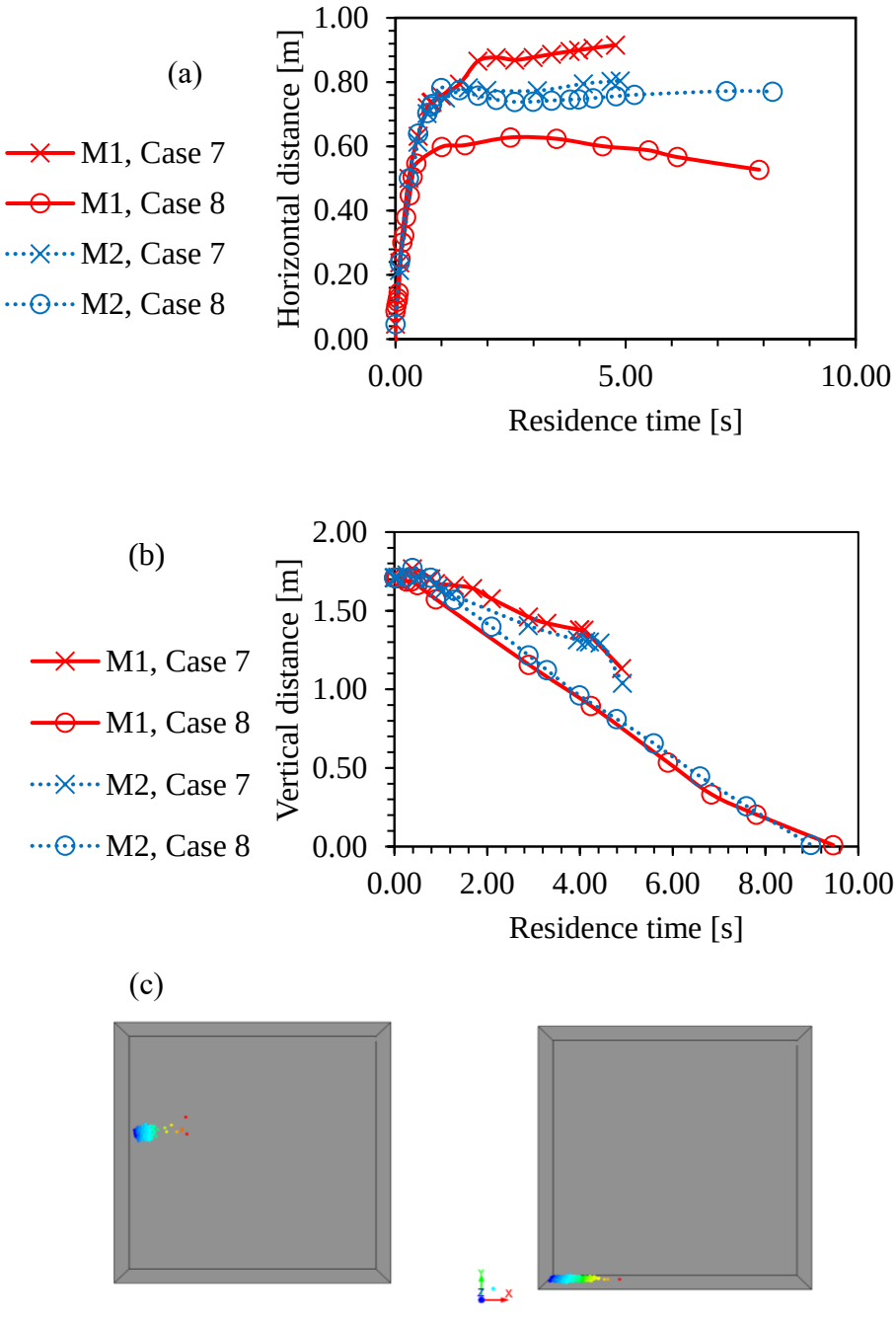

(Self-elaborated)

In Case 8, the horizontal distance versus time graph calculated from M1 and M2 were slightly different similar. For instance, they calculated the maximum horizontal distances of 0.63 m and 0.78 m, and maximum vertical distances of 1.71 m and 1.77 m, respectively. It is important to highlight that this is the only case where the particles completed the flow trajectory without totally evaporating as can be seen in Figure 36 c. The time of flight of the particles calculated (Case8) applying M1 and M2 were 9.46 s and 8.98 s, respectively.

The relative humidity of the coughing chamber, among other environmental factors is crucial in the behavior of droplets emitted from respiratory events. In this study, it was observed that cough droplets traveled longer horizontal distances at higher humidity conditions (80%) than a low one (0%) due to low evaporation rate; Cases 2 and 4 were good examples. That means at higher relative humidity conditions, the chances of IRD transmission are higher. To support this observation, Auler et al. (2020) carried out studies on COVID-19 spread in a tropical climate, and they concluded that higher relative humidity close to 80% favored the dissemination of the virus. This is because, at higher relative humidity atmospheric conditions, cough droplets need more time to evaporate than in lower relative humidity conditions. It is important to state that considerably large droplets and high relative humidity (such as in Case 8) fall to the floor giving way for an indirect form of contamination.

The particle diameter is another factor that is important in the dispersion of IRDs through droplets. However, it can be altered according to the RH of the area in focus. For instance, In Case 6, the longest horizontal distance (1.34 m for M2) covered by the cough particles in this work was observed under 80%. This is a clear effect of RH because a lesser distance was covered by the same particles at 0%. In other words, IRDs are more likely to spread through cough droplets where RH is high and the droplets are neither too small nor too big.

In conclusion, phase coupling had little effect on the distance traveled by the particle in both vertical and horizontal directions. Nevertheless, these slight differences are not significant due to the complexity of the fluid dynamics of respiratory events. However, since coupling has more computational cost tied to it, the uncoupled model is recommended in this work.

9. PART 4 - APPLICATION

In this last stage of the research, the simulation was carried out with the climatic conditions of São Carlos City, São Paulo, Brazil. The objective is to study the boundary conditions that can adequately be used in specific cases such as indoors and outdoors to observe the behavior of the respiratory droplets in more complex environmental conditions; specifically in the presence of one-directional wind at different velocities. It is important to highlight that this study was carried out using a 3D symmetric model to reduce computational cost. Additionally, (SST) k-ω turbulence model, one-way coupling was applied.

9.1 Geometry and mesh

In this part of the study, a relatively large computational domain was used. To ensure that the boundary layers of the respective wind velocity profiles used did not extend from the mannequin (which represents the person who releases the respiratory droplets). In such a situation, the behavior of the continuous and discrete phase (respiratory droplets) would largely be influenced by the velocity and direction of the wind, the shape of the mannequin, and all other factors such as air temperature and humidity. Such a strategy would allow the studies to be conducted under characteristics similar to large indoor or outdoor environments. The domain is presented in Figure 37.

Where B 01 is the respiratory droplets inlet, B 02 and B 07 are the wind inlet and outlet, respectively, and B 03, B 04, B 05, and B 06 are the walls. The wind inlet was placed so that it blows in the opposite direction to the respiratory droplets released from B 01. The 5 m length behind the mannequin is reserved for the particle flow.

The mesh was built using the same set-up applied in Section 7.2. Specifically, the configurations of g_2 hexahedral mesh were applied. Since a different geometry was used in this part of the study, different mesh features were generated as presented in Table 24. A more complex flow study was is focus, therefore hexahedral mesh was the ideal, due to its precision when compared to tetrahedral mesh with the same number of elements.

Figure 37- Respiratory flow domain

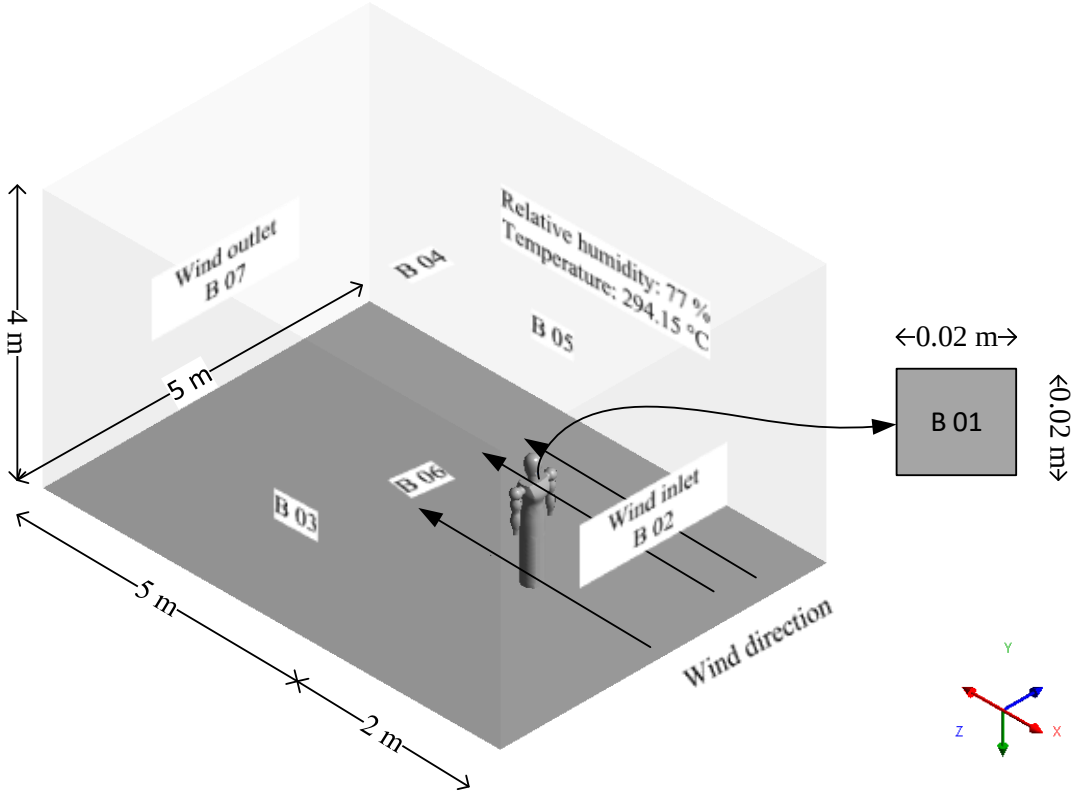

(Self-elaborated)

Table 25- Details of the mesh generated using hexahedral elements

Parameter	Value	Standard deviation
Nodes	340997	-
Elements	313053	-
Average skewness	1.856×10^{-2}	8.053×10^{-2}
Average aspect ratio	1.086	0.289
Average warping factor	2.552×10^{-3}	1.922×10^{-2}

(Self-elaborated)

Figure 38- Transverse section of the numerical mesh built with hexahedral elements

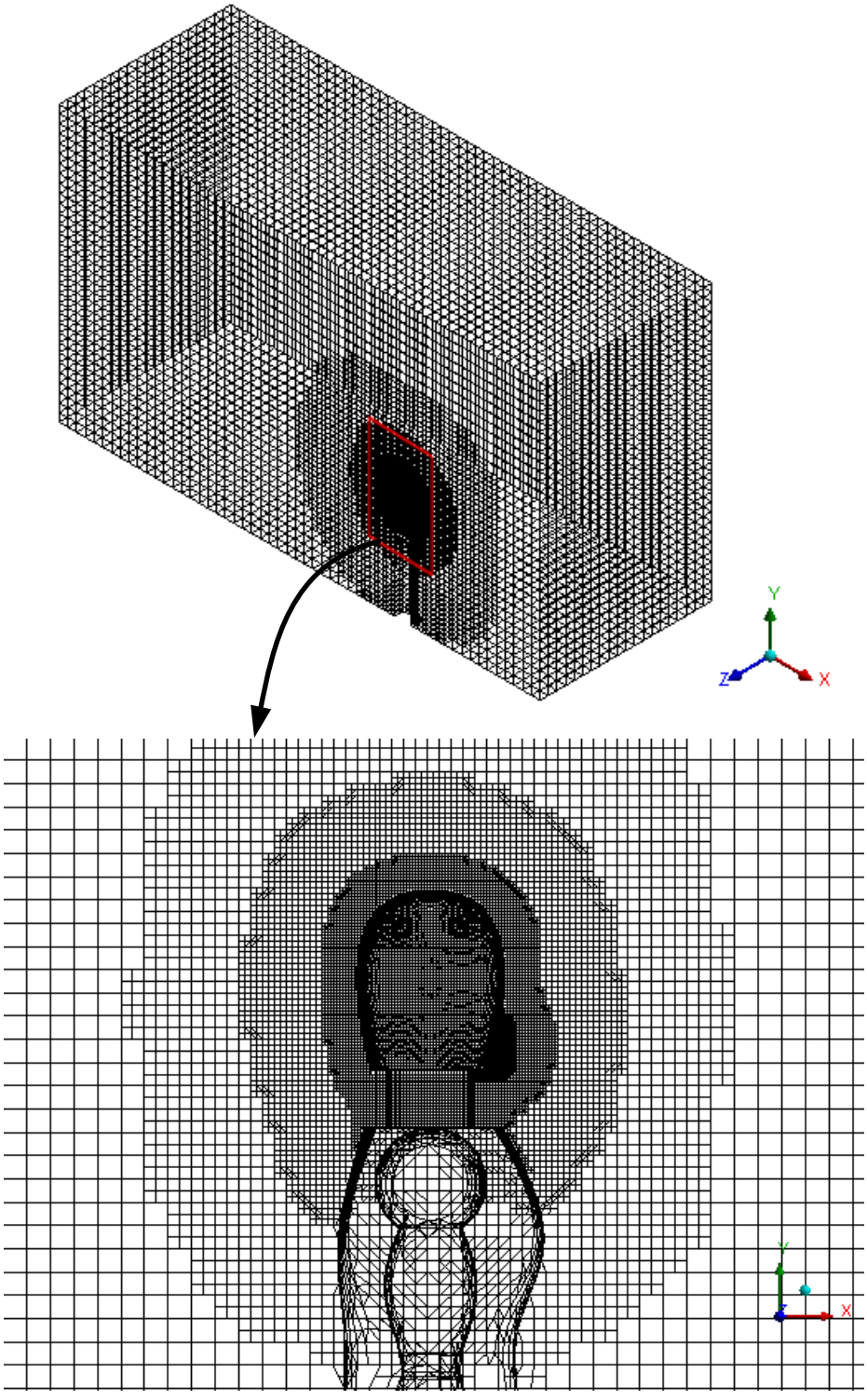

(Self-elaborated)

9.2 Initial and boundary conditions

The Eulerian-Lagrangian boundary condition can be specified based on the composition of the flow which are made up of the continuous phase and discrete phase as presented in Table 25.

Table 26- Boundary condition of the Euler-Lagrangian model

	Eulerian Phase	**Lagrangian Phase**	**Chamber boundary Region**
Particle Inlet	Velocity inlet	Surface velocity injection	B 01
Wind inlet	Velocity inlet	-	B 02
Outlet	Pressure outlet	Escape	B 07
Wall	No-slip, specified shear and pressure outlet	Reflect and trap	B 03, B 04, B 05 and B 06

(Self-elaborated)

This part of the research also applied the shared numerical properties in Section 5.3. In addition, the tests were conducted with climatic conditions of São Carlos City, São Paulo, Brazil. The city of São Carlos has an average temperature of 294.25 K, and, a relative humidity of about 77% on average. The establishment of the range of the wind velocity was inspired by the work of Barbosa (2009) where the author registered up to 3.4 m/s of wind velocity on the 26th day of February 2005. Therefore, the velocities of air flowing in one direction applied in this study are 0.5 m/s, 1.0 m/s, 3.0 m/s, and 4 m/s. Additionally, 400 respiratory droplets with 50 µm, 100 µm, 200 µm, 300 µm, and 500 µm are studied in a large and closed environment with the wind blowing against the droplets in one direction. These particles cover a range from medium to large sizes, which is interesting the the study of respiratory droplets. Since this simulation was expected to have a high computational, 400 droplets were used to conduct the studies.

9.3 Wall conditions

Tests were conducted regarding different wall conditions because boundary layers could have effect on the particle behavior (Wang and Levy, 2006), therefore, in this section, three conditions which are no-slip, zero-shear stress wall and pressure outlet were compared. These are all stationary wall conditions, and were respectively applied to the walls (B 03, B 04, B 05 and B 06) used to carry out the calculations at this stage of the research. In no-slip condition, the velocity of the fluid is zero at the fluid layer which is in contact with the wall. A zero-shear stress condition in ANSYS Fluent refers to a boundary condition where the wall exerts no tangential (shear) stress on the fluid. This can be used to simulate idealized cases where there is no frictional resistance at the wall, often to simplify problems or to study specific effects in fluid dynamics. Lastly, the pressure outlet, which is a boundary condition applied at the exit of the domain where the pressure is specified $P = P_{out}$. This condition allows for the calculation of the flow rate based on the given pressure and can accommodate backflow if the solution requires it. More details about the wall conditions are presented in Table 26.

Table 27. Wall conditions used in this research

Wall condition	Related expressions
No-slip	Roughness height = 0 and Roughness constant = 0.5 (uniform wall)
Zero-shear stress	Shear stress (Pa) where x, y, z = 0, 0, 0 roughness height and constant = 0
Pressure outlet	Guage pressure = 0 Pa Backflow turbulent intensity = 5% Backflow turbulent viscosity ratio = 10

(Self-elaborated)

It is important to highlight that in all the calculations, no-slip condition was applied on the floor of the domain (B 06) of Figure 37. From the droplet profiles presented in Figure 39, calculations under different wall conditions presented similar results. At very low velocity, vortex

shedding was more observed. The particles formed a more dispersed cloud behind the cougher as they were transported by the continuous phase. However, at a higher velocity, the particles formed a more compacted and organized particle cloud behind the cougher. The particles flew within the boundary layer close to the large eddy region (Figure 42 b). The 100 μm droplets reduced in diameter as they were transported by the wind. Due to their relatively large sizes, they were not completely evaporated. Such behavior was observed both at low and high wind velocities, respectively.

In Figure 40, the velocity profiles calculated using no-slip, zero shear-stress and pressure outlet were similar at the respective wind velocities in the XY-direction. Evaluation from different positional points in space, the velocity profiles for the respective boundary conditions were similar for instance on the YZ-plane as shown in Figure 41.

This result was expected because the space between the mannequin and the side walls was large. Therefore, the velocity of air acting on the droplets might be for all the boundary conditions. However, this could be different if the walls were closer, with no-slip boundary condition registering the lowest maximum due to the nature of the velocity boundary layer formed by the fluid.

Figure 39- Droplet path for different wind velocities flowing opposite to cough droplets under different boundary conditions at the walls

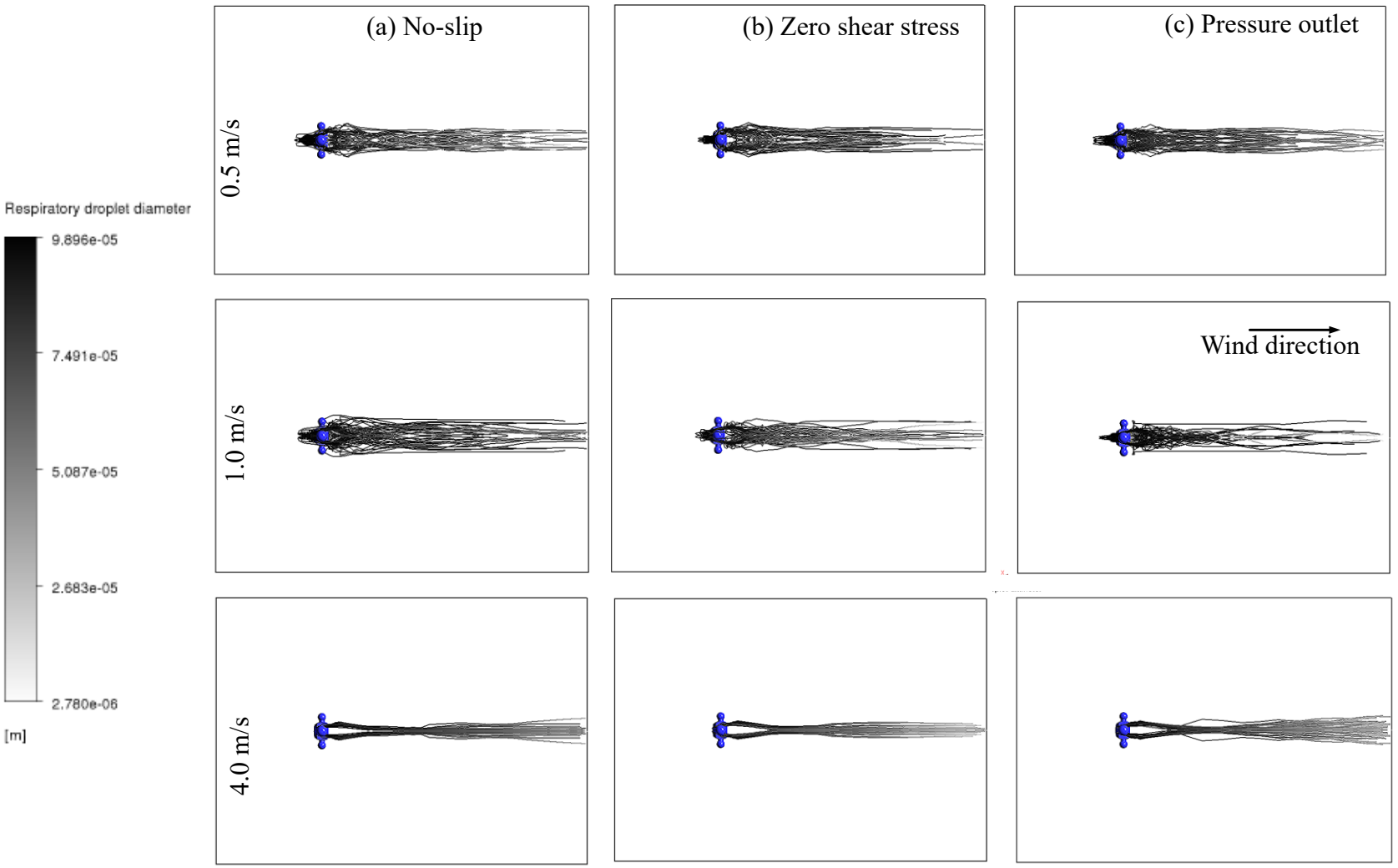

(Self-elaborated)

Figure 40- Contours of wind velocity with different magnitudes and its impact as it blows against 100 µm droplets emitted during coughing applying different boundary conditions

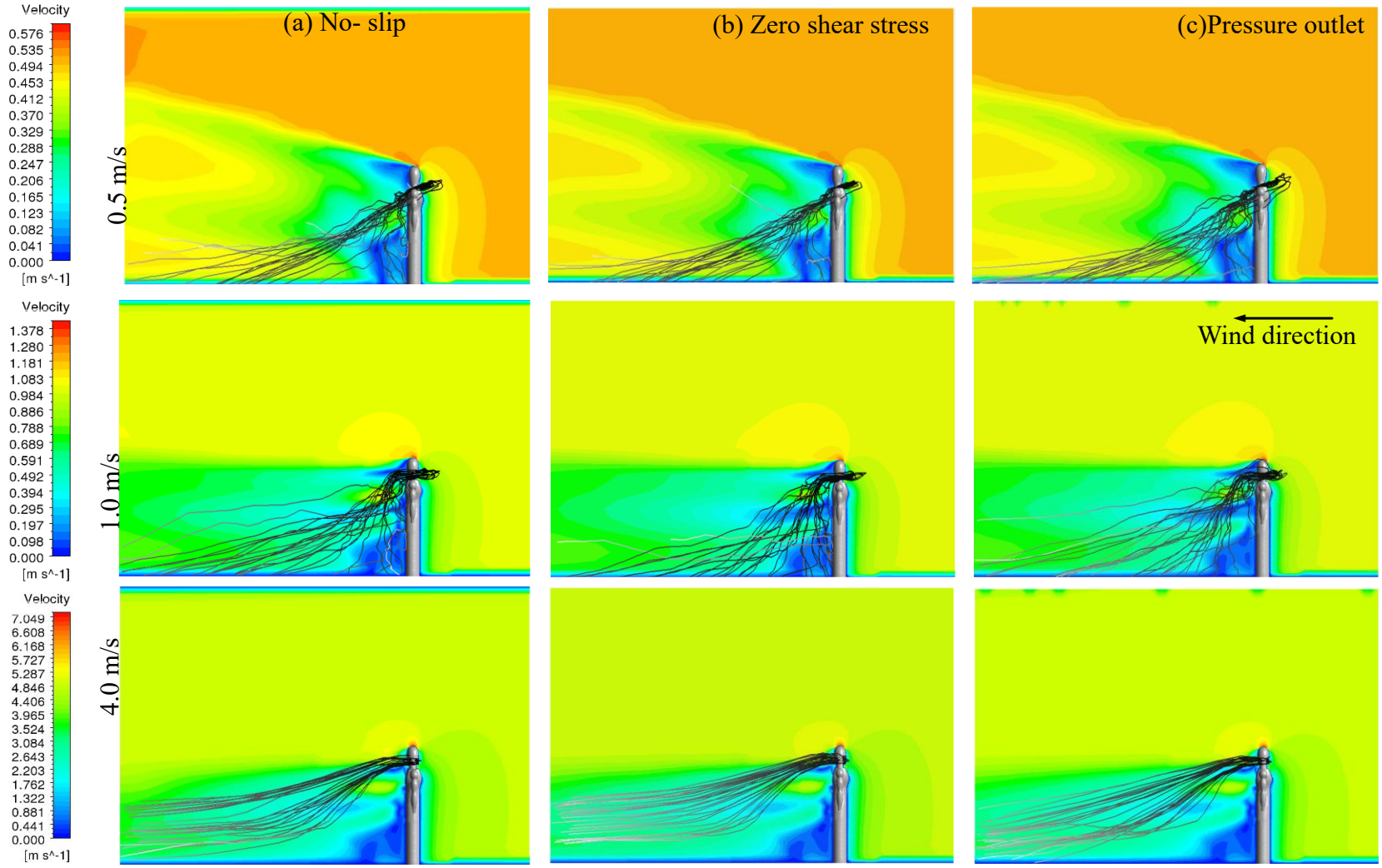

(Self-elaborated)

Figure 41-YZ plane velocity profile under a wind velocity of 3 m/s (a) no-slip (b) zero shear stress and (c) pressure outlet

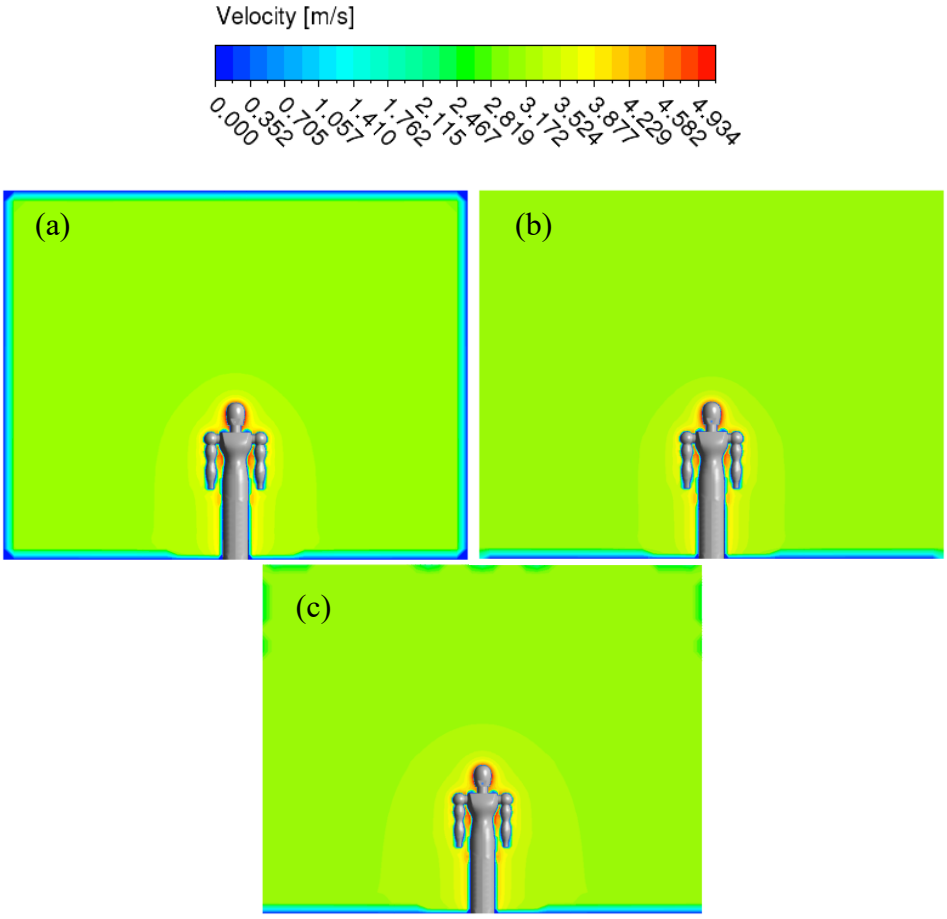

(Self-elaborated)

The gravitational, drag, and buoyant forces are predominant in the flow presented in previous sections of this work. At low velocities transporting fluid velocity, the drag forces acting on the respiratory droplets are relatively small, and the particles are primarily influenced by gravity and buoyancy, giving way to the formation of more dispersed particle cloud. On the other hand, at high velocities, the drag force becomes significant and often dominates.

When the droplets are released at a specific velocity, they encounter the wind flowing at its natural velocity. Immediately, the droplets begin to decelerate due to the action of the drag forces exerted by the blowing wind. At a specific time, the particles totally lose their kinetic energy and begin to acquire energy from the moving air. At this point, the droplets flow in the direction of

the wind by the total dominance of the drag force. At high velocities, high Reynolds region is formed behind the person releasing the respiratory droplets as shown in Figure 42. The Turbulent Reynolds contours are projected on a ZX-plane at a height of 1.5 m from the floor of the domain.

Figure 42- ZX-plane of Reynolds profile of wind at high velocity (4/m) (a) no-slip (b) zero-shear stress (c) pressure outlet

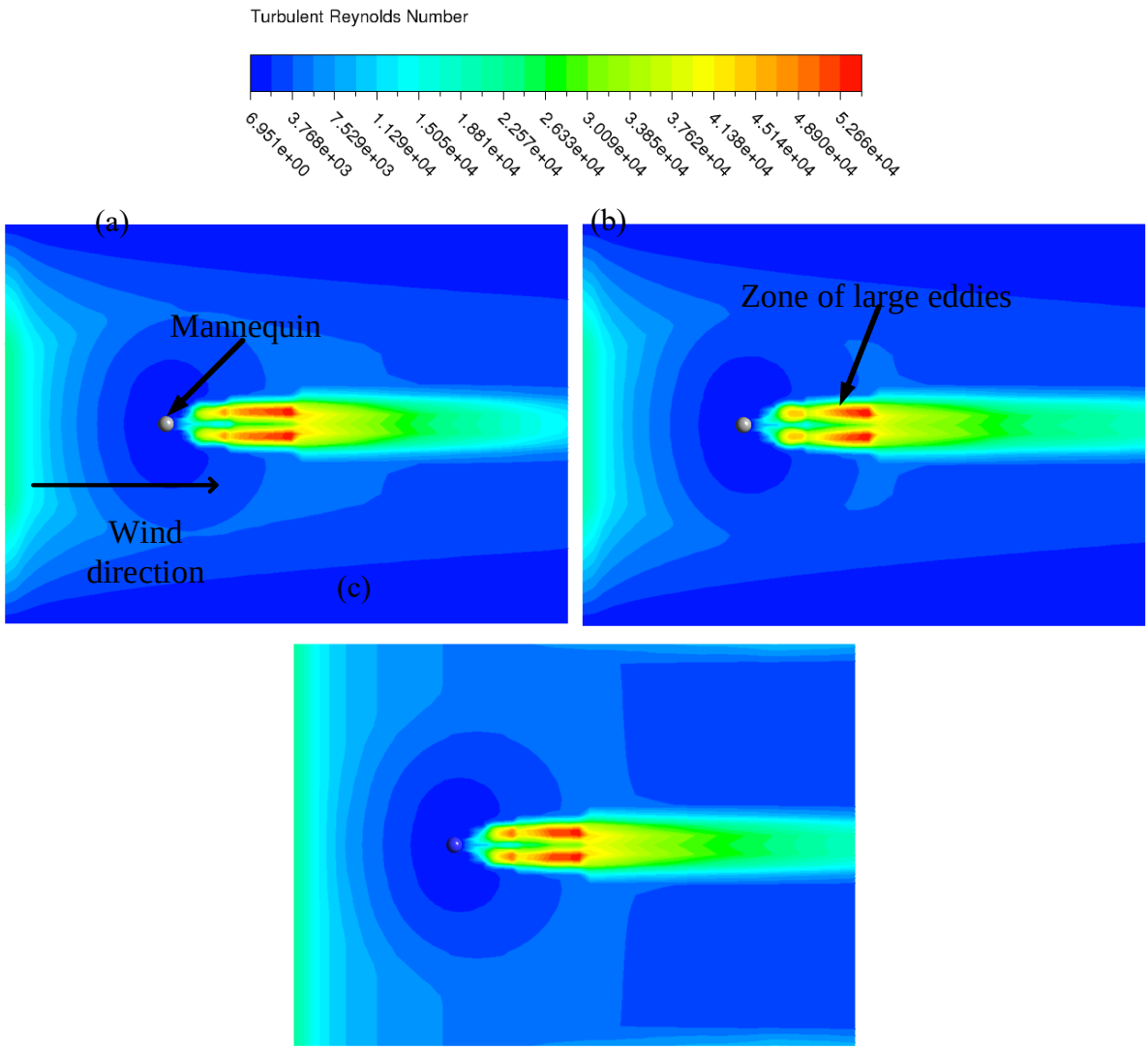

(Self-elaborated)

The Reynolds is calculated from $Re = \rho_g v_g L/\mu_g$. Where L is characteristic length of the Reynolds number, and its value is the height of the cougher (1.7 m).

The highest Reynolds number was calculated using zero-shear stress boundary conditions, while the lowest was obtained with a no-slip wall. The difference between these two values is significant, approximately 5000. In the no-slip boundary condition, the velocity decreases as it approaches the wall, which likely affected the Reynolds number. Additionally, there was a difference of about 2000 between the Reynolds numbers calculated using zero-shear stress and those obtained from the pressure outlet. To relate the three boundary conditions together, one can say that zero-shear stress and pressure outlet calculated the most similar Reynolds number. Their turbulent region extends to from the cougher to the end of the domain. On the contrary, the turbulent region with a non-slip wall diminishes as it approaches the wind outlet. In terms of Turbulent Reynolds profile in Figure 42, pressure outlet boundary condition (c) seems to mimic an outdoor space since its boundary layers develop with respect to obstacle (the cougher) in the flow stream. For the no-slip and the zero-shear stress to mimic an outdoor space, the boundaries need to be infinitesimally distant from the cougher.

The economical evaluation of the boundary conditions is presented in Table 27. It states the approximate time used to conduct a complete simulation using the respective boundary conditions. A simulation was considered complete when all the droplets dropped on the floor or evacuated the flow domain.

Table 28- Details of computational time at different air velocity applied in this work

Boundary condition	**Approximate computation time**		
	0.5 m/s	1 m/s	3 m/s and 4 m/s
No-slip	4-5 days	2-3 days	3-7 hours
Zero-shear stress	7-8 days	5-6 days	2-4 days
Pressure outlet	10-11 days	8-9 days	4-6 days

(Self-elaborated)

In terms of computational cost, the wall conditions presented large discrepancies. The no-slip boundary condition is the best in terms of economy. It is followed by the zero-shear stress boundary condition. And lastly, the most expensive boundary condition is the pressure outlet.

Since the results calculated by the aforementioned boundary conditions had little difference in terms of particle behavior concerning time and space, one could strategically apply the no-slip wall condition considering its lower computational costs. However, to mimic outdoor environments, the pressure outlet is recommended.

9.4 Behavior of droplets in moving air

9.5.1. Smaller and larger droplets

Smaller droplets had maximum diameters of 50 μm, while larger droplets had diameters of 200 μm, 300 μm, and 500 μm. The simulations were conducted using the properties detailed in Section 9.3. A non-slip boundary condition, selected for its low computational cost, was employed in these simulations.

The behavior of smaller respiratory droplets under varying wind velocities is illustrated in Figure 43. On the other hand, the that of the larger droplets is illustrated in Figures 44 and 45.

At a wind velocity of 0.5 m/s (Figure 43a), the droplets traveled a relatively short distance before completely evaporating. The reduction in droplet size due to evaporation had minimal effect on particle behavior, as they continued to fall because of the low air velocity before evaporation occurred. When the wind velocity increased to 1 m/s (Figure 43b), the droplets traveled further before evaporating. This scenario highlighted the influence of wind on the behavior of respiratory droplets: droplets within large eddy regions evaporated more rapidly, whereas those in the boundary layer, outside the region with the highest Reynolds number, traveled farther before evaporating. At a wind velocity of 4 m/s (Figure 43c), most respiratory droplets traveled across the entire domain and exited it.

Figure 43- The flow profile of smaller respiratory droplets of 50 μm in diameter using no-slip stress boundary condition and (a) 0.5 m/s (b) 1 m/s and (c) 3 m/s velocities

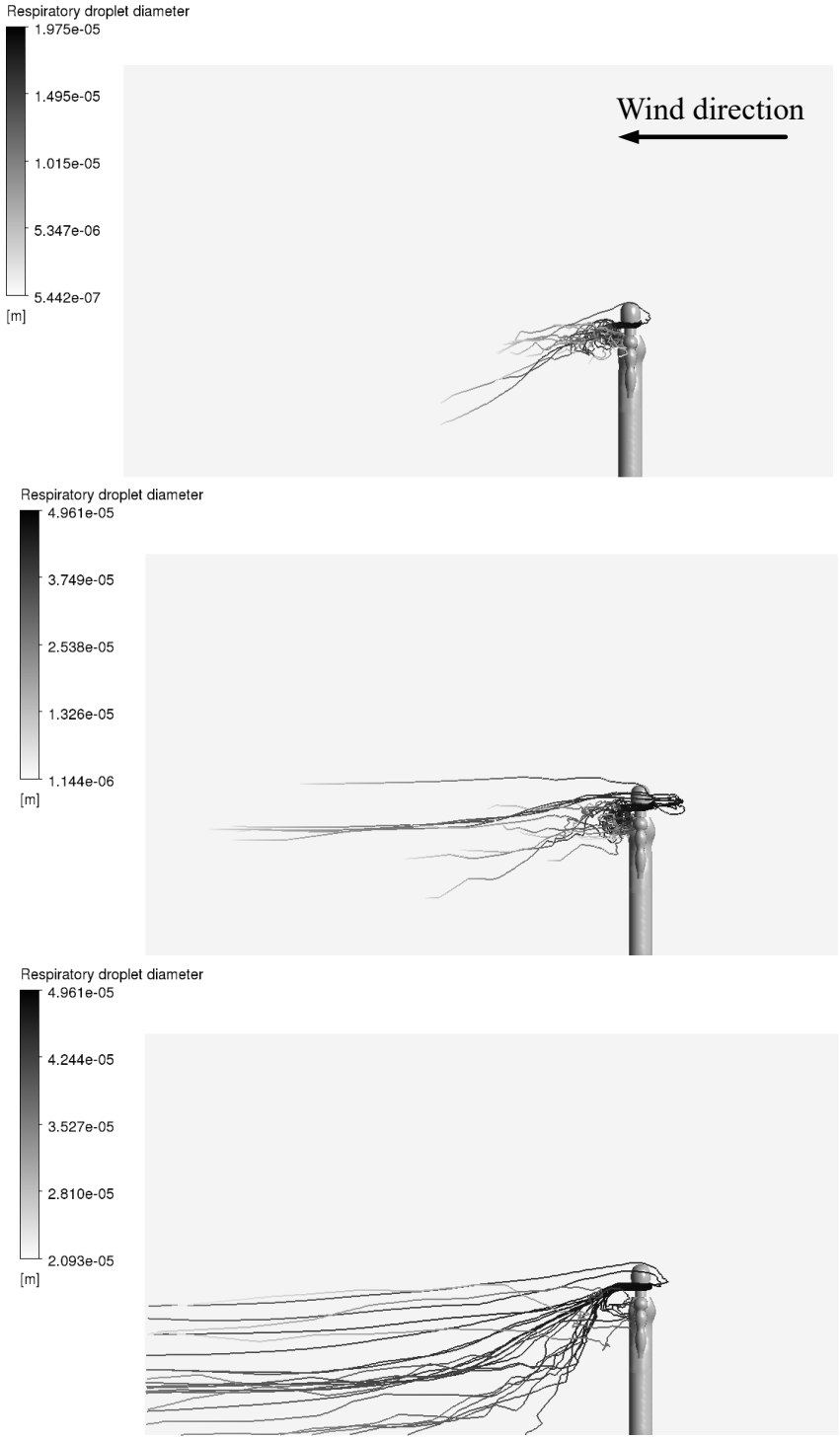

(Self-elaborated)

Figure 44- The flow profile of larger respiratory droplets using no-slip stress boundary condition and (a) 200 µm under 0.5 m/s (b) 300 µm under 4 m/s

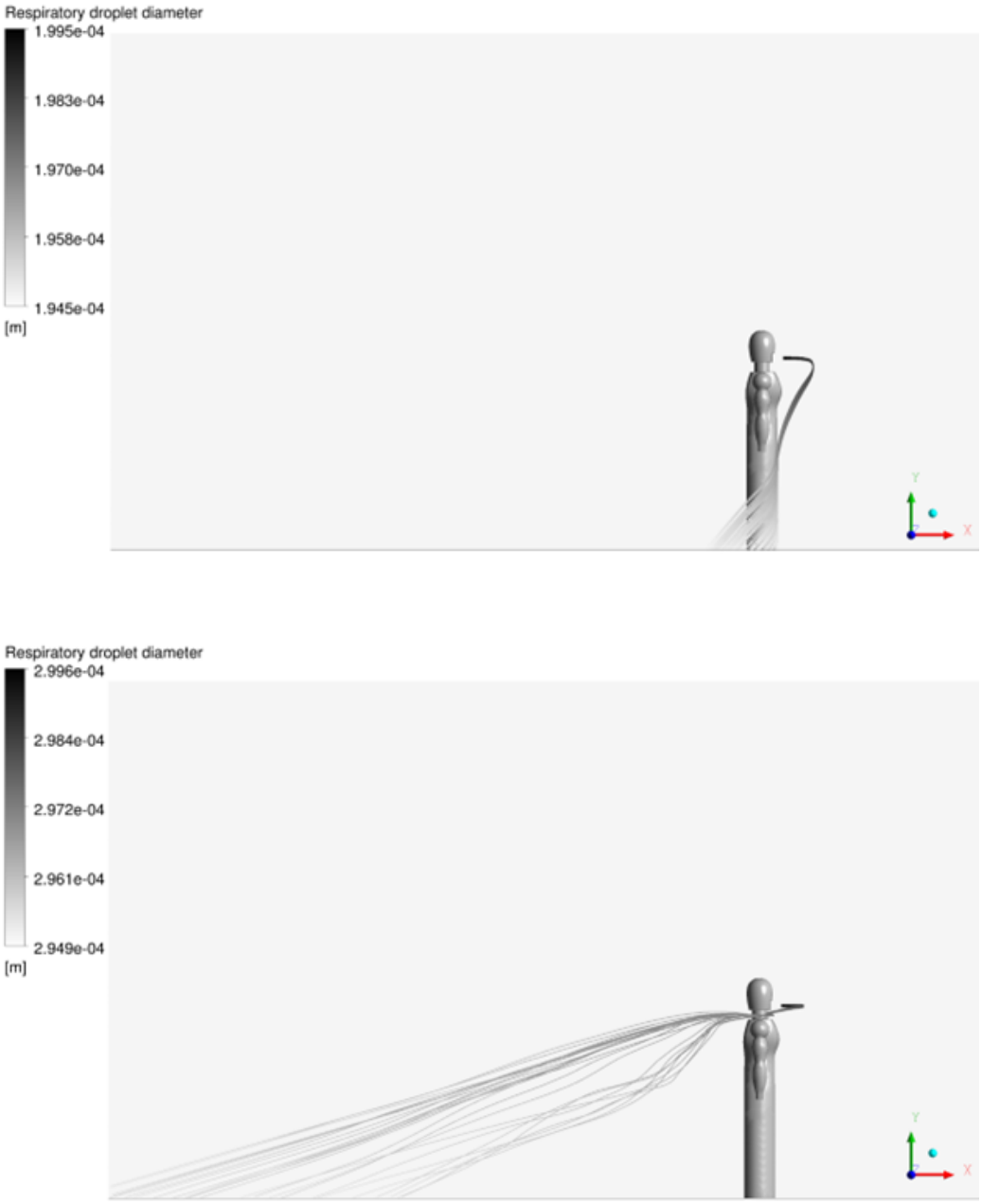

(Self-elaborated)

Figure 45- The flow profile of large respiratory droplets of 500 μm in diameter using no-slip stress boundary condition and (a) 0.5 m/s (b) 4 m/s

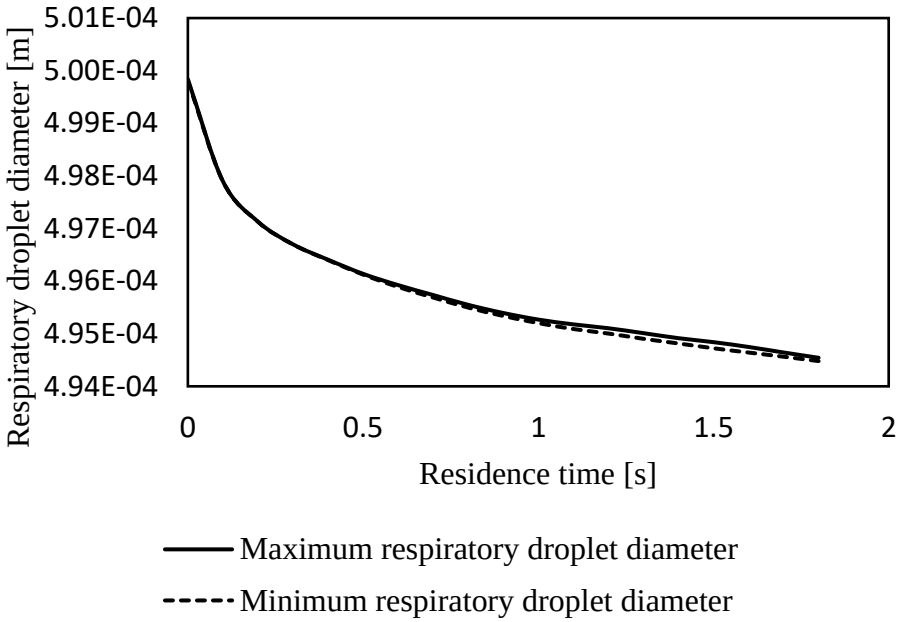

(b)

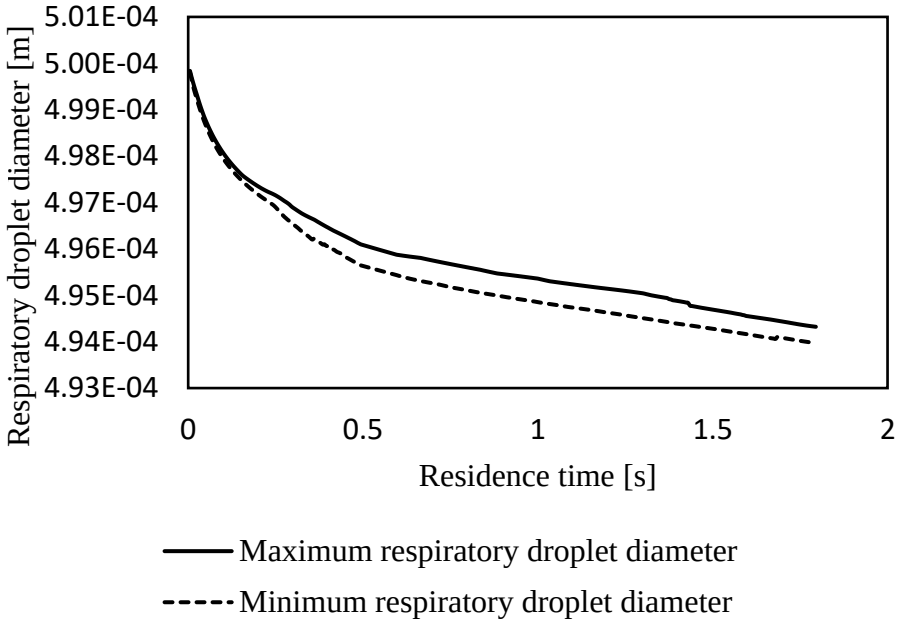

(Self-elaborated)

In Figure 43 c, the air inertia exerted sufficient force to reintegrate droplets from the low-pressure region behind the cougher. Some particles evaporated, particularly those within the large eddy region, while others fell to the floor or exited the flow domain, carried by the wind. In contrast to smaller droplets, larger droplets were displaced shorter distances at low wind velocities but traveled farther as wind velocity increased. Furthermore, larger droplets did not evaporate completely, as shown in Figures 44 and 45. It can also be observed that the rate of evaporation of larger droplets was similar at low and high wind speeds. However, at low wind speed, the evaporation was more uniform as presented by the maximum and minimum respiratory droplet diameters in Figure 45.

9.5.2. Significance of 50 μm respiratory droplets

Droplets with diameters close to 50 μm are particularly significant in studies of infectious respiratory droplet (IRD) transmission. This size range represents a balance: droplets are neither too heavy to quickly fall to the ground nor too light to evaporate immediately upon release. Very large droplets tend to settle rapidly, while smaller droplets evaporate quickly. However, 50 μm diameter droplets exhibit unique characteristics that allow them to persist in the air.

As discussed in Section 7, high relative humidity is a crucial factor in the persistence of respiratory droplets in the surrounding air. Additionally, as Figure 43c demonstrates, the persistence of droplets is also influenced by the velocity of the surrounding air. Therefore, it can be concluded that respiratory droplets remain airborne for longer durations at higher wind velocities compared to lower wind velocities.

10. CONCLUSIONS

In the initial phase of this research, we compared three turbulence models—SST k-ω, standard k-ε, and Reynolds Stress Model (RSM)—by simulating the evaporation of a single respiratory droplet. The results obtained from each model were consistent with one another. However, notable differences in computational cost were observed, with the RSM being the most computationally intensive, followed by the SST k-ω model. The similarities in results could be attributed to the simplified nature of the flow problem considered. Despite this, all three models demonstrated the capability to accurately compute the evolution of a single droplet in a quiescent environment. Therefore, the SST k-ω is recommended. The model offers a good balance between accuracy and computational cost, particularly effective near walls and in boundary layers, making it suitable for CFD studies of respiratory events.

In the second part of this research, mesh studies were carried out with the aim of comparing two prominently applied meshes to study the CFD of droplets emitted during human respiratory events. The graded hexahedral and tetrahedral meshes were employed to simulate the behavior of respiratory droplets in indoor and quiescent environments. The study's findings suggest that the evolution of droplets from activities like coughing is best calculated using a graded hexahedral mesh. The first observation emerged from the GCI test for both mesh types, showing that the mesh ratio's asymptotic convergence range reflected their capacity to calculate accurate results. The second observation revealed that, under certain conditions, the graded hexahedral mesh produced flow behavior more aligned with reality compared to the tetrahedral mesh. Typically, droplets with a diameter $d \geq 100\mu m$ fall to the ground due to gravity without fully evaporating if they originate from an average human height. The hexahedral mesh results aligned with literature, while the tetrahedral mesh results were less realistic, showing delayed fall and complete evaporation of droplets. Although the graded hexahedral mesh incurs a slightly higher computational cost than the graded tetrahedral mesh (10% to 13% more CPU time), this is incomparable with the quality of results it provides in simulating respiratory droplet flow in indoor environments. Therefore, in CFD studies of respiratory events using graded meshes, the respiratory droplet size should determine the cell geometry for computation. For larger droplets ($d \geq 100\mu m$), this study indicates that a graded hexahedral mesh is preferable. However, for smaller droplets (d

≤ 50μm), both graded tetrahedral and hexahedral meshes are effective. In case one applies the tetrahedral mesh, the mesh density needs to be increased.

Even thought the hexahedral meshes are recommended in this work, the tetrahedral mesh can also be applied given that a higher mesh density is applied, and a test is executed to observe key parameters like velocity and distance, which are functions of time.

The third part of this research was conducted to investigate the influence of air relative humidity on the evaporation of cough droplet. From the results obtained, it was concluded that even though relative humidity is an important factor in the spread of IRDs, for it to be efficient in disease spread, the respiratory droplets must have a certain range of diameter to withstand evaporation and gravitational pull at the same time. The best combination of the particle size and the humidity that could favor IRD transmission was observed when respiratory droplets with 50 μm in diameter were injected into a quiescent space with RH 80%. Thus, the farthest horizontal range (of 1.34 m) of respiratory droplets was registered in this work. Therefore, this work recommends a minimum social distance of 1.40 m from infected people to avoid contamination through respiratory droplets in an indoor and quiescent space.

Even though slight differences were observed in the results obtained from the application of the coupling models M1 and M2 in general, it can be concluded that model coupling is insignificant in calculating problems of CFD of respiratory droplets, regardless of droplet size and relative humidity. However, in cases where the flow involves a considerable quantity of droplets, coupling may be required for a more accurate calculation. Therefore, in an indoor environment, coupling is not recommended.

The fourth and last part of this research had the objective of applying the previous findings to study the behavior of respiratory droplets under the climatic conditions of São Carlos city, São Paulo, Brazil. Here, it was observed that different boundary conditions calculated similar droplet behavior in space, however, their respective computational cost varied significantly. From the results obtained in this work, the no-slip boundary condition is recommended to carry out simulations in indoor environments, however, it can also be used for outdoor simulations when the boundaries are infinitesimally distant from the region of flow of the respiratory droplets. The zero-

shear and the pressure outlet boundary conditions can be applied to compute the behavior of respiratory droplets in outdoor environments despite their high computational cost. Notwithstanding, the zero-shear stress boundary condition is recommended when the outdoor simulation is to be carried out with one-directional wind in a small computational domain.

Additionally, medium-sized droplets (with diameters around 50 μm) transported by high velocity winds with high relative humidity can travel greater distances (more than 1.34 m obtained in an indoor and quiescent environment), making this combination of factors and parameters efficient for airborne contamination.

In conclusion, the findings in this work could aid in establishing standards that can aid in controlling the spread of IRDs in closed and open environments. Additionally, it can aid in the selection and application of CFD models that are capable of describing the behavior of respiratory droplets emitted during respiratory events, considering accuracy and computational cost.

REFERENCES

Aliabadi, A. A., Rogak, S. N., Green, S. I., & Bartlett, K. H. (2010). CFD simulation of human coughs and sneezes: A study in droplet dispersion, heat, and mass transfer. In ASME International Mechanical Engineering Congress and Exposition (Vol. 44441, pp. 1051-1060).

Alfonsi, G. (2009). Reynolds-averaged Navier–Stokes equations for turbulence modeling. Applied Mechanics Reviews, 62(4), 040802. doi:10.1115/1.3124648.

Amsden, A. A. (1989). A computer program for chemically reactive flows with sprays. Los Alamos National Laboratory Report LA-11560-MS.

ANSYS Fluent. (2013). ANSYS Fluent User's Guide. Version 14.5. ANSYS, Inc.

Augusto, L. L. X., Lopes, G. C., & Gonçalves, J. A. S. (2016). A CFD study of deposition of pharmaceutical aerosols under different respiratory conditions. Brazilian Journal of Chemical Engineering, 33, 549-558.

Auler, A. C., Cássaro, F. A. M., Da Silva, V. O., & Pires, L. F. (2020). Evidence that high temperatures and intermediate relative humidity might favor the spread of COVID-19 in tropical climate: A case study for the most affected Brazilian cities. Science of the Total Environment, 729, 139090.

Azarnoosh, J., Sreenivas, K., & Arabshahi, A. (2016). CFD investigation of human tidal breathing through human airway geometry. Procedia Computer Science, 80, 965-976.

Bagheri, G., & Bonadonna, C. (2016). Aerodynamics of volcanic particles: characterization of size, shape, and settling velocity. In Volcanic ash (pp. 39-52). Elsevier.

Bahramian, A., Mohammadi, M., & Ahmadi, G. (2023). Effect of indoor temperature on the velocity fields and airborne transmission of sneeze droplets: An experimental study and transient CFD modeling. Science of The Total Environment, 858, 159444.

Baldan, G., Bellosta, T., & Guardone, A. (2023). Efficient Lagrangian particle tracking algorithms for distributed-memory architectures. Computers & Fluids, 256, 105856.

Barbosa, R. V. R. (2009). Estudo do campo térmico urbano de São Carlos (SP): Análise da intensidade da ilha de calor urbano em episódio climático de verão (Doctoral dissertation, Universidade de São Paulo).

Baudouin, T. C., Remacle, J. F., Marchandise, E., Henrotte, F., & Geuzaine, C. (2014). A frontal approach to hex-dominant mesh generation. Advanced Modeling and Simulation in Engineering Sciences, 1(1), 1-30.

Biswas, R., & Strawn, R. C. (1998). Tetrahedral and hexahedral mesh adaptation for CFD problems. Applied Numerical Mathematics, 26(1-2), 135-151.

Bourouiba, L. (2020). Turbulent gas clouds and respiratory pathogen emissions: potential implications for reducing transmission of COVID-19. Jama, 323(18), 1837-1838.

Branche, A. R., & Falsey, A. R. (2015). Respiratory syncytial virus infection in older adults: an under-recognized problem. Drugs & aging, 32, 261-269.

Campbell, J. (2015). Entrainment. Complete Casting Handbook (Second Edition), 17–90. Butterworth-Heinemann. doi:10.1016/b978-0-444-63509-9.00002-9.

Cao, Q., Liu, M., Li, X., Lin, C. H., Wei, D., Ji, S., ... & Chen, Q. (2022). Influencing factors in the simulation of airflow and particle transportation in aircraft cabins by CFD. Building and Environment, 207, 108413.

Chen, H., Zhou, X., Feng, Z., & Cao, S. J. (2022). Application of polyhedral meshing strategy in indoor environment simulation: Model accuracy and computing time. Indoor and Built Environment, 31(3), 719-731.

Chillón, S. A., Fernandez-Gamiz, U., Zulueta, E., Ugarte-Anero, A., & Urbina-Garcia, O. (2023). Numerical modeling of a sneeze, a cough and a continuum speech inside a hospital lift. Heliyon, 9(2).

Climate-Data. (2023). Clima São Carlos: Temperatura, Tempo e Dados climatológicos São Carlos. Retrieved from https://pt.climate-data.org/america-do-sul/brasil/sao-paulo/sao-carlos-4818/. Accessed on June 27, 2023.

Dao, H. T., & Kim, K. S. (2022). Behavior of cough droplets emitted from Covid-19 patient in hospital isolation room with different ventilation configurations. Building and Environment, 209, 108649.

D'Alessandro, V., Falone, M., Giammichele, L., & Ricci, R. (2021). Eulerian–Lagrangian modeling of cough droplets irradiated by ultraviolet–C light in relation to SARS-CoV-2 transmission. Physics of Fluids, 33(3).

Dbouk, T., & Drikakis, D. (2020). On coughing and airborne droplet transmission to humans. Physics of Fluids, 32(5).

Elghobashi, S. (1994). On predicting particle-laden turbulent flows. Applied scientific research, 52, 309-329.

Faizal, W. M., Ghazali, N. N. N., Khor, C. Y., Badruddin, I. A., Zainon, M. Z., Yazid, A. A., Ibrahim, N. B., & Razi, R. M. (2020). Computational fluid dynamics modelling of human upper airway: A review. *Computer Methods and Programs in Biomedicine*, *196*, 105627.

Faleiros, D. E., van den Bos, W., Botto, L., & Scarano, F. (2022). TU Delft COVID-app: A tool to democratize CFD simulations for SARS-CoV-2 infection risk analysis. Science of the Total Environment, 826, 154143.

Ferziger, J. H., Perić, M., & Street, R. L. (2019). Computational methods for fluid dynamics. Springer.

K, J. K., Lin, C. H., & Chen, Q. (2009). Flow dynamics and characterization of a cough. Indoor Air, 19(6), 517-525.

Gosman, A. D., & Loannides, E. (1983). Aspects of computer simulation of liquid-fueled combustors. Journal of energy, 7(6), 482-490.

Guo, Y., Wei, J., Ou, C., Liu, L., Sadrizadeh, S., Jin, T., … Li, Y. (2020). Deposition of droplets from the trachea or bronchus in the respiratory tract during exhalation: A steady-state numerical investigation. Aerosol Science and Technology, 54(8), 869–879.

Gupta, J. K., Lin, C. H., & Chen, Q. (2009). Flow dynamics and characterization of a cough. Indoor air, 19(6), 517-525.

Han, Z. Y., Weng, W. G., & Huang, Q. Y. (2013). Characterizations of particle size distribution of the droplets exhaled by sneeze. Journal of the Royal Society Interface, 10(88), 20130560.

He, R., Yi, P., & Li, T. (2020). Evaporation and condensation characteristics of N-heptane and multi-component diesel droplets under typical spray relevant conditions. International Journal of Heat and Mass Transfer, accepted.

Honkinen, M., Lahti, E., Österback, R., Ruuskanen, O., & Waris, M. (2012). Viruses and bacteria in sputum samples of children with community-acquired pneumonia. Clinical microbiology and infection, 18(3), 300-307.

Jiang, Y. (2020). General mesh method: A unified numerical scheme. Computer Methods in Applied Mechanics and Engineering, 369, 113049.

Kolanjiyil, A. V., Hosseini, S., Alfaifi, A., Farkas, D., Walenga, R., Babiskin, A., ... & Longest, P. W. (2022). Validating CFD predictions of nasal spray deposition: Inclusion of cloud motion effects for two spray pump designs. Aerosol Science and Technology, 56(4), 305-322.

Kwok, Y. L. A., Gralton, J., & McLaws, M. L. (2015). Face touching: a frequent habit that has implications for hand hygiene. American journal of infection control, 43(2), 112-114.

Kucharski, A. J., Klepac, P., Conlan, A. J., Kissler, S. M., Tang, M. L., Fry, H., ... & Simons, D. (2020). Effectiveness of isolation, testing, contact tracing, and physical distancing on reducing transmission of SARS-CoV-2 in different settings: a mathematical modelling study. The Lancet infectious diseases, 20(10), 1151-1160.

Li, H., Leong, F. Y., Xu, G., Ge, Z., Kang, C. W., & Lim, K. H. (2020). Dispersion of evaporating cough droplets in tropical outdoor environment. Physics of Fluids, 32(11).

Li, H., Leong, F. Y., Xu, G., Kang, C. W., Lim, K. H., Tan, B. H., & Loo, C. M. (2021). Airborne dispersion of droplets during coughing: A physical model of viral transmission. Scientific Reports, 11(1), 4617.

Li, X., Shang, Y., Yan, Y., Yang, L., & Tu, J. (2018). Modelling of evaporation of cough droplets in inhomogeneous humidity fields using the multi-component Eulerian-Lagrangian approach. Building and Environment, 128, 68-76.

Lintermann, A. (2021). Computational meshing for CFD simulations. Clinical and Biomedical Engineering in the Human Nose: A Computational Fluid Dynamics Approach, 85-115.

Menter, F. R., Kuntz, M., & Langtry, R. (2003). Ten years of experience with the SST turbulence model. In K. Hanjalic, Y. Nagano, & M. Tummers (Eds.), Turbulence, Heat and Mass Transfer (Vol. 4, pp. 625–632). Begell House Inc.

Morawska, L., & Cao, J. (2020). Airborne transmission of SARS-CoV-2: The world should face the reality. Environment International, 139, 105730. https://doi.org/10.1016/j.envint.2020.105730.

Morawska, L. (2005). Droplet fate in indoor environments, or can we prevent the spread of infection?. In Indoor Air 2005: Proceedings of the 10th International Conference on Indoor Air Quality and Climate (pp. 9-23). Tsinghua University Press.

Oh, W., Ooka, R., Kikumoto, H., & Han, M. (2022). Numerical modeling of cough airflow: Establishment of spatial–temporal experimental dataset and CFD simulation method. Building and Environment, 207, 108531.

Oh, W., Ooka, R., Kikumoto, H., & Lee, S. (2024). Effects of ventilation rate and social distancing on risk of transmission of disease: A numerical study using Eulerian-Lagrangian method. Aerosol Science and Technology, 58(1), 70-90.

Ong, S. W. X., Tan, Y. K., Chia, P. Y., Lee, T. H., Ng, O. T., Wong, M. S. Y., & Marimuthu, K. (2020). Air, surface environmental, and personal protective equipment contamination by severe acute respiratory syndrome coronavirus 2 (SARS-CoV-2) from a symptomatic patient. JAMA, 323(16), 1610-1612.

Ozcelik, M. T., & Kokturk, B. (2019). Modeling of flow and dispersion in indoor air environments using CFD approach. Computational Thermal Sciences: An International Journal, 11(6), 531-548.

O'ROURKE, P. J. (1981). Collective drop effects on vaporizing liquid sprays (Doctoral dissertation, Princeton University).

O'Rourke, P. J., & Amsden, A. A. (1987). The TAB method for numerical calculation of spray droplet breakup (No. 872089). SAE technical paper.

Pan, K. L., Chou, P. C., & Tseng, Y. J. (2009). Binary droplet collision at high Weber number. Physical Review E—Statistical, Nonlinear, and Soft Matter Physics, 80(3), 036301.

Patel, R. P., Airoldi, C., Sforza, G., & Comerford, D. (2022). Comparison of computational and experimental approaches for predicting spray deposition of nasal sprays: A review. Respiratory Drug Delivery Europe, 2022, 303–314.

Perot, B., & Wang, H. (1999). Modeling separation and reattachment using the turbulent potential model. In Engineering Turbulence Modelling and Experiments 4 (pp. 145-154). Elsevier Science Ltd.

Qi, S., Li, Z., Yue, Y., van Triest, H. J., & Kang, Y. (2014). Computational fluid dynamics simulation of airflow in the trachea and main bronchi for the subjects with left pulmonary artery sling. Biomedical engineering online, 13(1), 1-15.

Redrow, J., Mao, S., Celik, I., Posada, J. A., & Feng, Z. G. (2011). Modeling the evaporation and dispersion of airborne sputum droplets expelled from a human cough. *Building and Environment*, *46*(10), 2042-2051.

Roache, P. J. (1998). Verification and validation in computational science and engineering (Vol. 895, p. 895). Albuquerque, NM: Hermosa.

Roache, P. J. (1994). Perspective: a method for uniform reporting of grid refinement studies.

Rosa, P., Jacob, C., & Pedrini, A. (2022). Evaluation of alternative solar cooling methods for buildings in hot climates. Energy Reports, 8, 357-366. https://doi.org/10.1016/j.egyr.2021.12.022.

Santana, Harrson S., et al. "Computational methodology for the development of microdevices and microreactors with ANSYS CFX." MethodsX 7 (2020): 100765.

Scapellato, R., Canfora, P., & Gatto, P. (2020). Assessment of exposure to SARS-CoV-2 via aerosol during exercise in confined spaces: The case of indoor swimming pools. Environmental Pollution, 267, 115476.

Scharfman, B. E., Techet, A. H., Bush, J. W. M., & Bourouiba, L. (2016). Visualization of sneeze ejecta: steps of fluid fragmentation leading to respiratory droplets. Experiments in Fluids, 57(2), 1-9.

Sedighi, A. A., Haghighat, F., Nasiri, F., Cao, S., & Ren, C. (2023). Approaches in CFD Modeling of Respiratory Droplet Dispersion–Issues and Challenges. *Sustainable Cities and Society*, 104696.

Shan, M., Zhang, D., Zhang, J., Lei, Q., & Li, C. (2022). Numerical study on the effects of ventilation and source control measures in a hospital ward with suspected airborne transmission of COVID-19. Building and Environment, 210, 108640.

Shinohara, M., Yoshida, T., & Ikeda, T. (2021). Evaluation of social distance and ventilation effect on indoor particle transport using CFD simulations. Aerosol and Air Quality Research, 21(6).

Solano, J. P. G., & Pereira, C. R. (2015). Fluid flow analysis and CFD code validation for simulation of urban microclimates. Journal of Wind Engineering and Industrial Aerodynamics, 147, 32-44.

Tan, Z. L., Wu, C. H., & Cheng, C. H. (2022). CFD simulation of aerosol deposition in the human upper airway: A comparison of polyhedral, tetrahedral, and hybrid mesh types. In Proceedings of the 14th International Symposium on Fluid Control, Measurement, and Visualization (FLUCOME2022), 160–167.

Tang, J. W., Nicolle, A. D., Klettner, C. A., Pantelic, J., Wang, L., Suhaimi, A. B., ... & Morris, J. G. (2013). Airflow dynamics of human jets: Sneezing and breathing–potential sources of infectious aerosols. PloS One, 8(4), e59970.

Tsega, E. G. (2022). CFD simulations of respiratory airflow in human upper airways response to walking and running for oral breathing condition. Heliyon, 8(8).

Tsega, E. G. (2018). Computational fluid dynamics modeling of respiratory airflow in tracheobronchial airways of infant, child, and adult. Computational and mathematical methods in medicine, 2018.

Walsh, B., & Boyle, F. J. (2020). A preconditioned lattice Boltzmann Flux solver for steady flows on unstructured hexahedral grids. Computers & Fluids, 210, 104634.

Wang, J., & Levy, E. K. (2006). Particle behavior in the turbulent boundary layer of a dilute gas-particle flow past a flat plate. Experimental thermal and fluid science, 30(5), 473-483.

Wang, J., & Chow, T. T. (2011). Numerical investigation of influence of human walking on dispersion and deposition of expiratory droplets in airborne infection isolation room. Building and Environment, 46(10), 1993-2002.

Wang, W., Cao, Y., & Okaze, T. (2021). Comparison of hexahedral, tetrahedral and polyhedral cells for reproducing the wind field around an isolated building by LES. Building and Environment, 195, 107717.

Wei, J., & Li, Y. (2015). Enhanced spread of expiratory droplets by turbulence in a cough jet. Building and Environment, 93, 86-96.

Worth Longest, P., & Xi, J. (2008). Condensational Growth May Contribute to the Enhanced Deposition of Cigarette Smoke Particles in the Upper Respiratory Tract. Aerosol Science and Technology, 42(8), 579–602.

Yan, Y., Li, X., & Tu, J. (2019). Thermal effect of human body on cough droplets evaporation and dispersion in an enclosed space. *Building and Environment*, *148*, 96-106.

Yang, R., Zhang, X., Wang, Q., Zhang, M., & Song, W. (2020). Transmission of pathogen-laden expiratory droplets in a coach bus. Journal of Hazardous Materials, 397, 122572.

Yang, Y., & Sekaran, S. D. (2021). Numerical simulation of indoor airflow distribution in classrooms with different ventilation strategies. Indoor and Built Environment, 30(5), 638-653. https://doi.org/10.1177/1420326X20972954.

Zahari, N. M., et al. "Introduction of discrete phase model (DPM) in fluid flow: a review.". (2018). AIP Conference Proceedings. Vol. 2030. No. 1. AIP Publishing LLC.

Zambrano-Mendoza, E. D., & Colle, S. (2020). Comprehensive study on the energy performance of photovoltaic ventilated façades under different climates. Energy, 193, 116800. https://doi.org/10.1016/j.energy.2019.116800.

Zee, M., Davis, A. C., Clark, A. D., Wu, T., Jones, S. P., Waite, L. L., Cummins, J. J. & Olson, N. A. (2021). Computational fluid dynamics modeling of cough transport in an aircraft cabin. *Scientific reports*, *11*(1), 23329.

Zhao, B., Zhang, Z., Li, X., & Yang, L. (2005). Numerical study of the transport of droplets or particles generated by respiratory system indoors. Building and Environment, 40(8), 1032-1039.

Zhou, B., Wang, H., Li, Z., & Huang, D. (2022). Investigation of cough airflow and droplet dispersion using CFD and Lagrangian approaches. Indoor and Built Environment, 31(4), 963-974.

APPENDIX I

The .h script file containing the UDF that describes the velocity at which the humid air is injected into the flow domain.

```
/************************************************************************

unsteady.c

UDF for specifying a transient velocity profile boundary condition

************************************************************************/

#include "udf.h"

DEFINE_PROFILE(axial_velocity, thread, position)

{

face_t f;

real t = CURRENT_TIME;

begin_f_loop(f, thread)

{

F_PROFILE(f, thread, position) = 38226*t*t*t*t*t*t - 56113*t*t*t*t*t + 27922*t*t*t*t - 4231.3*t*t*t - 599.44*t*t + 180.79*t - 0.6382;

}

end_f_loop(f, thread)}
```